Year : 2023

In vivo characterization of brain tissue microstructure

Veiga De Oliveira Ana Rita

UNIL | Université de Lausanne
Faculté de biologie et de médecine

Département des neurosciences cliniques

In vivo characterization of brain tissue microstructure
Thèse de doctorat en Neurosciences

présentée à la

Faculté de biologie et de médecine
de l'Université de Lausanne

par

Ana Rita VEIGA DE OLIVEIRA

Master de Instituto Superior Técnico, Portugal

Jury

Prof. Paul Franken, Président
Dr. Antoine Lutti, Directeur de thèse
Dr. Marzia De Lucia, Co-directeurtrice de thèse
Prof. Derek Jones, Expert
Prof. Dimitri Van De Ville, Expert

Thèse n° 385

Lausanne
(2023)

Programme doctoral interuniversitaire en Neurosciences des Universités de Lausanne et Genève

LEMANIC NEURO SCIENCE DOCTORAL SCHOOL

UNIL | Université de Lausanne

UNIVERSITÉ DE GENÈVE

UNIL | Université de Lausanne

UNIVERSITÉ DE GENÈVE

Programme doctoral interuniversitaire en Neurosciences des Universités de Lausanne et Genève

Imprimatur

Vu le rapport présenté par le jury d'examen, composé de

Président·e	Monsieur	Prof.	Paul Franken
Directeur·trice de thèse	Monsieur	Prof.	Antoine Lutti
Co-directeur·trice de thèse	Madame	Prof.	Marzia De Lucia
Expert·e·s	Monsieur	Prof.	Derek Jones
	Monsieur	Prof.	Dimitri Van de Ville

le Conseil de Faculté autorise l'impression de la thèse de

Madame Ana Rita Veiga de Oliveira

Mestrado Integrado Em Engenharia Biomédica

intitulée

***In vivo* characterization of brain tissue microstructure**

Lausanne, le 27 octobre 2023

pour Le Doyen
de la Faculté de Biologie et de Médecine

Prof. Paul Franken

Acknowledgments

Finishing my PhD was only possible due to the invaluable support of a group of individuals to whom I owe my deepest gratitude.

First, I would like to thank my two supervisors Antoine Lutti and Marzia De Lucia for the opportunity to join their lab and to work with them. Their passion for learning and discovering is fascinating. I am very grateful for their support throughout this PhD and for all that they taught me during this time.

I also want to express my appreciation to all the collaborators and colleagues who have contributed to my PhD projects. In particular to Andria, Quentin and Giulia for their important contributions to this work, including data acquisition and scientific discussions. I extend my profound gratitude to Andria for her invaluable support throughout my PhD journey and for being an irreplaceable friend.

My special thanks to all my colleagues who I had the opportunity to meet in this laboratory. This journey was exceptionally enjoyable thanks to all of them. Giada, Louise, Clara, Sivaniya, Olga, Maya, Ayberk, Jenny, I am grateful for all the moments spent with you, including all the chitchat, scientific discussions and hiking adventures.

My special thanks to the Oron neighbours whom I was glad to meet when I moved to Switzerland for my PhD. These last years would not have been the same without them. I also want to thank Filipa, Joana, Rafaela and Teresa who despite being far are still always there.

Finally, there is no way to compare my family support to anything else. My heartfelt gratitude in particular to my mum, dad, my sister Carolina, tia Ana and tio Zé who have been there all the way.

Abstract

Brain tissue microstructure plays an important role in brain function. Estimates of brain microstructure obtained *in vivo* can serve as valuable biomarkers to quantify brain tissue changes in living humans. However, non-invasive neuroimaging techniques, such as Magnetic Resonance Imaging (MRI), are unable to directly provide information on the microstructure of brain tissue. Estimating microscopic features of brain tissue *in vivo* requires the use of biophysical models that relate the measured signal to the underlying microstructure. In line with this, our focus was on obtaining measures of the morphology of axons composing white matter and of deposits of iron within brain tissue from data acquired using *in vivo* neuroimaging techniques.

First, in terms of axonal morphology, we developed a novel biophysical model for the simultaneous estimation of axonal radius and relative myelin thickness using MRI and Electroencephalography (EEG) data. The proposed approach for axonal morphology estimation involved the challenging task of estimating axonal conduction velocities from EEG data *in vivo*. We addressed this challenge by implementing a new technique in which conduction velocities were obtained by the calculation of the interhemispheric transfer time estimated as the latency difference between the maximal neuronal activity at two homologous visual cortical regions. The obtained conduction velocities were consistent with existing literature and were then used in the proposed axonal morphology model. The estimated axonal morphological features were consistent with values from histological studies of brain tissue. These results highlight the potential of this non-invasive technique in providing an accurate axonal morphology characterization of white matter tracts.

Second, we investigated the distribution of deposits of magnetic material in subcortical grey matter. We applied existing biophysical models that account for the impact of magnetic materials on the MRI signal due to transverse relaxation. These models allow for the estimation of the volume fraction occupied by the magnetic deposits as well as their magnetic susceptibility. The estimated volume fraction and magnetic susceptibility within the magnetic deposits were in line with the distribution of iron in *ex vivo* studies, consistent with the primary source of magnetic material in these regions being iron. The proposed approach enabled the characterization of iron deposits within brain tissue with increased specificity, offering a novel approach for the study of iron-related brain changes in neurodegenerative diseases.

Overall, in this work we characterized i) the morphology of axons in white matter tracts and ii) the iron deposits within subcortical grey matter. The estimated microstructural features, obtained in healthy participants non-invasively, were consistent with *ex vivo* literature, thereby holding the potential to become useful biomarkers. Such biomarkers may be highly relevant for assessing microstructural changes in individuals with neurological disorders.

Keywords: MRI, EEG, microstructure, *in vivo* histology, axonal morphology, iron

Résumé

La microstructure du tissu cérébral joue un rôle important dans le fonctionnement du cerveau. Les estimations de la microstructure du cerveau obtenues *in vivo* peuvent servir de biomarqueurs précieux pour quantifier les changements du tissu cérébral chez les êtres humains vivants. Toutefois, les techniques de neuro-imagerie non invasives, telles que l'imagerie par résonance magnétique (IRM), ne sont pas en mesure de fournir directement des informations sur la microstructure du tissu cérébral. L'estimation des caractéristiques microscopiques du tissu cérébral *in vivo* nécessite l'utilisation de modèles biophysiques qui relient le signal mesuré et la microstructure sous-jacente. Dans cette optique, notre objectif était d'obtenir des mesures de la morphologie des axones composant la matière blanche et des dépôts de fer dans le tissu cérébral à partir de données acquises à l'aide de techniques de neuro-imagerie *in vivo*.

Tout d'abord, en ce qui concerne la morphologie axonale, nous avons mis au point un nouveau modèle biophysique pour estimer de manière simultanée le rayon axonal et l'épaisseur relative de la myéline à l'aide de données d'IRM et d'électroencéphalographie (EEG). L'approche proposée pour l'estimation de la morphologie axonale impliquait la tâche difficile d'estimer les vitesses de conduction axonale à partir des données EEG *in vivo*. Nous avons relevé ce défi en mettant en œuvre une nouvelle technique dans laquelle les vitesses de conduction ont été obtenues par le calcul du temps de transfert interhémisphérique estimé comme la différence de latence entre l'activité neuronale maximale dans deux régions corticales visuelles homologues. Les vitesses de conduction obtenues étaient cohérentes avec la littérature existante et ont ensuite été utilisées dans le modèle de morphologie axonale proposé. Les caractéristiques morphologiques estimées des axones étaient cohérentes avec les valeurs des études histologiques des tissus cérébraux. Ces résultats soulignent le potentiel de cette technique non invasive pour fournir une caractérisation précise de la morphologie axonale.

Deuxièmement, nous avons étudié la distribution des dépôts de matériaux magnétiques dans la matière grise sous-corticale. Nous avons appliqué des modèles biophysiques existants qui tiennent compte de l'impact des matériaux magnétiques sur le signal IRM causé par la relaxation transversale. Ces modèles permettent d'estimer la fraction de volume occupée par les dépôts magnétiques ainsi que leur susceptibilité magnétique. La fraction volumique et la susceptibilité magnétique estimées à l'intérieur des dépôts magnétiques étaient conformes à la distribution du fer dans les études *ex vivo*, cohérent avec le fait que la principale source de matériaux magnétiques dans ces régions est le fer. L'approche proposée a permis de caractériser les dépôts de fer dans le tissu cérébral avec une spécificité accrue, offrant une nouvelle approche pour l'étude des changements cérébraux liés au fer dans les maladies neurodégénératives.

Dans l'ensemble, nous avons caractérisé i) la morphologie des axones dans les faisceaux de matière blanche et ii) les dépôts de fer dans la matière grise sous-corticale. Les propriétés microstructurales estimées, obtenues chez des participants sains de manière non invasive, étaient cohérentes avec la littérature *ex vivo*, et pourraient donc devenir des biomarqueurs utiles. Ces biomarqueurs peuvent être très utiles pour évaluer les changements microstructuraux chez les personnes souffrant de troubles neurologiques.

Mots Clés: IRM, EEG, microstructure, histologie *in vivo*, morphologie axonale, fer

Contents

List of Tables

List of Figures

Acronyms

AIC	Akaike Information Criterion
AVF	Axon Volume Fraction
CSF	Cerebrospinal Fluid
DDE	Double Diffusion Encoding
DNR	Diffusion Narrowing Regime
EEG	Electroencephalography
fMRI	functional Magnetic Resonance Imaging
FVF	Fiber Volume Fraction
gMRI	Aggregated MRI g-ratio
GP	Globus Pallidus
IHTT	Interhemispheric Transfer Time
MRI	Magnetic Resonance Imaging
MSE	Mean Square Error
MT	Magnetization Transfer
MVF	Myelin Volume Fraction
MWF	Myelin Water Fraction
QSM	Quantitative Susceptibility Mapping
ROI	Region of Interest
SDE	Single Diffusion Encoding
SDR	Static Dephasing Regime
SMT	Spherical Mean Technique
SN	Substantia Nigra

Chapter 1

Introduction

1.1 Overview

Magnetic resonance imaging (MRI) is a widely used non-invasive imaging technique for investigating the human brain. In particular, MRI has been extensively used to analyze and segment macroscopic structural brain features such as cortical thickness (e.g. Fischl and Dale, 2000) and brain lesions (e.g. Miller et al., 2014). However, MRI falls short of directly resolving microscopic features of brain tissue, like cell sizes. Estimating such features using non-invasive techniques constitutes an ongoing challenge in neuroscience and is the core of 'microstructural imaging' or '*in vivo* histology' (Edwards et al., 2018; Weiskopf et al., 2015; Alexander et al., 2019).

The bedrock of microstructural imaging lies in biophysical models that map the relationship between the measured MR signal and the underlying microstructural properties of brain tissue one aims at estimating (Weiskopf et al., 2015; Edwards et al., 2018). These models vary in complexity, ranging from a simple correlation between a given MRI parameter and a microscopic feature (e.g. R_2^* and myelin content (Stüber et al., 2014; Lee et al., 2012)) to more complex ones (e.g. MRI g-ratio (Stikov et al., 2015)). Biophysical models can be viewed as "sketches" of reality (Novikov et al., 2018), as they involve a simplification of the neuronal tissue under consideration. Thus, distinct models are employed to study different brain tissue features and often require different types of neuroimaging data (Jelescu et al., 2020). For example, relaxometry MRI data are usually used to infer myelin composition (Does, 2018; MacKay and Laule, 2016) and diffusion MRI data is commonly used for the estimation of neuronal axon radii (Novikov et al., 2018).

Assessing microstructural information from MRI data enables the establishment of brain biomarkers. Brain biomarkers are measures of brain tissue that can be used to non-invasively assess and quantify structural or functional changes in the brain. In research, microstructural biomarkers may be used to study brain development and ageing (e.g. Zhao et al., 2016). Importantly, biomarkers have numerous clinical applications that contribute to the diagnostic process, including the monitoring of disease progression and the assessment of disease severity (e.g. Mohammadi and Callaghan, 2021; Jelescu et al., 2016).

The main objective of this PhD thesis is the characterization of brain tissue microstructure from data acquired using *in vivo* neuroimaging techniques. The characterization of microstructure was performed in two distinct projects. The first project focused on the estimation of morphological features of axonal populations (Fig. 1.1A). The second project targeted the characterisation of deposits of magnetic material within brain tissue, specifically iron (Fig. 1.1B). In this work, we introduced the methodology for estimating the aforementioned microstructural features of brain tissue and evaluated their validity in cohorts of healthy individuals. Ultimately, the estimated features could serve as biomarkers of microstructure with potential clinical utility.

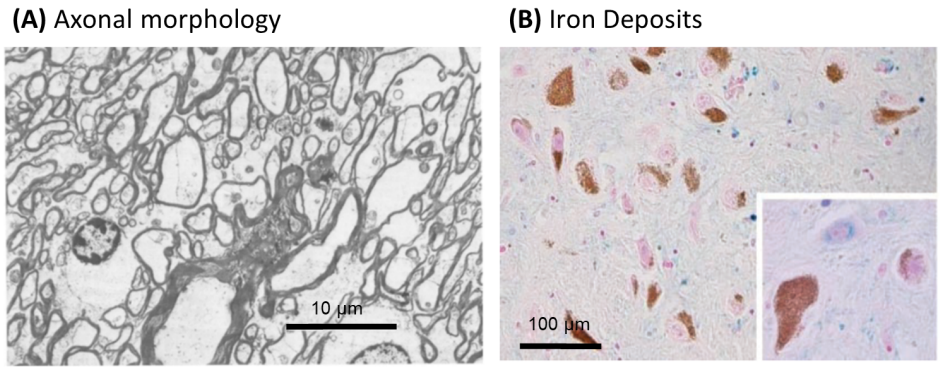

Fig. 1.1. Microstructural brain tissue features of interest in this thesis. (A) The first project focused on the estimation of morphological features of axonal populations. The electron micrograph shows multiple axons wrapped in myelin in the corpus callosum (adapted with permission from (Aboitiz et al., 1992)). (B) The second project focused on the characterization of magnetic deposits - aggregates of magnetic material such as iron - within brain tissue. The figure obtained by iron histochemistry with modified Perls' staining shows iron deposits (blue stain) mainly localized in oligodendrocytes (adapted with permission from (Zecca et al., 2004)).

1.2 Thesis outline

In this Chapter 1, the current techniques available for the estimation of axonal radius (section 1.3), fibre myelination (section 1.4), axonal conduction velocity (section 1.5), and iron content (section 1.6) will be detailed. With the motivation and background for this work established, the objectives behind the two projects implemented as part of this thesis are described (section 1.7).

Since the results regarding the characterization of magnetic material in brain tissue are not yet published, Chapter 2 is dedicated specifically to outlining the methodology and outcome of this project.

Chapter 3 offers a summary of the results obtained as part of this PhD project, which led to two scientific publications from the first project (section 3.1) and one draft manuscript from the second project (section 3.2). The two published articles derived from this research can be found in the Appendix.

Chapter 4 thoroughly discusses the results from the first (section 4.1) and second (section 4.2) projects.

1.3 Axonal Radius

1.3.1 Background

Axonal radius is a key structural property of neurons facilitating neuronal communication and determining axonal conduction velocity (Rushton, 1951; Waxman and Bennett, 1972). Larger-radius axons, mainly localized in primary sensory brain areas, facilitate faster information transfer, while smaller-radius axons prioritize information quantity over speed and are typically found in higher-level processing areas, such as the pre-frontal cortex (Lamantia and Rakic, 1990).

In healthy individuals, axon radii indices can provide valuable insights into the microstructural changes of neurons that occur during development and ageing (Stahon et al., 2016; Fan et al., 2019). Furthermore, axon radius may be used in generative models of brain function, providing measures of connectivity, for example using dynamic causal models (Honey et al., 2010; Stephan et al., 2009).

Assessing axon radius *in vivo* also has important clinical implications, as structural changes in axon size are associated with a variety of disorders. For example, compared to large axons, axons of small radius are primarily affected in autism (Wegiel et al., 2018) and multiple sclerosis (Evangelou et al., 2001). In contrast, in motor-neuron disease larger axons have been shown to be primarily impaired (Cluskey and Ramsden, 2001).

1.3.2 Techniques for axonal radius mapping

Over the past decades, numerous biophysical models have been proposed aimed at estimating axon radius in the brain. Diffusion MRI is a particularly well-suited technique for such estimation, due to its sensitivity to the microscopic motion of water molecules within tissue. Given that the motion of water molecules is hindered by compartmental boundaries like axons, modelling the water displacement allows for the inference of the underlying tissue architecture (Jelescu et al., 2020; Hagmann et al., 2006). Most biophysical models describe the measured signal by a weighted sum of the water signal coming from different tissue compartments and tissue microstructure information is estimated by fitting the model to the measured diffusion signal (Panagiotaki et al., 2012; Hagmann et al., 2006).

The first diffusion-based model for axon radius estimation worth mentioning is the one proposed by Stanisz et al. (1997). The authors described the measured signal using three different tissue compartments including water exchange between them: 1) spheres, representing glial cells; 2) ellipsoids, representing axons; and 3) the extracellular matrix. While this model enabled the estimation of volume fraction, size, membrane permeability, and diffusivity parameters, it required knowledge of the fibre orientation and it was not easily generalizable as it was designed and tested specifically for the bovine optic nerve.

Pioneering work by Assaf and colleagues introduced the CHARMED model (Assaf and Basser, 2005). This two-compartment framework modelled the intra- and extracellular compartments, assuming no exchange between the two compartments, no glial cell contribution, and axons of cylindrical geometry with a fixed radius. Even though CHARMED does not allow for the

estimation of axon radius *per se*, it was the basis for an extension put forward by the same group, coined AxCaliber (Assaf et al., 2008). With AxCaliber, the axon radius distribution – modelled by a gamma distribution – can be explicitly estimated. This model was validated by comparing MRI-based and *ex vivo* axonal radius estimates from excised nerve samples, yielding a high correspondence between the two types of measurements (Assaf et al., 2008). Barazany et al. (2009) further refined this method by adding an isotropic diffusion compartment accounting for cerebrospinal fluid (CSF) contribution. With this model extension, the authors were able to retrieve the known microstructural variation of radii along the corpus callosum of *in vivo* rats.

Despite the aforementioned advantages, AxCaliber and this latter extension (Barazany et al., 2009) have some limitations worth mentioning. First, both need MRI data to be acquired at high gradient strengths: 1 T/m for AxCaliber and 300 mT/m for Barazany et al. (2009). Second, they require long acquisition times: around 24 hours for AxCaliber and 2 hours for Barazany et al. (2009). Hence, these methods, though informative, cannot be easily applied to clinics, wherein current scanners provide gradient strengths between 40 and 80 mT/m, and long acquisition times are hard for individuals to tolerate. Third, these methods require *a priori* knowledge on fibre orientation; therefore, axon radius estimation is limited to a few brain structures for which this information is known.

To address the limitation of *a priori* knowledge on fibre orientation, AxCaliber 3D was proposed by Barazany et al. (2011) and applied on a fixed excised porcine spinal cord phantom. To estimate the full axon radius distribution in any fibre orientation, AxCaliber 3D projects the data perpendicular to the water-restricted compartment, thereby also being able to estimate axon radius in regions of crossing fibres.

The ActiveAx model was introduced by Alexander and colleagues (Alexander et al., 2010) and similarly aimed at providing orientational invariant axon radius estimates. This method succeeded in retrieving the known axon radii trend along the human corpus callosum *in vivo*. This four-compartment tissue model simplifies the two-compartment CHARMED model and combines it with a CSF compartment (similar to Barazany et al. (2009)) and a compartment accounting for the water trapped within small structures such as glial cells (similar to Stanisz et al. (1997)). Rather than the full distribution, ActiveAx provides a single summary index of the axon radius distribution, referred to as effective radius. Similar to the aforementioned methods, ActiveAx also assumes that all axons within single voxels have the same single orientation, therefore refinements to this method were later developed to improve the estimations in regions of orientation dispersions (Zhang et al., 2011b) and crossing fibres (Zhang et al., 2011a). Despite the improvements offered, ActiveAx and related models again require long acquisition times ($\sim$1 hour), making it still difficult to be employed in a clinical setting.

ActiveAxADD, an extension of ActiveAx proposed by Romasco and colleagues provides orientational invariant estimates, the novelty being a non-parametric approach and the estimation of the entire axon radius distribution (Romascano et al., 2019). While ActiveAxADD provided robust estimates on simulated data, the authors acknowledged that future work is needed to prove its reliability with *in vivo* data (Romascano et al., 2019).

While diffusion-based axon radius mapping acquisition protocols are commonly based on a single pair of pulsed-field gradients, i.e. single diffusion encoding (SDE), the acquisition method proposed by Benjamini et al. (2014, 2016) uses a double pair of pulsed-field gradients, i.e. double diffusion encoding (DDE). DDE has gained popularity for the quantification of microscopic diffusion metrics independent of orientation dispersion, due to the signal modulation that occurs between the application of the first and second diffusion encoding direction. Similarly to Romascano et al. (2019), the framework proposed in Benjamini et al. (2016) is also non-parametric, estimating axon radius distribution without *a priori* assumptions about the underlying form of the distribution. The major disadvantages of this method are again the need for extremely long acquisition times – $\sim$40 hours – and high gradient strengths. Moreover, MRI data acquisition is restricted to white matter tracts whose long axes are aligned to the main magnetic field.

More recently, to obtain axon radius estimates independent of fibre orientation distribution an alternative model was proposed by Fan et al. (2020). This method uses the spherical mean technique (SMT), which serves to integrate the diffusion MRI data along multiple gradient directions, thereby eliminating orientational dispersions. While Fan and colleagues were able to recover the usually observed trend in axon radius along the corpus callosum and estimate axon radii in crossing fibre configurations *in vivo* in humans, their method had similar limitations to the methods discussed above i.e. requiring high gradient strengths (300 mT/m) and long acquisition times ($\sim$1 hour).

In contrast to the voxel-level axon radius estimation employed by the previously mentioned methods, Barakovic and colleagues proposed a method to estimate axon radius for each group of axons with a similar trajectory, i.e. for each streamline. Their approach, entitled COMMITAxSize (Barakovic et al., 2021), is based on microstructure-informed tractography, and was applicable to crossing fibres, unlike most of the earlier models. This method was tested both with numerical simulations and *in vivo* human data and showed a good agreement between histology and known anatomy.

The AxSI (Diffusion-Based Axonal Spectrum Imaging) model put forward by Gast et al. (2023) also aims at estimating axon radii along individual streamlines. This model represents a simplified version of the previously developed AxCaliber and estimates axon radii by utilizing a library of simulated diffusion MRI signals. In this work, the known neuroanatomical features of axonal bundles were demonstrated in humans *in vivo*.

Finally, a diffusion-relaxation protocol model for radius estimation was proposed by Barakovic and colleagues (Barakovic et al., 2023). Relaxometry MRI is a viable technique for characterizing tissue microstructure, as relaxation rates like T2 also depend on the underlying tissue structural organization. By performing a histologically-informed calibration, the method implemented in Barakovic et al. (2023) may be sensitive to axon radii below the typical diffusion resolution limit of $\sim$1 μm (section 1.3.3). Despite the need for further validation, initial findings using this method in *in vivo* human data have demonstrated promising results (Dell'Acqua et al., 2023).

Table 1.1 summarizes axonal radius estimation methods which can vary in terms of: (i) the number of compartments; ii) handling of crossing fibres and orientation dispersion; iii) the need

for *a priori* hypotheses on the orientation of the underlying fibres; iv) whether they provide the entire axon radius distribution or a single summary index; v) and the technical requirements for use in a clinical setting.

Table 1.1. Axon radius estimation methods. N/D = Not Defined

Scientific publication	Model Name	Number of compartments	Whole distribution	Orientation invariant	Suitable for orientation dispersion	Suitable for crossing fibres	<= 80 mT/T	<= 1 hour
(Assaf et al., 2008)	AxCaliber	2	Yes	No	No	No	No	No
(Barazany et al., 2009)	AxCaliber (Extension)	3	Yes	No	No	No	No	No
(Barazany et al., 2011)	AxCaliber 3D	2	Yes	Yes	Yes	Yes	No	N/D
(Alexander et al., 2010)	ActiveAx	4	No	Yes	No	No	Yes	No
(Zhang et al., 2011b)	ActiveAx (Extension)	2	No	Yes	Yes	No	Yes	Yes
(Zhang et al., 2011a)	ActiveAx (Extension)	3	No	Yes	Yes	Yes	No	N/D
(Romascano et al., 2019)	ActiveAxADD	2	Yes	Yes	No	No	No	Yes
(Benjamini et al., 2014)	N/D	2	Yes	No	No	No	No	No
(Fan et al., 2020)	N/D	3	No	Yes	Yes	Yes	No	Yes
(Barakovic et al., 2021)	COMMITAxSize	3	Yes	Yes	No	Yes	No	N/D
(Gast et al., 2023)	AxSI	3	Yes	Yes	Yes	No	Yes	N/D

1.3.3 The challenge of radius overestimation

Despite advances made by the aforementioned models, the estimation of axon radius from *in vivo* data remains challenging. In addition to the limitations described in the previous section, in these models, the axon calibre is commonly overestimated when compared to histological data (Jones et al., 2018; Jelescu et al., 2020; Veraart et al., 2020). Indeed, typical axon radius distributions peak around 0.3 – 0.5 μm, with maximum axon radius between 1.5 – 3.0 μm (Aboitiz et al., 1992; Liewald et al., 2014). In contrast, MRI-derived axon radii are overestimated, calculated to be within the range of 1.3 – 7.5 μm (Alexander et al., 2010; Huang et al., 2015; Veraart et al., 2020). This section will attempt to uncover the major factors that contribute to this overestimation.

Gradient strengths

MRI gradient strengths impose a limitation on axonal radius estimation. Nilsson and colleagues proposed a metric coined "axon radius limit" or "resolution limit", corresponding to the smallest radius (r_{min}) that can be differentiated from a stick of zero radius given an MRI sequence under ideal conditions (Nilsson et al., 2017):

$$2r_{min} = \left(\frac{768}{7} \cdot \frac{\sigma D_0}{\gamma^2 G^2 \delta}\right)^{1/4} \tag{1.1}$$

D_0 is the free diffusivity of the intra-axonal water, G is the gradient amplitude, δ is the pulse duration, γ the gyromagnetic ratio and σ is the minimal detectable percentage change in the MRI signal. The rationale behind Eq. 1.1 is that if the signal attenuation coming from the axons is less than σ, it will be indistinguishable from a cylinder with a radius of zero. As per Eq. 1.1, the resolution limit critically depends on the gradient amplitude.

According to Nilsson, for a σ =1% (defined for a given significance value and signal-to-noise ratio level), the resolution limit radius ranges between 2.0 and 4.0 μm for a typical clinical scanner (with gradient strengths between 60 mT/m and 80 mT/m) and between 1.0 and 2.5 μm for a high gradient strength of 300 mT/m (Nilsson et al., 2017). A recent study by Veraart

et al. (2020) showed that with a clinical scanner of 80 mT/m, the smallest radius that can be differentiated from a stick of radius zero is $\sim$3.2 μm, whereas, with a scanner of gradient strength 300 mT/m, this value improves to $\sim$1.5 μm (Fig. 1.2A).

Moreover, it is worth noting that the presence of large-radii axons has a disproportionate influence on the MR signal contrast (Fig. 1.2B). In the example provided by Jones et al. (2018), even though only less than 10% of the axons had radii over 1.5 μm, those axons accounted for 50% of the intra-axonal signal. In addition, as gradient amplitudes increase (i.e. decrease in resolution limit), the percentage of axons above the resolution limit increased from 5% to 20%, whereas the signal these axons provided increased considerably more, from 35% to 70%.

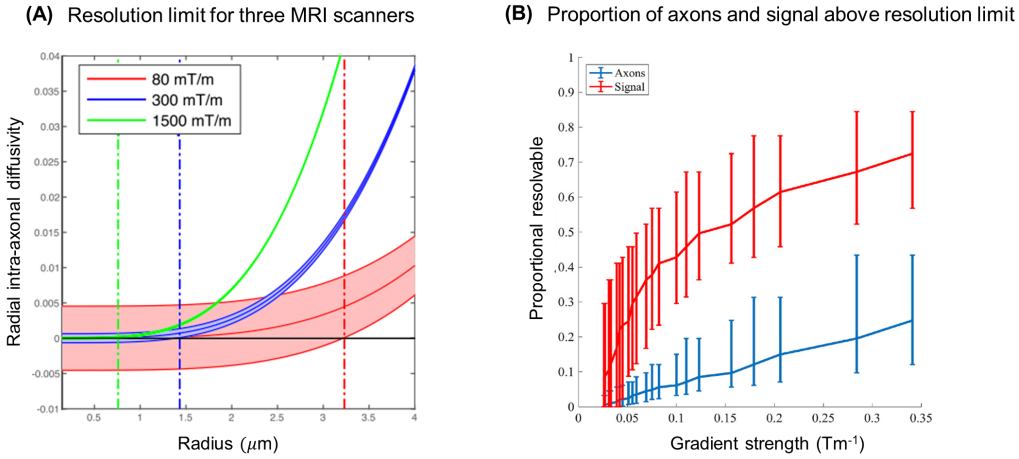

Fig. 1.2. Gradient strength impact on axon radius estimation. (A) Minimal cylinder radius that can be detected with a scanner of 80 mT/m (clinical human scanner), 300 mT/m (research human scanner), and 1500 mT/m (animal scanner), represented in red, blue, and green respectively. As the gradient increases, the smallest radius that can be differentiated from a stick of zero radius decreases. The minimum radius that can be measured with a clinical scanner is $\sim$3.2 μm. The shaded areas represent the 95% confidence interval (adapted with permission from (Veraart et al., 2020)). (B) The proportion of axons (blue) above the resolution limit and the proportion of intra-axonal signal (red) originating from these axons, as a function of gradient strength (adapted with permission from (Jones et al., 2018)). Both these results demonstrate the strong sensitivity of diffusion MRI to larger axons.

Extracellular contribution

Another factor contributing to the overestimation of axon radius is the extra-axonal signal influence on the diffusion signal (Fig. 1.3A). Indeed, recent work demonstrated that the diffusion signal has higher sensitivity to extra- rather than to intra- axonal water under specific diffusion regimes (Burcaw et al., 2015; Lee et al., 2018).

Single summary index

Using a single metric such as the effective radius to represent the entire diameter distribution may also contribute to the overestimation of the radius estimates. This is due to the fact that the effective radius is, by construction, a measure that is weighted towards large axons: $r_{eff} = \left(\frac{\langle r^6 \rangle}{\langle r^2 \rangle}\right)^{1/4}$ (Burcaw et al., 2015; Veraart et al., 2020). This implies that a small contribution of

large axons can have a large impact on the estimated effective radius (Fig. 1.3B).

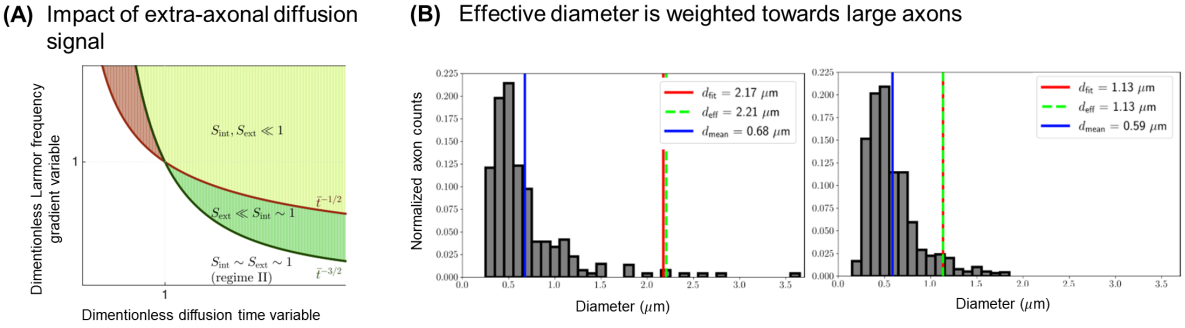

Fig. 1.3. Impact of the extracellular signal contribution and single summary index on axonal radius estimation. (A) Phase diagram of the diffusion signal. Green–shaded areas indicate that the signal is most sensitive to the intra–axonal water (S_{int}) and therefore can have a large impact on axonal radius estimation. Areas above the red line have a weak contribution from both intra–and extra –axonal (S_{ext}) signals. The white area, where clinical scanner gradient strengths can be found, corresponds to a weak gradient regime, where both intra–and extra–axonal water influence the acquired signal, making axonal radius estimation strongly biased (adapted with permission from (Burcaw et al., 2015)) (B) Changing the tail of a distribution of axon diameters, by adding a few extra axons in the 2−4 μm range heavily influences the effective diameter (d_{eff}), as opposed to the mean diameter (d_{mean}) which suffers only a small shift in value. The fitted MRI radius (d_{fit}) correlates well with the effective diameter (d_{eff}), which is weighted towards large-calibre axons (adapted with permission from (Paquette et al., 2020)).

Oversimplification of the tissue model

Another challenge in axon radius mapping lies in the simplifications made upon modelling the tissue architecture. It is commonly assumed that axons are perfect straight cylinders, however, this is not the case in the brain. First, radius variations along the axon length (undulation) exist (Andersson et al., 2020; Lee et al., 2019). Second, and differently, to what is assumed by many state-of-the-art methods, there is no single orientation to describe all axons within a voxel (orientation dispersion); in particular, crossing, bending, and fanning fibres are some configurations one can find in the brain (Andersson et al., 2020; Lee et al., 2019; Zhang et al., 2011b). The work of Andersson et al. (2020) demonstrates how any variation from a cylinder (e.g. undulation, orientation dispersion, Fig. 1.4A) leads to an overestimation of the axon radius compared to a perfectly aligned cylinder (Fig. 1.4B).

Finally, most diffusion-based axonal radius models simplify the tissue architecture with two or three compartments, ignoring glial or other neuronal cell contributions. However, as highlighted by Veraart and colleagues strong diffusion-weighted MRI can be sensitive to signals originating from glial cells (Veraart et al., 2023). Along similar lines, accounting for extra and intra-cellular compartments while neglecting water exchange between them, may also potentially lead to axon radii overestimation (Fieremans et al., 2010).

To conclude, the series of studies outlined above demonstrate that the overestimation of axon radius in existing models is an important challenge to overcome and may be explained by: (i) the currently available neuroimaging hardware (Fig. 1.2); (ii) the large contribution of the extracellular signal (Fig. 1.3A); (iii) the use of a single summary index (Fig. 1.3B); (iv) the oversimplification of the tissue architecture (Fig. 1.4).

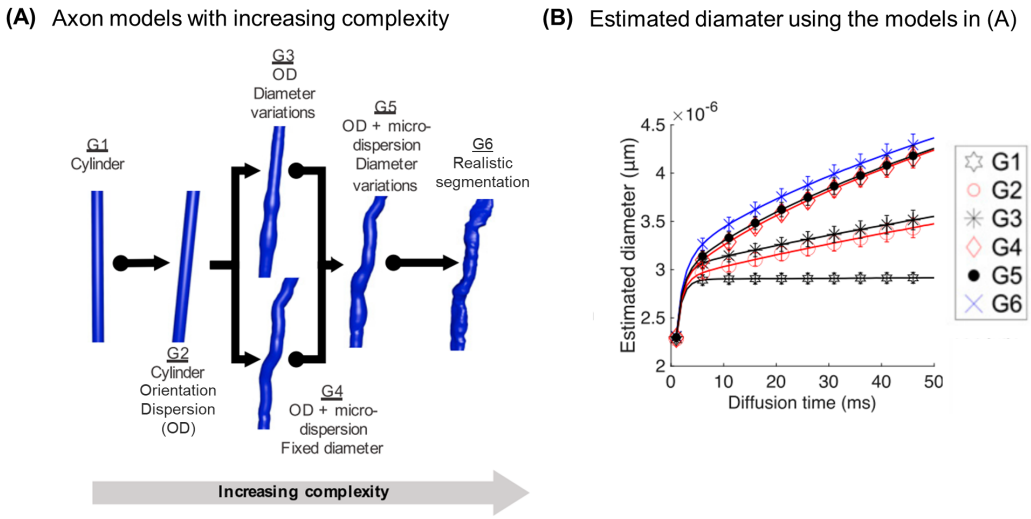

Fig. 1.4. Impact of along-axon radius variations on axon radius estimation. (A) Axon models with increased complexity (from G1 to G5 and a realistic segmentation of an axon G6). (B) Corresponding axon diameter estimates. The model of a perfect cylinder (G1) provides the correct simulated diameter of 2.9 μm. The increase in complexity of the substrate (G2 to G6) leads to an overestimation of the axon diameter, which increases with diffusion time. (Adapted with permission from Andersson et al. (2020)).

1.4 Fiber myelination

1.4.1 Background

Fibre myelination is another microstructural property of brain tissue contributing to the transmission of neuronal information and hence to brain function (MacKay and Laule, 2016; Lazari and Lipp, 2021). Changes in myelin content have been identified during brain development and healthy ageing (Peters, 2009; Ziegler et al., 2019). Moreover, demyelination is the hallmark of a range of neurological and psychiatric disorders, such as multiple sclerosis (Grossman and McGowan, 1998), autism (Zikopoulos and Barbas, 2010), schizophrenia (Stedehouder and Kushner, 2017), and Alzheimer's disease (Brun and Englund, 1986). Thus, the non-invasive assessment of myelin content may enable the study of myelin-related changes across healthy individuals and in a variety of pathological conditions.

1.4.2 Techniques for myelin mapping

Quantifying myelin *in vivo* involves MRI contrasts that are sensitive to the interactions between water molecules and the myelin sheath. Such interactions can be detected with longitudinal relaxation R_1 (Koenig, 1991), transverse relaxation R_2 (Laule et al., 2007), effective transverse relaxation R_2^* (Lee et al., 2012; Wharton and Bowtell, 2012; Stüber et al., 2014; Bagnato et al., 2018) and Magnetization Transfer(MT)-based metrics such as MT saturation (MTsat) (Laule et al., 2007; Helms et al., 2008b). Multi-compartment models of R_2 or R_2^*, such as Myelin Water Fraction (MWF) (Mackay et al., 1994; MacKay and Laule, 2016), can also be used to investigate the contribution of the different types of water content in the brain (e.g. water within myelin layers, intra- and extracellular water).

The magnetic properties of myelin also induce local fluctuations in the magnetic field, resulting in variations of the MRI signal phase. Such variations can be captured using quantitative susceptibility mapping (QSM) techniques (Deistung et al., 2017; Wharton and Bowtell, 2012; Li and Leigh, 2004; Duyn and Schenck, 2017).

Despite the wide use of MRI-based myelin contrasts in neuroscientific and clinical applications (e.g. Dick et al., 2012; Marques et al., 2017; Helbling et al., 2015), their specificity in measuring myelin is limited. For instance, MT is sensitive to various macromolecules beyond myelin (Pike, 1996) and R_2^* is influenced by iron content as well as other factors (section 1.6).

G-ratio imaging (g_{MRI}) is one approach that allows for improving the specificity of MRI-based myelin content estimation as it removes sensitivity to the absolute fibre volume fraction (FVF) when quantifying the relative myelin thickness (Stikov et al., 2015; Campbell et al., 2018). The g-ratio, defined histologically as the ratio between the inner and outer radius of the myelin sheath (Stikov et al., 2015, 2011; West et al., 2016), is inaccessible through *in vivo* measurements. Nonetheless, an ensemble average of g-ratios can be derived from MRI data (g_{MRI}) using voxel-averages of myelin volume fraction (MVF) and axonal volume fractions (AVF) (Fig. 1.5) (Stikov et al., 2015; Campbell et al., 2018). Despite its current implementation in investigations of brain health and disease (e.g. Hagiwara et al., 2017; Berman et al., 2018), g_{MRI} provides a weighted aggregated assessment of axonal myelination, therefore yielding a measure that is skewed towards larger axons (Campbell et al., 2018).

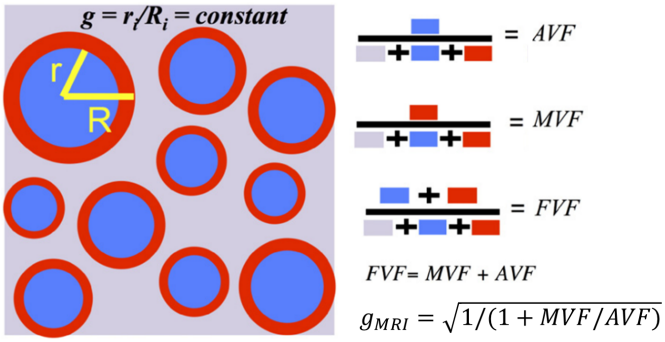

Fig. 1.5. G-ratio imaging. The aggregate g-ratio can be expressed as a function of the myelin volume fraction (MVF) and the axon volume fraction (AVF) or fibre volume fraction (FVF) (adapted with permission from (Stikov et al., 2015)).

Beyond g_{MRI}, other techniques have been proposed to improve MRI specificity to myelination. Given that MRI contrasts are often influenced by both myelin and iron content, novel methods have been proposed for the independent quantification of these quantities, thereby improving the specificity of each measure (section 1.6.2).

Overall, despite several available MRI-based markers of myelination, their sensitivity and specificity are still a matter of debate. Moreover, inconsistent reporting and differences in methodological approaches are some of the factors that prevent establishing a gold standard for MRI-based myelin imaging and thus, a myelin-sensitive brain biomarker (Lazari and Lipp, 2021; Mancini et al., 2020).

1.5 Fiber conduction velocity

Conduction velocity of action potentials along neuronal axons is a crucial property of functional brain networks. Conduction velocity has been shown to depend on axonal morphology (e.g. Rushton, 1951; Waxman and Bennett, 1972), specifically the axonal radius and g-ratio (Drakesmith et al., 2019). As discussed in sections 1.3 and 1.4, MRI has proven a valuable technique for the *in vivo* estimation of axonal radius and MRI g-ratio. Therefore, previous studies have used the dependency of conduction velocity on axonal morphology to deduce, from MRI measurements, the conduction velocity along white matter fibres (e.g. Berman et al., 2019). However, rather than using structural measures to estimate functional properties, integrating structural and functional modalities holds great potential to explore its relationship. For example, the concurrent non-invasive estimation of axonal radius and conduction velocities allowed for the identification of a linear correlation between the two measures in humans (Horowitz et al., 2015), which has not been demonstrated previously.

Functional measures of brain activity can be estimated through various non-invasive neuroimaging techniques, such as electroencephalography (EEG) and functional magnetic resonance imaging (fMRI). While standard fMRI has a very low temporal resolution as it is an indirect measure of neuronal activity, electrophysiology-based measures provide a direct measure of neuronal activity at a high temporal resolution (Helbling et al., 2015; Glover, 2011). Therefore, electrophysiological measures such as EEG are better suited for assessing conduction delays, and consequently, conduction velocities *in vivo*.

One useful approach for the estimation of conduction velocity with EEG is through the calculation of the interhemispheric transfer time (IHTT). IHTT is the delay of neuronal information transfer from one hemisphere to the other (Marzi, 1999). In the visual domain, it relies on the fact that each hemisphere has only access to one-half of the visual field. Thereby, a unilaterally-presented visual stimulus first reaches the contralateral hemisphere and is then transferred to the ipsilateral hemisphere (Fig. 1.6), via the splenium of the corpus callosum (Marzi, 1999). Classically, EEG-based estimation of IHTT is calculated by measuring the latency difference in evoked activity recorded from homologous electrodes in the two hemispheres (e.g.. Saron and Davidson, 1989; Brown and Jeeves, 1993). However, this calculation relies on the *ad hoc* selection of electrodes at which the transfer is most likely to take place and on the *ad hoc* identification of the EEG-evoked response component that underpins this transfer.

The visual IHTT is a valuable metric that has been used to investigate brain lateralization (Chaumillon et al., 2018) and the structural integrity of the corpus callosum (Westerhausen et al., 2006). However, the majority of studies predominantly focus on group-averaged IHTT measures, with limited attention given to single-subject analysis. Studies that do explore individual-level IHTT fail to provide consistent results across participants, and in some cases, counter-intuitively, even show negative IHTT values (Saron and Davidson, 1989; Marzi et al., 1991; Friedrich et al., 2017; Westerhausen et al., 2006). This outlines an important limitation of currently available techniques for the *in vivo* estimation of conduction velocities, especially when aiming to integrate structural and functional measures at the single-subject level.

Despite the achievements of IHTT-based measures of conduction velocity, recent more so-

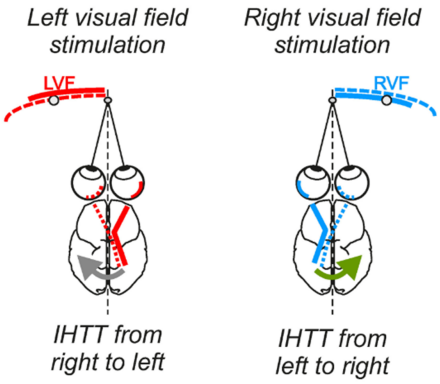

Fig. 1.6. Visual interhemispheric transfer time (IHTT). The estimation of visual IHTT relies on the crossed organization of the visual system: a unilaterally-presented visual stimulus first reaches the cortex contralateral to the stimulated visual field (red and blue pathways) and is then transferred to the ipsilateral cortex (grey and green arrows). IHTT is taken as the difference in latencies between the signal recorded in both hemispheres (adapted with permission from (Chaumillon et al., 2018)).

phisticated methods have been proposed to estimate axonal velocity *in vivo*. One noteworthy approach was proposed by Lemarechal et al. (2022), who introduced a biologically informed model that enables the estimation of axonal transmission delays from cortico-cortical evoked potentials. However, this method requires the use of invasive intracerebral depth electrodes and is therefore not applicable to non-invasive neuroimaging techniques.

An innovative approach that does not rely on invasive techniques was proposed by Sorrentino et al. (2022) with which single-subject and single-tract transmission delays can be estimated. The authors used resting-state magnetoencephalography and EEG data, to measure neuronal avalanches, which represent cascades of neural activity that propagate across different white matter tracts. Axonal transmission delays can then be derived based on the observed neuronal avalanches. The authors revealed a strong relationship between conduction velocity and lesioned white matter tracts in multiple sclerosis patients. However, the necessity for pre-defined methodological parameters such as bin length and branching value along with large coarse cortical parcellations, adds complexity to the widespread implementation of this method.

In an altogether different approach, the combination of EEG and diffusion MRI was used to non-invasively infer and visualize the flow of information through white matter tracts (Deslauriers-Gauthier et al., 2019). This approach was based on Bayesian networks and assumes a constant conduction velocity throughout the brain while estimating the white matter pathways involved in the information transfer during a given task. Their subsequent work (Deslauriers-Gauthier and Deriche, 2019) is built conceptually on their previous approach but differs on the estimated metrics. Instead of fixing the conduction velocity to estimate the flow of information along white matter tracts, they now fix the tract responsible for information transfer and focus on estimating its conduction time and consequently, conduction velocity.

Despite an important contribution to conduction velocity estimation, the aforementioned approaches rely on complex models, make numerous assumptions, and cannot be easily implemented *in vivo*. This highlights the potential advantages of adopting simpler, data-driven methods; a noteworthy example being the IHTT estimation.

1.6 Iron

1.6.1 Background

Iron is a chemical element naturally present in the brain that is involved in a number of physiological functions. Indeed, iron plays a crucial role in oxygen transportation, myelination, energy production, and neurotransmitter synthesis and signalling (Hare et al., 2013). While iron is naturally present in healthy brains, pathological iron accumulation is a hallmark of numerous disorders such as Alzheimer's disease, Parkinson's disease, and multiple sclerosis (Thompson et al., 2001; Zecca et al., 2004; Hare et al., 2013). Iron has also been shown to naturally accumulate in healthy ageing (Ward et al., 2014). Hence, *in vivo* assessment of iron content holds particular relevance. Specifically, characterization of the iron deposits located within brain tissue (Fig. 1.1B) may enable the identification of the mechanisms responsible for iron accumulation and improve the accurate and early diagnosis of neurodegenerative diseases.

1.6.2 Techniques for iron mapping

The *in vivo* quantification of iron content commonly involves relaxometry MRI measures, such as the longitudinal relaxation rate R_1 and the transverse relaxation rate R_2, due to the established correlation between iron concentration and R_1 (Brooks et al., 1998; Ogg and Steen, 1998) as well as R_2 (Bartzokis et al., 1994; Schenck, 1996; Vymazal et al., 1995; Graham et al., 2000). However, both these measures are also influenced by myelin content (Koenig, 1991; Laule et al., 2007) (section 1.4.2). Non-invasive iron characterization is also commonly carried out using R_2^* MRI measure. The strong link between R_2^* maps and iron concentration was demonstrated with *post mortem* brain tissue in the seminal work from Fukunaga et al. (2010) and Langkammer et al. (2010). Along the same lines, Péran et al. (2009) and Yao et al. (2009) have substantiated this relationship using *in vivo* data. Despite the potential of R_2^* to identify iron patterns in various neuroscientific applications (Deistung et al., 2013; Kirilina et al., 2020; Duyn et al., 2007), this map is also affected by variations in myelin content within neuronal tissues (Lee et al., 2012; Wharton and Bowtell, 2012; Stüber et al., 2014; Bagnato et al., 2018). This may be problematic, as myelin and iron colocalize in some cortical areas (Fukunaga et al., 2010) (Figure 1.7).

Similarly to myelin, the magnetic susceptibility of iron also contributes to the MRI phase contrast and therefore, QSM (Haacke et al., 2015; Deistung et al., 2017). QSM maps have been instrumental in quantifying iron content in numerous studies, including in healthy ageing (Bilgic et al., 2012) or in deep grey matter structures (Langkammer et al., 2012).

In QSM, myelin and iron contribute to the MRI contrast with opposing effects: myelin is diamagnetic and thus has negative susceptibility while iron is paramagnetic, having positive susceptibility. This difference makes the interpretation of QSM measures challenging, which Shin et al. (2021) elegantly attempted to address with the χ-separation technique. This model attempts to separate paramagnetic and diamagnetic susceptibility sources. The χ-separation approach was validated with simulations, phantoms, *ex vivo*, and *in vivo* data of healthy volunteers and multiple sclerosis patients, demonstrating its viability in improving the specificity to iron *in vivo*.

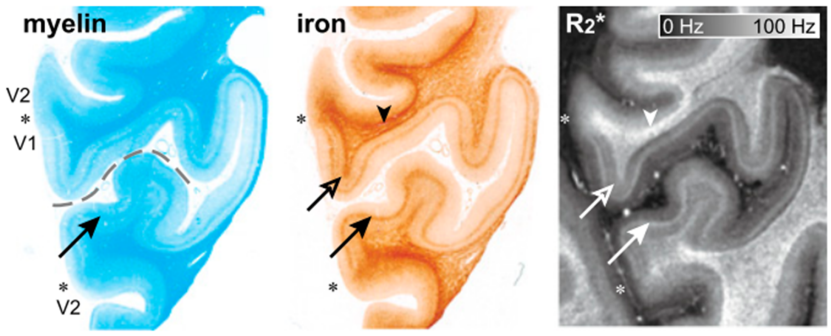

Fig. 1.7. Myelin (left panel) and iron (middle panel) histochemical stains of the primary and secondary visual cortices, as well as a R_2^* map (right panel) of the same region. As is evident, iron and myelin often colocalize within the visual cortex. The calcarine sulcus is labelled as the dashed line and the boundaries between primary (V1) and secondary (V2) visual cortices by the asterisk. The different arrows indicate the similarities between the iron and myelin stain to the R_2^* map (adapted with permission from (Fukunaga et al., 2010)).

Similarly aimed at improving the specificity of iron measures, other methods have been proposed for the independent estimation of iron and myelin concentrations, by combining complementary quantitative contrasts. Stüber et al. (2014) proposed a multivariate regression model of R_1, R_2^* and magnetic susceptibility as a function of iron and myelin concentration. Despite the *ex vivo* validation of this technique, its *in vivo* application remains challenging, as was demonstrated from an *in vivo* study which yielded physiologically improbable iron and myelin maps (Marques et al., 2017). An earlier study by Schweser et al. (2011a) attempted to obtain iron-induced myelin-free susceptibility maps by subtracting the concurrent effects of myelin (obtained using MT maps). In their later work, myelin effects were not removed but estimated independently of iron content (Schweser et al., 2011b). However, it is worth noting, that these three approaches (Stüber et al., 2014; Schweser et al., 2011a,b), primarily rely on an empirical relationship between iron/myelin content and the MRI data and thus lack a biophysical foundation, a crucial point for attaining specificity and for correct interpretation of the results (Novikov et al., 2018).

While current methods offer voxel-average estimations of iron content, they fall short of fully capturing the microstructural features of the magnetic material within brain tissue. On the contrary, theoretical studies have made significant contributions in modelling the impact of magnetic deposits within brain tissue (e.g. iron-loaded cells, myelin) on the MRI signal decay due to transverse relaxation (Yablonskiy and Haacke, 1994; Jensen and Chandra, 2000; Sukstanskii and Yablonskiy, 2003; Anderson and Weiss, 1953). Such models have enabled the estimation of volume fractions, size or magnetic susceptibilities of the magnetic deposits in numerous cases, such as, in suspensions of paramagnetic beads (Storey et al., 2015), *in vitro* red blood cell suspensions, *ex vivo* brain samples (Jensen and Chandra, 2000), and *in vivo* blood vessels (Ulrich and Yablonskiy, 2016). However, these theoretical formulations have yet to be applied for iron quantification *in vivo*, leaving the voxel-average measures (e.g. R_2^*) as the primary approach for identifying iron-related microscopic brain changes.

1.7 Objectives

This thesis comprises two distinct projects, each focusing on different aspects of brain tissue characterization *in vivo*.

In the first project, we aimed to characterize the morphology of axons within a white matter tract, in particular the radius and myelination of the underlying axonal fibres (Fig. 1.1A). Despite the promising outcomes demonstrated by the current axon radius mapping techniques (section 1.3), challenges such as the need for high gradient strength and long scan times limit their application. Additionally, the high sensitivity of the MRI signal to the extra-axonal water also leads to an overestimation of axon radius by diffusion-based MRI methods. Moreover, none of the existing approaches appears to simultaneously estimate axonal radius and fibre myelination, two fundamental morphological properties of axons that can allow for a more comprehensive assessment of the white matter. To address these limitations and accomplish our objective, we propose a novel biophysical model for the estimation of axonal radius distribution and relative fibre myelin thickness of the axons composing a given white matter tract. This method combines EEG-based measures of conduction velocity with MRI-based structural measures of relative myelin thickness (MRI g-ratio) acquired along the white matter tract under evaluation, which in this case was the visual transcallosal tract.

While the measurement of MRI g-ratio from MRI data (section 1.4) is relatively straightforward, the measurement of conduction velocities from EEG (section 1.5) is more complex. A potential approach for the estimation of conduction velocities *in vivo* is via the estimation of IHTT. However, IHTT estimation is classically performed based on scalp measurements, relying on a few *ad hoc* analysis decisions. Moreover, IHTT estimation at the single-subject level remains challenging. To address these limitations, we estimate IHTT at the cortical origins of the electrode-level measured activity using source reconstruction techniques. Our proposed framework is based on a data-driven evaluation of the maximal peak of the source-level neural response to visual stimuli with minimal *a priori* constraints. This framework also allows for the single-subject measurement of the IHTT from EEG data.

In the second project, we aimed to characterise the distribution of iron deposits in subcortical grey matter tissue (Fig. 1.1B). Although numerous methodologies have been proposed for the *in vivo* quantification of iron content (section 1.6), these techniques provide voxel-averaged estimations of iron content. Therefore, here we aim to address this limitation by estimating microstructural features with increased specificity to the iron deposits, such as their magnetic susceptibility (proportional to the concentration of iron within the deposit), radius and volume fraction. To achieve this, we apply existing biophysical models of the effect of magnetic deposits within brain tissue on the MRI signal. To the best of our knowledge, this is the first account of these theoretical models being implemented for the *in vivo* quantification of iron content in subcortical grey matter regions.

Chapter 2

Non-exponential transverse relaxation decay in subcortical grey matter

2.1 Introduction

In MRI data, the decay of the gradient-echo signal due to transverse relaxation is widely considered to follow an exponential behaviour with a rate R_2^* (Weiskopf et al., 2014). Estimates of R_2^* correlate with iron concentration within brain tissue (Péran et al., 2009; Yao et al., 2009; Fukunaga et al., 2010; Langkammer et al., 2010), a property of primary importance for the study of the brain. Iron indeed plays a crucial role in various biological processes such as myelin synthesis, energy production, and neurotransmitter synthesis and signalling (Hare et al., 2013; Möller et al., 2019). Abnormal accumulation of iron also constitutes a hallmark of neurodegenerative disorders such as Parkinson's Disease (Gerlach et al., 1994; Thompson et al., 2001; Ward et al., 2014). As a result, R_2^* mapping data are used extensively for the monitoring of iron-related brain changes for instance in neurodegenerative diseases (Ulla et al., 2013; Damulina et al., 2020).

However, deposits of magnetic material within brain tissue such as iron-loaded cells, myelin, or blood vessels, induce microscopic inhomogeneities of the magnetic field which can result in a non-exponential signal decay (Haacke et al., 2005; Kiselev and Novikov, 2018). According to theoretical studies, such decay displays a gaussian behaviour at short echo times followed by an exponential behaviour at longer echo times (Yablonskiy and Haacke, 1994; Jensen and Chandra, 2000; Kiselev and Novikov, 2002, 2018; Sukstanskii and Yablonskiy, 2003). While this behaviour has been reported in suspensions of paramagnetic beads (Storey et al., 2015), in *ex vivo* brain samples (Jensen and Chandra, 2000) and *in vivo* blood vessels (Ulrich and Yablonskiy, 2016), no evidence has been presented from iron-rich subcortical grey matter regions *in vivo*.

The mechanisms that underlie transverse relaxation in the presence of magnetic deposits can be described under two limiting regimes. In the static dephasing regime (SDR), water diffusion is assumed to be negligible and signal decay arises from the spatial inhomogeneities of the magnetic field generated by the deposits. In the diffusion narrowing regime (DNR) (Jensen

and Chandra, 2000; Sukstanskii and Yablonskiy, 2003), signal decay arises primarily from the diffusion of water molecules across these spatial inhomogeneities. The large differences in the relaxation rate measured from spin-echo and gradient-echo data come in support of the SDR as a plausible mechanism for transverse relaxation in subcortical grey matter regions (Sedlacik et al., 2014; Brammerloh et al., 2021). On the other hand, investigations of the relationship between R_2^* and MRI measures of magnetic susceptibility in the basal ganglia have suggested the DNR as the most plausible regime (Yablonskiy et al., 2021).

In this work, we provide experimental evidence of non-exponential MRI signal decay due to transverse relaxation in subcortical brain regions, in gradient-echo data acquired *in vivo* at 3T. We fitted the signal decay with theoretical models of the effect of magnetic deposits within brain tissue on the MRI signal (Anderson and Weiss, 1953; Jensen and Chandra, 2000; Sukstanskii and Yablonskiy, 2003). From the model parameter estimates of the gaussian and exponential parts of the signal decay, we assessed the properties of the magnetic deposits within the tissue at the source of the transverse relaxation, under the assumption of SDR and DNR regimes.

2.2 Theory

2.2.1 Transverse relaxation in the presence of magnetic material

Existing biophysical models of transverse relaxation in biological tissues are based on the diffusion of water molecules across the inhomogenous magnetic field created by magnetic deposits (Anderson and Weiss, 1953; Jensen and Chandra, 2000; Sukstanskii and Yablonskiy, 2003). In the model of Anderson and Weiss (1953) (AW), the auto-correlation function of the Larmor frequency experienced by diffusing water molecules is assumed to take an exponential form. With the model of Sukstanskii and Yablonskiy (2003) and Jensen and Chandra (2000) (SY) the auto-correlation function was derived from the analytical expression of spin displacements due to diffusion within brain tissue. Alternatively, we derived a parametric expression for the signal decay from the Padé approximation of a transition from gaussian to exponential decay. The Padé approximation constitutes a flexible parametric approach that does not rely on a specific set of assumptions. While it lacks a theoretical basis, we refer henceforward to all three analytical expressions as models of the MRI signal for the sake of simplicity.

With the Padé, AW, and SY models, the decay of the MRI signal due to transverse relaxation is written as:

$$S_{Pade} = S_0 \cdot \exp\left(-\frac{\langle\Omega^2\rangle T_E^2}{2(1+\frac{\langle\Omega^2\rangle}{2R^*_{2,micro}}T_E)} - R_{2,nano}T_E\right) \tag{2.1}$$

$$S_{AW} = S_0 \cdot \exp\left(-\frac{{R^*_{2,micro}}^2}{\langle\Omega^2\rangle}\left(\frac{\langle\Omega^2\rangle}{R^*_{2,micro}}T_E + e^{-\frac{\langle\Omega^2\rangle}{R^*_{2,micro}}T_E} - 1\right) - R_{2,nano}T_E\right) \tag{2.2}$$

$$S_{SY} = S_0 \cdot \exp\left(-\frac{{R^*_{2,micro}}^2}{\langle\Omega^2\rangle}\left(\frac{\langle\Omega^2\rangle}{R^*_{2,micro}}T_E - \sqrt{1+2\frac{\langle\Omega^2\rangle}{R^*_{2,micro}}T_E} + 1\right) - R_{2,nano}T_E\right) \tag{2.3}$$

where S_0 is the signal amplitude at T_E=0 and $R_{2,nano}$ is the transverse relaxation rate due to spin-spin interactions at the molecular/nanoscopic scales. $\langle\Omega^2\rangle$ is the mean square frequency deviation of the field inhomogeneities induced by the magnetic deposits (Novikov et al., 2018) and drives the behaviour of the signal decay at short echo times ($S = S_0 \cdot e^{-\frac{1}{2}\langle\Omega^2\rangle {T_E}^2}$ with $T_E \lesssim \frac{R^*_{2,micro}}{\langle\Omega^2\rangle}$). The transverse relaxation rate $R^*_{2,micro}$ drives the behaviour of the signal decay at long echo times ($S = S_0 \cdot e^{-R^*_{2,micro}T_E}$ with $T_E \gtrsim \frac{R^*_{2,micro}}{\langle\Omega^2\rangle}$).

The commonly used exponential model is written as:

$$S_{Exp} = S_0 \cdot \exp\left(-R^*_2 T_E\right) \tag{2.4}$$

with $R^*_2 = R^*_{2,micro} + R_{2,nano}$.

2.2.2 Microscopic underpinnings of non-exponential decay

For magnetic deposits with simple geometries, the signal decay parameters ($R^*_{2,micro}$ and $\langle\Omega^2\rangle$) can be linked explicitly with the microstructural properties of the magnetic material within brain tissue. The mean square frequency deviation $\langle\Omega^2\rangle$ of the magnetic field inhomogeneities generated by randomly distributed spherical deposits is (Yablonskiy and Haacke, 1994; Jensen and Chandra, 2000; Sukstanskii and Yablonskiy, 2003):

$$\langle\Omega^2\rangle = \frac{4}{5}\zeta\left(\frac{1}{3}\gamma B_0\right)^2 \Delta\chi^2 \tag{2.5}$$

where ζ is the volume fraction of the magnetic deposits, $\Delta\chi$ is their susceptibility difference with the surrounding tissue (SI units), γ the gyromagnetic ratio (2.7·10^8 $rad\ s^{-1}T^{-1}$) and B_0 the main magnetic field. Note that $\langle\Omega^2\rangle$ is an average measure of field inhomogeneities within a voxel and differs from the frequency deviation generated by an individual magnetic deposit: $\delta w_s = \frac{1}{3}\gamma B_0\ \Delta\chi$.

In the framework of the SDR (Yablonskiy and Haacke, 1994) and DNR (Jensen and Chandra, 2000; Sukstanskii and Yablonskiy, 2003) the relaxation rate is described by the following equations:

$$R^*_{2,micro} = \lambda_{SDR}\zeta\gamma B_0\Delta\chi, \quad \lambda_{SDR} = 1.2092 \cdot \frac{1}{3} \tag{2.6a}$$

$$R^*_{2,micro} = \lambda_{DNR}\zeta\gamma^2 B_0^2\Delta\chi^2\tau, \quad \lambda_{DNR} = \frac{8}{225} \cdot 6 \tag{2.6b}$$

where $\tau = \frac{r^2}{6D}$ is the time scale for water molecules to diffuse away from magnetic deposits with spherical geometry (radius r). D is the water diffusion coefficient (1 μm^2/ms).

In the DNR, the dimensionless parameter $\alpha = \tau\sqrt{\langle\Omega^2\rangle}$ (Storey et al., 2015; Kiselev and Novikov, 2018) represents the amount of spin dephasing induced by the field inhomogeneities over the period τ. $\alpha \ll 1$ is consistent with the assumptions of the DNR.

2.3 Methods

2.3.1 Participant cohort

MRI data were acquired from 5 healthy volunteers (2 females, mean age=31.8$\pm$9 years old). The study received approval by the local ethics committee and all volunteers gave written informed consent for their participation.

2.3.2 Data acquisition

MRI data were acquired on a 3T whole-body MRI system (Magnetom Prisma; Siemens Medical Systems, Erlangen, Germany) with a 64-channel receive head coil. The MRI protocol consisted of multi-echo 3D fast low-angle shot (FLASH) acquisitions with a bipolar readout. Image resolution was 1.2 mm^3 isotropic, with a field of view 144$\times$192$\times$208. 16 gradient-echo images were acquired with an echo time T_E ranging from 1.25 to 19.25 ms, with 1.2 ms inter-echo spacing (repetition time T_R = 23.2 ms). Partial Fourier (factor 6/8) was used in the phase and partition directions. Three repetitions were conducted on each participant and the total nominal acquisition time was 18min09s.

A prospective motion correction system (KinetiCor, HI, Honolulu) was used to reduce image degradation due to patient motion (Zaitsev et al., 2006; Maclaren et al., 2012). To further preserve image quality in the event of head motion, data acquisition was automatically suspended during periods of excessive head movement as described in Castella et al. (2018) (ΔMew_{th}= 3.5e^{-4} mm s^{-1}). To minimize the effect of cardiac-induced noise on the images, data acquisition was suspended during the systolic period of the cardiac cycle, taken to last for a duration of 300 ms (Raynaud et al., 2022). For a heart rate of 80 beats per minute, this resulted in an increase in scan time by approximately 40%. The quality index of the data lay within a narrow range across participants and did not exceed 3.7 s^{-1}, indicative of high-quality data (Castella et al., 2018; Lutti et al., 2022).

For the computation of MTsat maps (Helms et al., 2008a), multi-echo 3D FLASH images were acquired with magnetization transfer-, proton density- and T1-weighted contrasts (radio-frequency excitation flip angle = 6°, 6° and 21°, respectively; repetition time T_R=24.5 ms). 8 echo images were acquired for the T1- and proton density-weighted contrasts and 6 for the magnetization transfer-weighted contrast. Image resolution was 1 mm^3 isotropic, and the image field of view was 176$\times$240$\times$256mm. B1-field mapping data was acquired (4 mm^3 voxel size, TR/TE = 500/39.1 ms) to correct RF transmit field inhomogeneity effects on the MTsat maps (Lutti et al., 2010, 2012). For correction of image distortions in the B1 map data, B0-field map data was acquired with a 2D double-echo FLASH, T_R=1,020 ms, α=90 °, TE1/TE2 = 10/12.46 ms, BW = 260 Hz/pixel, slice thickness = 2 mm.

2.3.3 Anatomical imaging processing

MTsat maps were calculated from the magnetization transfer-, proton density- and T1-weighted images with the hMRI toolbox (Tabelow et al., 2019), as described in Helms et al. (2008b,a). MTsat maps were segmented into grey and white matter tissue probability maps using the

Statistical Parametric Mapping software (SPM12, Wellcome Centre for Human Neuroimaging, London) (Ashburner and Friston, 2005). A grey matter mask was computed by selecting voxels with a grey matter probability above 0.95. As B0-field inhomogeneities affect transverse relaxation, regions with inhomogeneous field (e.g. orbitofrontal cortex, inferior temporal lobe, amygdala) were removed from the grey matter mask. Globus pallidus (GP), putamen, thalamus, and caudate regions of interest (ROI) were defined from the grey matter mask and the regional labels of the Neuromorphometrics atlas (http:// neuromorphometrics.com/). As no label exists for the substantia nigra (SN), this region was delineated using an *ad hoc* procedure, from a cuboid placed appropriately in the space of each MTsat map. Within this cuboid, SN voxels were identified from the grey matter voxels labelled as brainstem and ventral diencephalon in the Neuromorphometrics atlas.

2.3.4 Fitting of the transverse relaxation decay

Data were analyzed using bespoke analysis scripts written with MATLAB (The Mathworks, Natick, MA). The gradient-echo data was denoised using the Marchenko Pastur-PCA method described in (Does et al., 2019). The PCA decomposition of the signal decay was conducted from the raw signals within the grey matter mask in cubic regions of 8x8x8 voxels. At each voxel, we removed scaling and additive effects between the signal decays acquired across repetitions, due to e.g. head motion in the spatially varying sensitivity profile of the receive coil. To suppress the noise floor in the magnitude images, background voxels outside the head were identified from the segmentation of the first gradient-echo image using SPM12 segmentation (Ashburner and Friston, 2005). The distribution of signal intensities across noise voxels was fitted assuming a Rician distribution and the resulting value of the noncentrality parameter was deducted from the signal intensities.

Fitting of the transverse relaxation decay with the analytical models of Section 2.2.1 involved the multi-echo data acquired across all repetitions simultaneously and was conducted using a dictionary-based approach. The columns of the dictionary contained signal decays predicted by all combinations of model parameter values. For all models, the $R^*_{2,micro}$ ranged from 1e^{-3} to 80e^{-3} ms^{-1}. The $\langle\Omega^2\rangle$ parameter ranged from 1e^{-4} to 4e^{-2} ms^{-2} for the Padé and AW models and from 1e^{-4} to 8e^{-2} ms^{-2} for the SY model. $R_{2,nano}$ was set to 10 s^{-1} (Jensen and Chandra, 2000; Sedlacik et al., 2014; Brammerloh et al., 2021). To facilitate the visualization of the signal decays, both the data and dictionary columns were low-pass filtered prior to fitting, with a Butterworth filter of order 5 and a cut-off frequency of 0.2 of the Nyquist rate. At each voxel, fitting the multi-echo data involved estimating the value of S_0 for each column of the dictionary. The solution was the set of parameter values of the dictionary column where the fitting residual was minimum.

The goodness of fit of each model was estimated from the mean squared error of the fit (MSE) and the Akaike Information Criterion (AIC), which includes a penalty for model complexity. Lower MSE and AIC values indicate a better model fit. Model parameter estimates for the five regions of interest were extracted from all voxels and all subjects after the removal of the voxels where MSE$>$10, indicative of spurious effects in the data such as physiological noise. We also excluded voxels where the transition from gaussian to exponential behaviour took place over a

timescale $\frac{R^*_{2,micro}}{\langle\Omega^2\rangle}$ <0.5 ms, too short to be robustly detectable.

2.3.5 Microscopic underpinnings of non-exponential decay

From the estimates of $R^*_{2,micro}$ and $\langle\Omega^2\rangle$ at each voxel, we estimated the properties of the magnetic deposits within brain tissue at the source of the non-exponential decay. Under the assumption of the SDR, we estimated the magnetic susceptibility ($\Delta\chi$) and volume fractions (ζ) of the deposits (Eqs. 2.5 and 2.6a). From the values of $R^*_{2,micro}$, we also computed estimates of the MRI magnetic susceptibility, usually computed using QSM techniques (Li and Leigh, 2004; Schweser et al., 2011b; Deistung et al., 2017):

$$\chi_{MRI} = \zeta\Delta\chi = \frac{R^*_{2,micro}}{1.209\frac{1}{3}\gamma B_0} \tag{2.7}$$

Under the assumption of the DNR, the model parameters $R^*_{2,micro}$ and $\langle\Omega^2\rangle$ depend on 3 properties of the magnetic deposits ($\Delta\chi$, ζ, and τ), which cannot be estimated from $R^*_{2,micro}$ and $\langle\Omega^2\rangle$ alone. We estimated α and τ instead (Eqs. 2.5 and 2.6b).

We conducted non-parametric Kruskal-Wallis statistical tests of inter-regional differences in the estimates of $\Delta\chi$ and ζ obtained under the assumption of the SDR (*kruskalwallis* function in Matlab). Post-hoc Tukey's HSD tests were conducted subsequently to identify the pairs of regions at the source of these differences (*multcompare* function in Matlab). To quantify the magnitude of differences between regions, the effect size was computed using the cliff's delta. The AW model was used as an example for this statistical analysis.

2.4 Results

2.4.1 Non-exponential transverse decay in basal ganglia and thalamus

At short echo times (T_E <5-10ms), transverse signal decay in the basal ganglia and thalamus (Fig. 2.1) displays systematic deviations from exponential behaviour (green line in Fig. 2.1): the log-signal exhibits a quadratic form, with a transition towards a linear dependence at long times. This behaviour is consistent with the effect of magnetic deposits on the MRI signal predicted by theoretical studies (Yablonskiy and Haacke, 1994; Jensen and Chandra, 2000; Sukstanskii and Yablonskiy, 2003)

The non-exponential models of transverse relaxation (AW, SY, Padé) can account for the non-exponential decay of the MRI signal at short times, leading to an improved fit of the data (Fig. 2.2A). The residual levels are largely consistent across the non-exponential models (MSE $\sim$1.3), a factor of $\sim$3-4 smaller than the exponential model (Fig. 2.2B). The differences in the values of the AIC ($\sim$60, Fig. 2.2C) show that this residual decrease goes beyond that expected from the higher number of parameters with non-exponential models.

The ratio of the MSE from the exponential fit over those from the non-exponential fits is higher in subcortical regions (average $\sim$6) than in cortical grey matter (average $\sim$3, Fig.2.3). This shows that non-exponential signal decays take place primarily in subcortical regions.

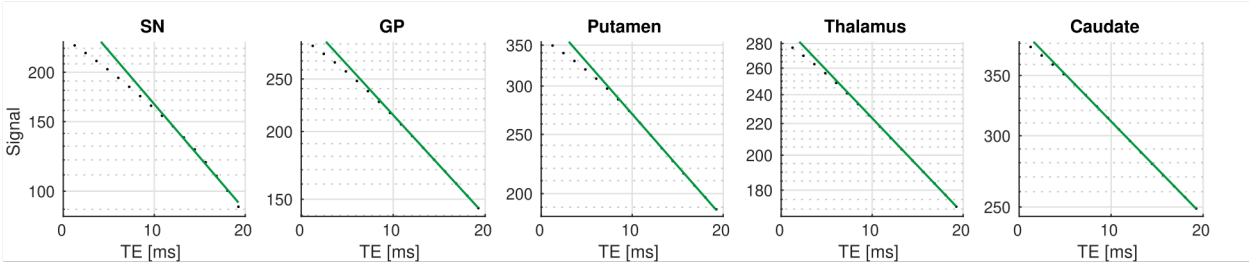

Fig. 2.1. Example transverse relaxation decays in the basal ganglia and thalamus (semilog-scale). The green line shows the exponential decay fit at long echo times (T_E >10ms). At short echo times (T_E ∼<5ms), the data displays a quadratic decay consistent with the effect of magnetic deposits on the MRI signal predicted by theoretical studies (Yablonskiy and Haacke, 1994; Jensen and Chandra, 2000; Sukstanskii and Yablonskiy, 2003)

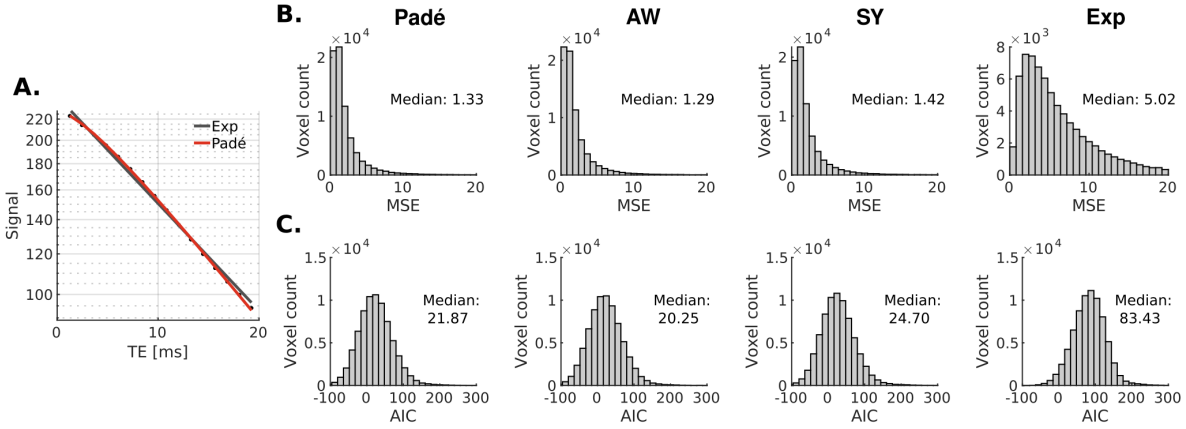

Fig. 2.2. Residual levels across signal models. Non-exponential models of transverse relaxation (e.g. Padé) can account for the non-exponential decay at short times, leading to an improved fit of the data (A). As a result, the residual levels (MSE) are reduced by ∼3-4 across subcortical regions, consistently for all non-exponential models (B). This residual decrease leads to a decrease of the AIC by ∼60 - beyond that expected from the higher number of parameters of non-exponential models (C).

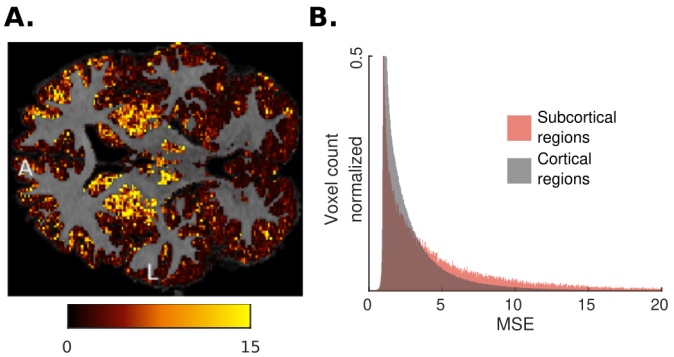

Fig. 2.3. Example spatial distribution of the ratio of the MSE from the exponential fit over the Padé signal model fit (A). The higher ratio values in subcortical regions (average ∼6) indicate that the strongest deviations from exponential behaviour take place in these areas (B). L – left; A – anterior.

2.4.2 Estimates of the MRI signal model parameters

Non-exponential signal decays were reliably detected with $\frac{R^*_{2,micro}}{\langle\Omega^2\rangle}$ >0.5 ms in 88/83/88/84/87% of voxels in the SN/GP/putamen/thalamus/caudate respectively. In these voxels, the non-

exponential models (Padé, AW, SY) lead to estimates of $R^*_{2,micro}$ that are respectively 37%, 30%, and 54% higher than the exponential model (Fig. 2.4A).

The estimates of $R^*_{2,micro}$ and $\langle\Omega^2\rangle$ are spatially organised and are consistent between anatomical regions (Fig. 2.4). The values of $R^*_{2,micro}$ and $\langle\Omega^2\rangle$ are higher in the GP and the SN, consistent with histological measures of iron concentration in brain tissue (Hallgren and Sourander, 1958) and with the expected dependence of these parameters on iron content (Eqs. 2.5 and 2.6).

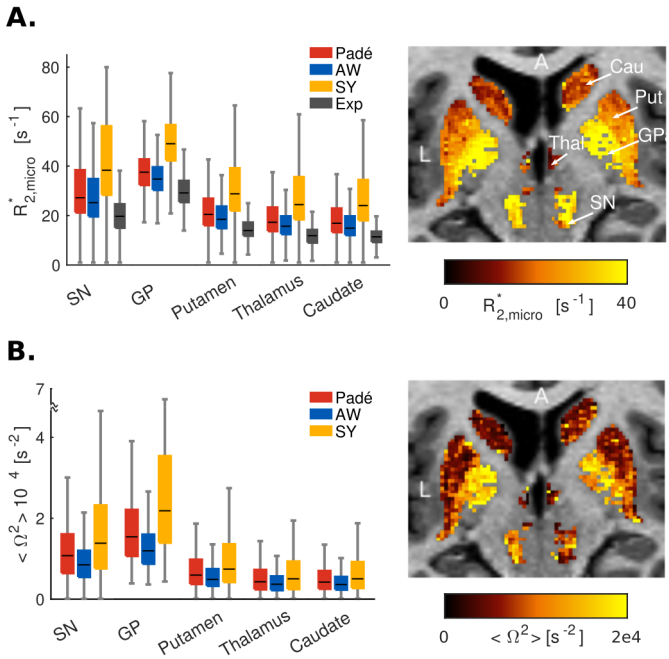

Fig. 2.4. Non-exponential model parameter estimates. Estimates of $R^*_{2,micro}$ (A) and $\langle\Omega^2\rangle$ (B) are highest in the GP followed by the SN, in agreement with histological measures of iron concentration (Hallgren and Sourander, 1958) and Eqs. 2.5 and 2.6. The example maps of $R^*_{2,micro}$ and $\langle\Omega^2\rangle$ were obtained from the AW model. L – left; A – anterior; Cau – caudate; Put – putamen; GP – globus pallidus; Thal – thalamus; SN – substantia nigra.

The SY model yields systematically higher values of $R^*_{2,micro}$ and $\langle\Omega^2\rangle$ than the AW and Padé models ($\sim$30-50%). This arises from the square-root term in the SY signal equation (Eq. 2.3), which brings a slow modulation of the signal over the range of echo times. As a result, the decay rate at very large echo times predicted by the SY model ($R_2(\infty)$) shows a steeper slope than the one observable experimentally (Fig. 2.5). On the other hand, the AW model converges to an exponential decay faster and the predicted decay rate at long echo times matches the slope of the data. Results from the Padé and AW models are largely consistent.

2.4.3 Characterization of magnetic deposits within subcortical tissue

From the estimates of the MRI signal parameters $R^*_{2,micro}$ and $\langle\Omega^2\rangle$, we characterized the properties of the magnetic deposits present within brain tissue, at the source of the non-exponential decay. Under the assumption of the SDR, the estimates of $R^*_{2,micro}$ and $\langle\Omega^2\rangle$ were used to estimate the volume fraction (ζ) and magnetic susceptibility ($\Delta\chi$) of the deposits (Eqs. 2.5 and 2.6a). Iron-rich regions such as the GP and SN display larger values of ζ (median value: 0.056

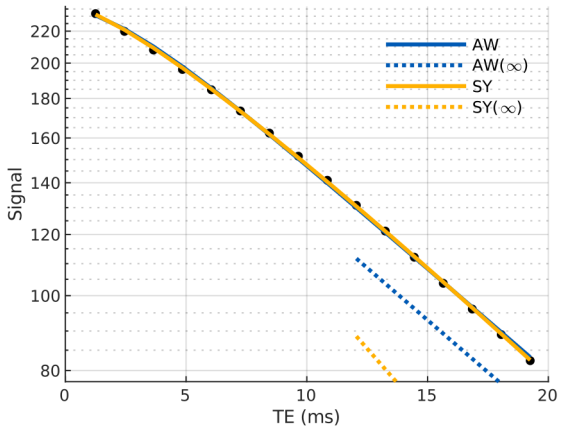

Fig. 2.5. Example transverse relaxation decay and fit with the AW (solid blue line) and SY (solid yellow line) models. Semi-log scale. The dashed lines correspond to the asymptotic behaviour of each model in the long-time limit $R_2(\infty)$. The slow convergence of the SY model towards an exponential decay leads to systematic differences between $R_2(\infty)$ and the decay rate observable experimentally.

and 0.044 from the AW signal model respectively, Fig. 2.6) followed by the putamen (0.038) and caudate and thalamus (0.033). The SY model yields higher estimates of ζ due to the systematic differences in the $R^*_{2,micro}$ and $\langle\Omega^2\rangle$ estimates highlighted above. The median of the estimates of the magnetic susceptibility of the deposits ($\Delta\chi$ ranges from 1.2 to 2.7 ppm. They are larger in the GP and SN (median $\Delta\chi$ ∼2.0 ppm and 1.8 ppm respectively from the AW signal model), followed by the putamen ($\Delta\chi$ ∼1.6 ppm) and caudate and thalamus ($\Delta\chi$ ∼1.4 ppm). Assuming that ferritin is the only source of magnetic material within the deposits, these estimates of $\Delta\chi$ indicate iron concentrations (Schenck, 1992) of ∼1.4, 1.5, 1.2, 1.1, and 1.1 mg/g in the SN, GP, putamen, thalamus and caudate, respectively, at a temperature of 310K and assuming a brain tissue density ρ ∼1.05 g/cm^3 (Barber et al., 1970).

The Kruskal-Wallis tests revealed statistically significant differences in $\Delta\chi$ between at least two ROIs (F(4, 69373) = [1154], p $<$ 0.001). The Tukey's HSD tests for multiple comparisons found significant differences between $\Delta\chi$ estimates from all ROIs (p$<$0.001) with small effect sizes, except between the thalamus and caudate where no significance was found. The SN and GP showed the strongest effect sizes ($>$0.14) compared to the remaining regions.

Similarly, the Kruskal-Wallis tests revealed statistically significant differences in ζ between at least two ROIs (F(4, 69373) = [612], p $<$ 0.001). Tukey's HSD tests showed significant differences between the ζ estimates from the GP and those from the putamen, thalamus, and caudate with the largest effect size ($>$0.30). Other inter-regional differences (except those between the thalamus and caudate) were found significant (p$<$0.01) with small effect sizes ($<$0.15).

Under the assumption of the DNR (Fig. 2.7), the estimates of $R^*_{2,micro}$ and $\langle\Omega^2\rangle$ were used to compute the value of the parameters τ and α (Eqs. 2.5 and 2.6b). The estimates of τ are larger in the putamen, thalamus, and caudate (median ∼1.6 ms) than in the SN and GP (median ∼1.1 ms). A typical value of τ ∼1.5 ms suggests that the magnetic field inhomogeneities generated by the deposits have a typical radius r∼3 μm, in the order of a typical cell size. The value of α is similar across regions (median ∼0.11-0.16), consistent with the assumption of the DNR ($\alpha \ll 1$).

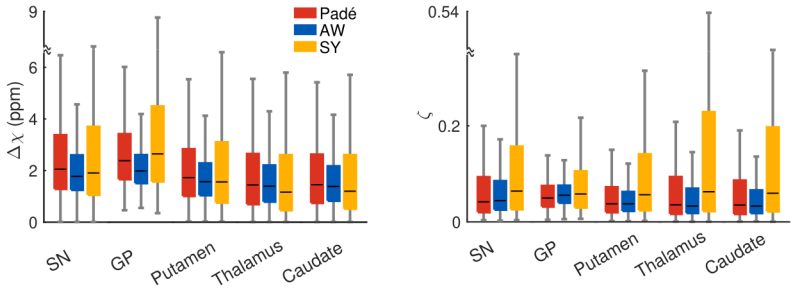

Fig. 2.6. Properties of the magnetic deposits present within brain tissue, estimated from the values of $R^*_{2,micro}$ and $\langle\Omega^2\rangle$ under the assumption of the SDR. The magnetic susceptibility of the deposits is larger in the SN and GP ($\Delta\chi$ ∼2 ppm) compared to the remaining regions ($\Delta\chi$ ∼1.4 ppm). The GP exhibits the largest volume fraction of deposits (ζ ∼0.06).

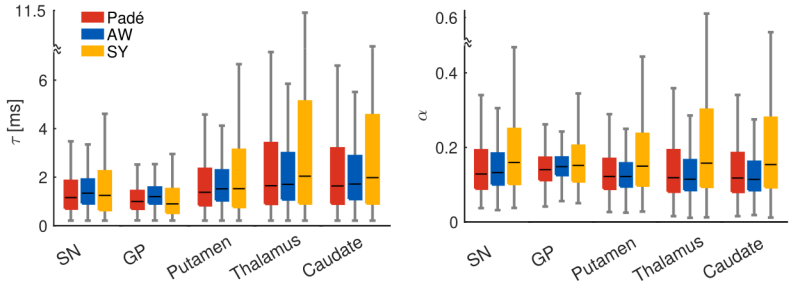

Fig. 2.7. Properties of the magnetic deposits present within brain tissue, estimated from the values of $R^*_{2,micro}$ and $\langle\Omega^2\rangle$ under the assumption of the DNR. The characteristic diffusion times τ are larger in the putamen, thalamus, and caudate (∼1.6 ms) compared to SN and GP (∼1.1 ms). The corresponding estimates of the radius of the magnetic field inhomogeneities generated by the deposits (r ∼3 μm) are in the order of a typical cell size. α values are similar across regions (∼0.11-0.16) and consistent with the assumption of the DNR.

Under the assumption of the SDR, estimates of the MRI magnetic susceptibility (χ_{MRI}) were computed from the estimates of ζ and $\Delta\chi$ (Eq. 2.7). With the AW and Padé models, the χ_{MRI} estimates are ∼0.11 ppm in the GP, ∼0.08 ppm in the SN, ∼0.06 ppm in the putamen, and ∼0.05 ppm in the thalamus and caudate (Fig. 2.8). The estimates of χ_{MRI} from the SY model are systematically higher by ∼0.03 ppm. These values are consistent with susceptibility estimates obtained from QSM techniques (Bilgic et al., 2012; Langkammer et al., 2012; Yablonskiy et al., 2021).

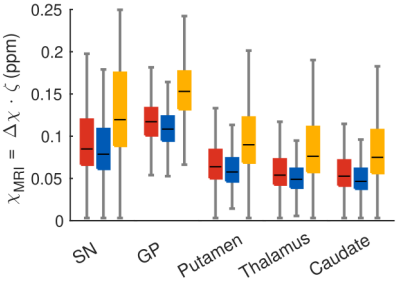

Fig. 2.8. MRI magnetic susceptibility ($\chi_{MRI} = \Delta\chi \cdot \zeta$) computed under the assumption of the SDR. The values of χ_{MRI} are consistent with estimates obtained using QSM techniques (Bilgic et al., 2012; Langkammer et al., 2012; Yablonskiy et al., 2021)

2.5 Discussion

Here we provide experimental evidence of non-exponential signal decay due to transverse relaxation in *in vivo* MRI data from subcortical regions. In agreement with theoretical studies, signal decay follows a gaussian behaviour at short echo times with a transition to exponential behaviour at long echo times. Models of the effect on the MRI signal of magnetic deposits within brain tissue show an improved fit to the data compared to the widely used exponential model. The strongest deviations from exponential behaviour were found in iron-rich areas, such as the GP and SN. From the estimates of the model parameters, we estimated the properties of the magnetic deposits at the source of the effect. The results are consistent with histological studies of iron distribution within brain tissue and suggest that non-exponential signal decay arises from spatially localized iron-rich cells.

2.5.1 Non-exponential transverse relaxation decay

The lack of evidence of non-exponential signal decay in subcortical regions has been attributed to the short timescale of the transition between the gaussian and exponential behaviours, below the range of achievable echo times (Yablonskiy et al., 2021). Here, we combined a dense sampling of the decay curve with acquisition strategies that reduce the noise level in the data (Castella et al., 2018; Raynaud et al., 2022) to collect reliable evidence of non-exponential signal decay. Transverse relaxation decay exhibits a gaussian behaviour at short echo times (T_E <5 ms) with a transition towards exponential decay (Fig. 2.1). This behaviour was predominantly observed in subcortical grey matter regions (Fig. 2.3) and is consistent with theoretical models of the effect on the MRI signal of magnetic deposits within brain tissue (Anderson and Weiss, 1953; Jensen and Chandra, 2000; Sukstanskii and Yablonskiy, 2003). These models show improved fit to the data compared with the widely used exponential model (Fig. 2.2). Amongst subcortical regions, the strongest non-exponential behaviours take place in the GP and SN.

The higher values of $R^*_{2,micro}$ and $\langle\Omega^2\rangle$ in the SN and GP (Fig. 2.4) are consistent with the higher concentration of iron in these regions (Hallgren and Sourander, 1958; Haacke et al., 2005; Langkammer et al., 2012; Krebs et al., 2014) and with the expected dependence of these parameters on iron concentration (Eqs. 2.5 and 2.6). However, other magnetic materials such as myelin or blood vessels might also contribute, particularly in the thalamus due to its comparatively high myelin and low iron concentrations (Hallgren and Sourander, 1958). We considered three models of the MRI signal generated by brain tissue with magnetic deposits. All the models fitted the data equally well, with marginal differences between them (Fig. 2.2). Nonetheless, the SY model yields higher estimates of $R^*_{2,micro}$ and $\langle\Omega^2\rangle$ compared to the AW and Padé models. This results from the long transition from the gaussian to exponential behaviours predicted by this model, due to the square-root term in Eq. 2.3. As a result, the exponential decay rate predicted by the SY model differs from the one observable experimentally (Fig. 2.5).

2.5.2 Characterization of magnetic deposits within subcortical tissue

From the estimates of the signal model parameters, we were able to estimate the properties of the magnetic deposits embedded within brain tissue. This would not have been achievable from the exponential end of the decay alone. This was conducted under the assumption of the SDR (Fig. 2.6) and DNR (Fig. 2.7) for which different analytical expressions exist.

The estimates of the magnetic susceptibility of the magnetic deposits, obtained under the assumption of the SDR, lie in the range $\Delta\chi \sim$1-3 ppm across subcortical regions and MRI signal models. The ordering of the $\Delta\chi$ estimates between subcortical values follows the ordering of *ex vivo* measures of iron concentration within brain tissue (Hallgren and Sourander, 1958; Haacke et al., 2005; Langkammer et al., 2012; Krebs et al., 2014). The estimates of $\Delta\chi$ are in good agreement with the magnetic susceptibility of iron-rich neuromelanin aggregates in the SN (Brammerloh et al., 2021). Under the assumption that ferritin is the only magnetic material within the tissue, these susceptibility estimates lead to estimates of iron concentration $[Fe] \sim$1-2 mg/g within the deposits, well in line with the intra-cellular concentrations of iron known from *ex vivo* studies (Friedrich et al., 2021). The estimates of the volume fraction of the deposits lie in the range $\zeta \sim$ 0.03-0.06 across subcortical regions and MRI signal models. The ordering of the ζ estimates between subcortical values also follows the ordering of *ex vivo* measures of iron concentration within brain tissue (Hallgren and Sourander, 1958; Haacke et al., 2005; Langkammer et al., 2012; Krebs et al., 2014). The estimates of ζ are in broad agreement with those calculated considering the distribution of iron at the cellular scale: $\zeta_{cell} = \frac{[Fe]_{bulk}}{[Fe]_{cell}} \sim$0.01, with $[Fe]_{bulk} \sim$0.02 mg/g (Hallgren and Sourander, 1958) and $[Fe]_{cell} \sim$1.5 mg/g (Friedrich et al., 2021). In addition, our ζ estimates are in line with the experimental volume fractions of neuromelanin observed in the SN (Brammerloh et al., 2021). Overall, these results indicate that the reported non-exponential signal decay arises from spatially localized clusters consistent with iron-loaded cells, rather than individual ferritin complexes.

The consistency of the estimates of the properties of the magnetic deposits with *ex vivo* studies highlights the plausibility of the SDR as the regime underlying transverse relaxation decay in subcortical grey matter. The estimates of MRI magnetic susceptibility, computed from the properties of the deposits under the assumption of the SDR ($\chi_{MRI} = \zeta\Delta\chi$, Fig. 2.8), are also consistent with those obtained from QSM techniques ($\sim$0.1 ppm, (Bilgic et al., 2012; Langkammer et al., 2012; Yablonskiy et al., 2021).

Under the assumption of the DNR, the values of the signal decay parameters were used to estimate the parameter τ, the decay time of the frequency auto-correlation of water molecules diffusing through the inhomogeneous magnetic field generated by the deposits. The τ estimates ($\sim$1.5 ms) suggest a typical radius of $\sim$3 μm for the magnetic deposits. In agreement with the SDR analysis, this finding suggests that cell-sized iron clusters are at the source of the non-exponential decay. This estimate of r is also consistent with the cell-based definition of the radius of magnetic deposits proposed by Taege et al. (2019) and with the value of r reported in studies of excised human grey matter tissue (Jensen and Chandra, 2000). In particular, the latter study also reported larger values of r in the putamen, thalamus, and caudate, compared to the GP as observed here (Fig. 2.7). Under the DNR, the parameters $\Delta\chi$ and ζ could not

be estimated. Instead, we estimated the parameter $\alpha = \tau\sqrt{\langle\Omega^2\rangle}$. The resulting estimates are smaller than 1, suggesting that the time scale τ at which molecules diffuse is smaller than the time scale of spin dephasing caused by magnetic material, consistently with the assumptions of the DNR theory. However, the parameter α was computed from estimates of the mean square frequency deviations averaged across a voxel $\langle\Omega^2\rangle$, rather than from the mean frequency generated by a single magnetic deposit $\delta\omega_s$ ($\langle\Omega^2\rangle \propto \zeta{\delta\omega_s}^2$). Estimation of α at the scale of the deposits may lead to higher values inconsistent with the assumptions of the DNR.

The SDR has been proposed as a valid explanation for iron-induced transverse relaxation in subcortical grey matter, due to the large differences between the relaxation rates in gradient-echo and spin-echo data (Sedlacik et al., 2014; Brammerloh et al., 2021). However, studies of the relationship between R_2^* and magnetic susceptibility suggest that the contribution of iron to relaxation in the basal ganglia can be described under the DNR, provided that iron is aggregated in clusters with $\sim$100 nm radius (Shin et al., 2021; Yablonskiy et al., 2021). The most plausible scenario is that transverse relaxation is the result of a combination of both regimes. Therefore, models that describe the relaxation process without relying on these assumptions may allow a more accurate characterization of the magnetic deposits at the source of non-exponential transverse relaxation in subcortical brain regions (Jensen and Chandra, 1999; Bauer and Nadler, 2002; Ziener et al., 2005).

2.6 Conclusions

In this study, we provided experimental evidence of non-exponential transverse relaxation from *in vivo* gradient-echo MRI data in subcortical brain regions at 3T. The behaviour of the decay is consistent with the effect of magnetic deposits on the MRI signal predicted by theoretical studies. These theoretical models of the MRI signal yield improved fit with experimental data compared to the widely used exponential model. The larger deviations from exponential decay were observed in iron-rich subcortical regions (substantia nigra, globus pallidus). From the estimates of the signal decay parameters, we characterized the distribution of the magnetic deposits within brain tissue at the source of the non-exponential decay. Our estimates are consistent with *ex vivo* studies of iron distribution within brain tissue and suggest that the observed non-exponential signal decay arises from spatially localized iron-rich cells.

Non-exponential decay of the MRI signal due to transverse relaxation allows the characterization of iron-rich deposits within subcortical structures from *in vivo* MRI data and opens new avenues for the study of iron-related brain changes in neurodegenerative diseases.

Chapter 3

Summary of the Results

The research carried out during my PhD involved two main projects and has resulted in two published peer-reviewed papers and an additional draft manuscript.

As part of the first project, the two published papers focused on the characterization of the morphological features of neuronal axons (see Appendix). As part of the second project, the third manuscript focused on the characterization of magnetic deposits, in particular iron, within the brain tissue (Chapter 2).

Here, the main results from the two published articles (section 3.1.1 and 3.1.2) and the third draft manuscript (section 3.2) are presented as well as a description of my individual contributions to each of the three scientific communications.

3.1 Characterization of axonal morphology in white matter tracts

To characterize the morphological features of axons composing white matter, we developed a novel biophysical model for the simultaneous estimation of the axonal radius and relative myelin thickness using EEG and MRI data (Fig. 3.1).

The MRI data consisted of the MRI g-ratio (section 1.4), a measure of myelin thickness, sampled along a white matter fibre tract (Fig. 3.1, left panel). The MRI g-ratio maps (Stikov et al., 2015) were computed using the NODDI model (Zhang et al., 2012) and MTsat maps (Helms et al., 2008a,b). EEG is used to estimate axonal conduction velocity along the visual transcallosal white matter tract (Fig. 3.1, left panel). For this purpose, we applied the well-established Poffenberger's paradigm to estimate the visual IHTT (section 1.5). The basis for IHTT estimation using this paradigm is that lateralized visual stimuli induce an activity increase in the contralateral hemisphere prior to the ipsilateral hemisphere. Therefore, IHTT can be estimated as the latency difference between the maximal neuronal activity (obtained using EEG source reconstruction techniques) at two homologous visual cortical regions. Finally, conduction velocities can be estimated by dividing the tract length by the IHTT.

From the acquired data we estimate the axonal radius distribution – $P(r)$ – and the axonal g-ratio – $g(r)$ (Fig. 3.1, right panel). $P(r)$ is defined as a gamma distribution with mode M

and scale θ. M represents the mode/peak of the axonal radius distribution. By construction, an increased value of θ indicates a broader spread of $P(r)$ into large radius values. $g(r)$ is given by a power-law with parameters α, representing the slope of the radius dependence of the axonal g-ratio, and β is a scaling factor. In this work, from this set of 4 model parameters, parameters α and M were fixed and θ and β were estimated with the model.

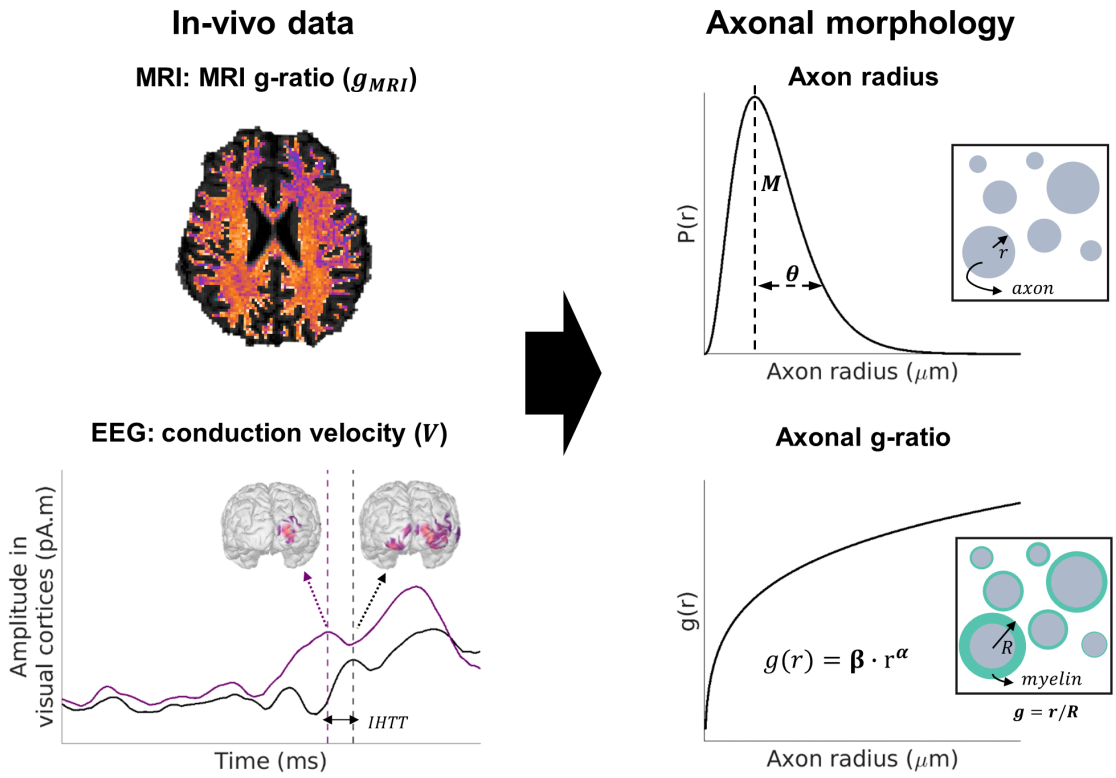

Fig. 3.1. Proposed approach for estimating morphological features of axons *in vivo*. The *in vivo* data (left panel) consists of i) the MRI g-ratio (a measure of relative myelin thickness), sampled along a white matter fibre tract; ii) the conduction velocity of the axons in the same tract, estimated using EEG-based measures of IHTT. From the acquired data we estimate the axonal radius distribution $P(r)$ and the axonal g-ratio $g(r)$ (right panel). $P(r)$ is defined as a gamma distribution with mode M and scale θ. $g(r)$ is given by a power-law with parameters α and β.

In the first stage of this project, the estimation of the IHTT was obtained from EEG data averaged across a group of 14 subjects. From the group-averaged IHTT and the individual-measured MRI g-ratio, we used the proposed model to estimate the morphological features of the axons for each participant. The estimates of axonal radius distribution and fibre myelination are consistent with previous literature values obtained from *ex vivo* histological studies of brain tissue. These results are presented in the first article (section 3.1.1).

Attempting to refine our proposed approach, in the second stage of this project, rather than using a group-average IHTT measure, we proposed a framework for obtaining subject-specific estimates of IHTT from EEG data. We successfully demonstrated the feasibility of this approach in a cohort of 14 volunteers, with the morphological estimates agreeing with literature values. The corresponding results can be found in the second article (section 3.1.2).

3.1.1 *In vivo* Estimation of Axonal Morphology From Magnetic Resonance Imaging and Electroencephalography Data

The first scientific article published on this work is entitled "*In vivo* Estimation of Axonal Morphology From Magnetic Resonance Imaging and Electroencephalography Data". It was published in Frontiers in Neuroscience in the issue of April 2022, with authors Rita Oliveira, Andria Pelentritou, Giulia Di Domenicantonio, Marzia De Lucia, and Antoine Lutti, all from the Laboratory for Research in Neuroimaging, Department of Clinical Neuroscience, Lausanne University Hospital and University of Lausanne, Lausanne, Switzerland.

As the first author, I actively participated in the development of the model and wrote the necessary code for its implementation. In addition, I led and conducted the MRI/EEG experiment, and was responsible for data analysis. Finally, I wrote the manuscript describing this work and was responsible for any revision and editing requirements.

The abstract of this article (Oliveira et al., 2022) is given below:

> Purpose: We present a novel approach that allows the estimation of morphological features of axonal fibers from data acquired *in vivo* in humans. This approach allows the assessment of white matter microscopic properties non-invasively with improved specificity.
>
> Theory: The proposed approach is based on a biophysical model of Magnetic Resonance Imaging (MRI) data and of axonal conduction velocity estimates obtained with Electroencephalography (EEG). In a white matter tract of interest, these data depend on 1) the distribution of axonal radius – $P(r)$ – and 2) the g-ratio of the individual axons that compose this tract - $g(r)$. $P(r)$ is assumed to follow a Gamma distribution with mode and scale parameters, M and θ, and $g(r)$ is described by a power law with parameters α and β.
>
> Theory: The proposed approach is based on a biophysical model of Magnetic Resonance Imaging (MRI) data and of axonal conduction velocity estimates obtained with Electroencephalography (EEG). In a white matter tract of interest, these data depend on 1) the distribution of axonal radius – $P(r)$ - and 2) the g-ratio of the individual axons that compose this tract - $g(r)$. $P(r)$ is assumed to follow a Gamma distribution with mode and scale parameters, M and θ, and $g(r)$ is described by a power law with parameters α and β.
>
> Methods: MRI and EEG data were recorded from 14 healthy volunteers. MRI data were collected with a 3T scanner. MRI-measured g-ratio maps were computed and sampled along the visual transcallosal tract. EEG data were recorded using a 128-lead system with a visual Poffenberg paradigm. The interhemispheric transfer time and axonal conduction velocity were computed from the EEG current density at the group level. Using the MRI and EEG measures and the proposed model, we estimated morphological properties of axons in the visual transcallosal tract.
>
> Results: The estimated interhemispheric transfer time was 11.72$\pm$2.87 ms, leading to an average conduction velocity across subjects of 13.22$\pm$1.18 m/s. Out of the 4 free parameters of the proposed model, we estimated θ - the width of the right tail of the axonal radius distribution and β - the scaling factor of the axonal g-ratio, a measure of fiber myelination. Across subjects, the parameter θ was 0.40$\pm$0.07 μm and the parameter β was 0.67$\pm$0.02 $\mu m^{-\alpha}$.
>
> Conclusions: The estimates of axonal radius and myelination are consistent with histological findings, illustrating the feasibility of this approach. The proposed method allows the

measurement of the distribution of axonal radius and myelination within a white matter tract, opening new avenues for the combined study of brain structure and function, and for *in vivo* histological studies of the human brain.

As part of this publication and to foster open science principles, data analysis custom scripts and the processed data associated with this work are publicly available, at:

- `https://github.com/rita-o/AxonalMorphology`
- `https://doi.org/10.5281/zenodo.6027335`

3.1.2 Single-subject electroencephalography measurement of interhemispheric transfer-time for the *in vivo* estimation of axonal morphology

The second scientific article entitled "Single-subject electroencephalography measurement of interhemispheric transfer-time for the *in vivo* estimation of axonal morphology" was published in Human Brain Mapping in July 2023 by Rita Oliveira, Marzia De Lucia, and Antoine Lutti, the two last authors contributed equally to this work. All authors are from the Laboratory for Research in Neuroimaging, Department of Clinical Neuroscience, Lausanne University Hospital and University of Lausanne, Lausanne, Switzerland.

As the first author, I was responsible for the acquisition of a second EEG in a subset of the participants from the first study. I devised and conducted the analyses described in the paper. In addition, I wrote the first draft of the manuscript and revised it during the editing and revision processes.

The abstract of this scientific article (Oliveira et al., 2023) is given below:

> Assessing axonal morphology *in vivo* opens new avenues for the combined study of brain structure and function. A novel approach has recently been introduced to estimate the morphology of axonal fibres from the combination of MRI data and EEG measures of the interhemispheric transfer time (IHTT). In the original study, the IHTT measures were computed from EEG data averaged across a group, leading to bias of the axonal morphology estimates.
>
> Here, we seek to estimate axonal morphology from individual measures of IHTT, obtained from EEG data acquired with a visual evoked potential experiment. Subject-specific IHTTs are computed in a data-driven framework with minimal *a priori* constraints, based on the maximal peak of neural responses to visual stimuli within periods of statistically significant evoked activity in the inverse solution space.
>
> The subject-specific IHTT estimates ranged from 8 to 29 ms except for one participant and the between-session variability was comparable to between-subject variability. The mean radius of the axonal radius distribution, computed from the IHTT estimates and the MRI data, ranged from 0 to 1.09 μm across subjects. The change in axonal g-ratio with axonal radius ranged from 0.62 to 0.81 $\mu m^{-\alpha}$.
>
> The single-subject measurement of the IHTT yields estimates of axonal morphology that are consistent with histological values. However, improvement of the repeatability of the IHTT estimates is required to improve the specificity of the single-subject axonal morphology estimates.

Custom code and processed data that enable the replication of these results can be found at:

- `https://github.com/rita-o/SingleSubjectIHTTEstimation`
- `https://doi.org/10.5281/zenodo.7446009`

3.2 Characterization of magnetic deposits in subcortical tissue

The second project of this PhD aimed at characterizing the distribution of iron deposits within subcortical tissue. To achieve this goal, we examined the decay of the MRI signal caused by transverse relaxation. This signal decay is commonly taken to follow an exponential decay with a rate R_2^* (Weiskopf et al., 2014). However, when magnetic material (e.g. iron-loaded cells, myelin, or blood vessels) is present within the tissue, the signal decay due to transverse relaxation deviates from an exponential function (Haacke et al., 2005; Kiselev and Novikov, 2018). According to theoretical studies, it instead follows a Gaussian behaviour at short echo times (dependent on parameter $\langle\Omega^2\rangle$) and an exponential decay at long echo times (with rate R_2^*) (Yablonskiy and Haacke, 1994; Jensen and Chandra, 2000; Kiselev and Novikov, 2002, 2018; Sukstanskii and Yablonskiy, 2003).

With this theoretical approach in mind, we fitted the signal decay in subcortical grey matter with existing theoretical models of the effect of magnetic deposits within brain tissue on the MRI signal. From the model parameter estimates of the Gaussian ($\langle\Omega^2\rangle$) and exponential (R_2^*) parts of the signal decay (Fig. 3.2, left panel), we estimated properties of the magnetic deposits at the source of the non-exponential decay. Under the assumption of the SDR, one of the limiting regimes that can be used to explain transverse relaxation in environments containing magnetic material (Chapter 2), these properties are the volume fraction occupied by the magnetic deposits (ζ) and the magnetic susceptibility (χ) of such deposits (Fig. 3.2, right panel). The latter is directly proportional to the concentration of magnetic material within the deposits. Under the assumption of the other limiting regime, DNR, the volume fraction ζ and the magnetic susceptibility χ of the deposits cannot be independently estimated. Instead, the radius r of the magnetic deposits can be deduced under this regime.

As part of this work, we provided, for the first time, experimental evidence of non-exponential transverse relaxation in subcortical grey matter. Models of the effect of magnetic deposits on the MRI signal showed an improved fit to the data compared to the commonly assumed exponential model. The strongest deviations from exponential behaviour, indicative of the presence of a large amount of magnetic material, were observed in the GP and SN. These results are consistent with the high iron concentrations observed histologically in these regions (Hallgren and Sourander, 1958). Under the assumption of the SDR, the estimated volume fraction and magnetic susceptibility within the magnetic deposits were consistent with *ex vivo* studies and point to the fact that the measured magnetic deposits were mainly iron-rich cells. Under the assumption of the DNR, the estimated radius r of the deposits was also consistent with a typical cell size and in agreement with the SDR results.

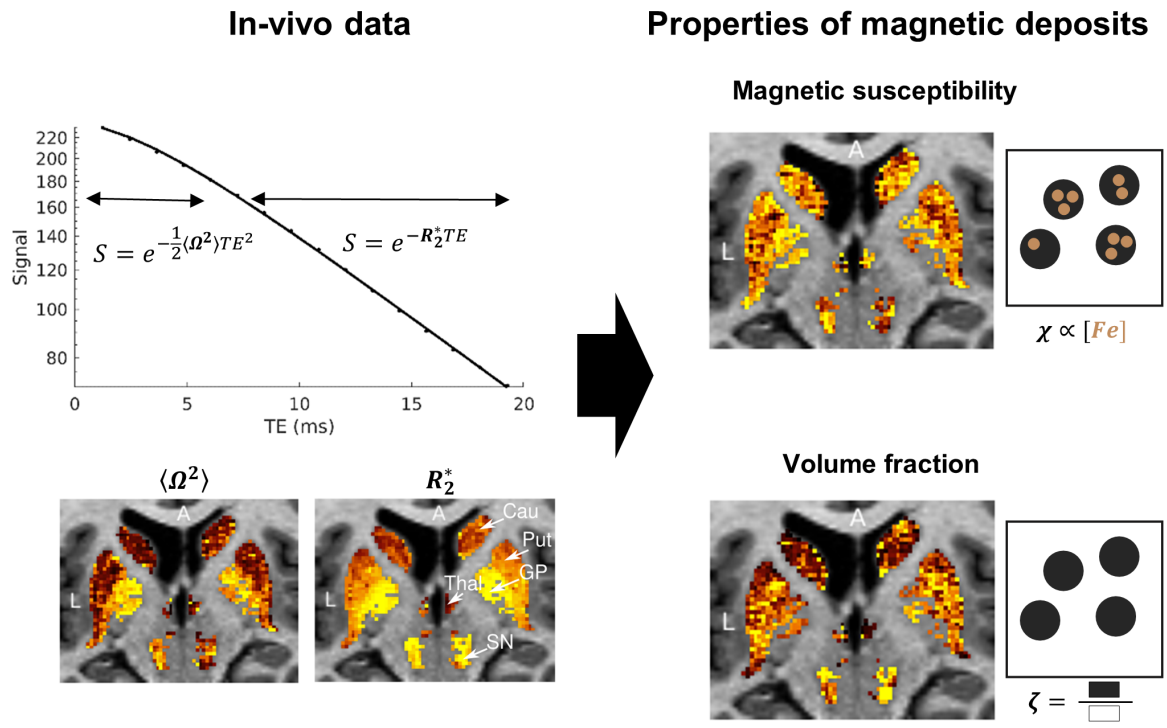

Fig. 3.2. Proposed approach for the characterization of magnetic deposits within subcortical tissue. The MRI signal decay due to transverse relaxation in tissues containing magnetic material follows a non-exponential behaviour. We fitted the signal decay with theoretical models of the effect of magnetic deposits within brain tissue on the MRI signal (left panel). From the model parameter estimates of the Gaussian ($\langle\Omega^2\rangle$) and exponential (R_2^*) parts of the signal decay, we calculated the magnetic susceptibility of magnetic deposits (χ) and the fraction of the voxel occupied by such deposits (ζ) (right panel). χ is proportional to the concentration of magnetic material within the deposits. In subcortical grey matter, the region analyzed in this thesis, the magnetic deposits can be assumed to be formed primarily by iron (Hallgren and Sourander, 1958), and therefore, χ is proportional to the concentration of iron within the deposits. L - left, A - anterior, SN - substantia nigra, Cau - caudade, Put - putamen, GP - globus pallidus, Thal - thalamus.

The third manuscript entitled: "Non-exponential transverse relaxation in subcortical brain regions" is the collective effort of Rita Oliveira[1], Quentin Raynaud[1], Valerij Kiselev[2], Ileana Jelescu[3] and Antoine Lutti[1] from [1]Laboratory for Research in Neuroimaging, Department of Clinical Neuroscience, Lausanne University Hospital and University of Lausanne, Lausanne, Switzerland; [2]Medical Physics, Department of Radiology, Faculty of Medicine, University of Freiburg, Freiburg, Germany; [3]Department of Radiology, Lausanne University Hospital (CHUV) and University of Lausanne, Lausanne, Switzerland.

For the third scientific article, I joined an ongoing project, as part of which the data was already acquired and the majority of the code for the analysis was written. I was involved in a refinement of the methodology and the analysis code. In addition, I analyzed the data and drafted the manuscript for this work. Code and Data will become publicly available upon publication to allow for the replication of the findings.

Chapter 4

Discussion

This PhD work aimed at the characterization of brain tissue microstructure from *in vivo* data and was conducted in two distinct projects.

First, we focused on the characterization of the morphological features of neuronal axons in the visual transcallosal white matter tract (Fig. 1.1A). For this purpose, we developed a novel biophysical model for the simultaneous estimation of axonal radius and relative myelin thickness. This was achieved by the combination of MRI-based g-ratio measurements and EEG-based measures of axonal conduction velocity computed from estimates of the IHTT. In our first study, IHTT was estimated from EEG data averaged across a group of subjects. In our second study, we refined our approach by estimating IHTT at the single-subject level for a subject-specific estimation of axonal morphological features.

Second, we characterized the deposits of magnetic material within subcortical tissue (Fig. 1.1B). To this end, we applied existing biophysical models of the effect of magnetic deposits on the MRI signal due to transverse relaxation. This allowed for the computation of measures such as the volume fraction and magnetic susceptibility of the magnetic deposits, which, in subcortical regions, consist predominantly of iron.

The key contributions and the potential clinical translation of the proposed approaches in the first (section 4.1) and second (section 4.2) project are discussed in this chapter. In addition, the limitations and future applications are also addressed.

4.1 Characterization of axonal morphology in white matter tracts

4.1.1 Estimation of conduction velocity *in vivo*

The estimation of axonal morphological features involved the acquisition of MRI-based g-ratio maps and EEG-based measures of axonal conduction velocity via the estimation of the IHTT (Fig. 3.1). While the computation of the MRI g-ratio is relatively straightforward, the latter involved the proposal of a novel approach for subject-specific EEG-based estimation of the IHTT. Hence, prior to addressing the general contributions of our axonal morphology model, in this section, the advantages and limitations of this approach for IHTT estimation are discussed.

In estimating the IHTT, our proposed methodology was free from the *ad hoc* selection of electrodes and of the evoked response component, as we estimate the neural origins of the measured activity from EEG scalp electrodes with minimal *a priori* constraints using source reconstruction techniques. Conduction delays were estimated based on the difference in latency of the maximal peak of neural response to visual stimuli between two homologous cortical regions. Moreover, an additional advantage of our approach compared to previous reports is that it allows for the estimation of subject-specific IHTT.

Across the 14 subjects analyzed, the estimated subject-specific visual IHTT ranged from 8 to 29 ms; one participant exhibited an implausible negative IHTT. The obtained IHTT values were consistent with the limited studies estimating subject-specific IHTT from evoked activity at electrode-level (Chaumillon et al., 2018; Friedrich et al., 2017; Westerhausen et al., 2006). Our IHTT estimates are also consistent with the delays estimated using intracranial recordings from whole-brain cortical–cortical connections (Lemarechal et al., 2022). Importantly, our results suggest a subject-specific neuronal response to visual stimuli and therefore, indicate that the main challenge in IHTT estimation lies in the definition of a robust metric to extract the IHTT from the EEG data across subjects in a consistent manner while minimizing assumptions. In our case, these assumptions included the search time window and the definition of maximal activity within the visually evoked responses of interest.

The challenge of IHTT estimation at the single-subject level has been observed in numerous studies. In particular, inconsistent IHTT values across participants, and, similar to our results, even negative IHTTs have been reported (e.g. Saron and Davidson, 1989; Marzi et al., 1991; Westerhausen et al., 2006; Friederici et al., 2007). The inconsistent findings across participants in our study may be explained by differences in brain morphology (Saron and Foxe, 2003) and inaccuracies in the source estimation algorithms. The localization of the neuronal generators of scalp-measured EEG activity in deep cortical fissures and the unique characteristics of each individual's cortical anatomy can make source reconstruction in the visual cortex challenging (Creel, 2012). This is of particular relevance when single-subject analysis is considered as was the case in our second study, due to the lower signal-to-noise ratio. In this context, exploring the impact of different source reconstruction techniques on IHTT estimation can in turn improve the calculation of conduction velocity using EEG measures (Plomp et al., 2010; Mahjoory et al., 2017). An alternative solution for the estimation of conduction velocities *in vivo* is through different neuroimaging techniques, such as Transcranial Magnetic Stimulation (Lo and Fook-

Chong, 2004; Spitzer et al., 2004; Basso et al., 2006; Deftereos et al., 2008; Marzi et al., 2009).

Beyond improved neuroimaging methodologies, more advanced models such as the ones proposed in Sorrentino et al. (2021) and Deslauriers-Gauthier and Deriche (2019) could also be considered for the estimation of conduction velocities *in vivo* (section 1.5). However, contrary to our proposed approach, these models require a high number of parameters and *a priori* assumptions.

4.1.2 Key contributions

A major asset of our proposed model is that it enables the simultaneous estimation of two morphological properties of the neuronal axons (the axon radius and the fibre relative myelin thickness). This allows for a more comprehensive assessment of the microstructural properties of white matter tracts.

To demonstrate the viability of our proposed axonal morphology model, we estimated the axonal radius distribution $P(r)$ and the axonal g-ratio dependence on the radius $g(r)$ in the visual transcallosal white matter tract for a cohort of 14 volunteers (Fig. 3.1), from single-subject IHTT and MRI-ratio data. The estimated mean axon radius ranged from 0 to 1.09 μm across subjects. The mean value across subjects was 0.53 μm, in line with previous estimates from histological studies, reporting $\sim$0.62 μm in the visual cortex of human tissue (Caminiti et al., 2009). Moreover, in our study, axons above 2.50 μm represented $<$0.04% of the total fibre count. This result was also consistent with the histology literature, wherein maximum axonal radius was commonly reported to be between $\sim$1.50–3.00 μm in human brain tissue (Aboitiz et al., 1992; Caminiti et al., 2009; Liewald et al., 2014). The reduced overestimation of the axon radius compared to histology stems from the explicit relationship between the MRI/EEG data and the underlying histological properties of brain tissue ($P(r)$ and $g(r)$). This is an advantage of our technique compared to diffusion-based methods that rely only on fitting the radius to the measured signal, which can even be heavily influenced by the extra-axonal geometry, and thus fail to accurately reflect the true axonal radius ((Burcaw et al., 2015; Lee et al., 2018), section 1.3.3).

Although only the mean of the axon radius distribution is reported above, it is important to highlight that our proposed model is specifically tailored to the estimation of the whole distribution of axonal radii rather than a single summary index, which is not achieved by many other approaches ((e.g. Alexander et al., 2010), section 1.3.2).

The other axonal feature estimated with our approach (Fig. 3.1) is the axonal g-ratio, a measure of relative myelin thickness. Specifically, with our model we estimate the axonal g-ratio parameter β, a scaling factor that equally contributes to axons of all sizes. A large β implies an overall larger amount of myelin wrapped around the axons. In our results, β ranged from 0.62 to 0.81 $\mu m^{-\alpha}$. Despite this parameter not being directly comparable to other *in vivo* literature, our estimated $g(r)$ was consistent with histological measures of the axonal g-ratio in the splenium of the corpus callosum (Jung et al., 2018). The successful estimation of $g(r)$ in our study offers an important contribution to the field as this measure remains largely unresolved in the literature and has not yet been integrated into any specific tissue model, unlike here.

Beyond the estimated measures, our proposed axon morphology model offers several technical advantages compared to other existing methods (section 1.3.2). First, it requires a low MRI scan time ($<$1 hour), making it more time-efficient compared to some of the other state-of-the-art models (e.g. Benjamini et al., 2014; Alexander et al., 2010). Second, unlike other models (e.g. Assaf et al., 2008; Fan et al., 2020), our approach eliminates the need for high gradient strength, making it compatible with clinical MRI recordings.

4.1.3 Limitations

Despite the valuable insights obtained from our work, it is essential to acknowledge some limitations that may impact the future use of our axonal morphological estimates as brain biomarkers.

First, our approach for the estimation of axonal morphological features requires the acquisition of a structural measure of white matter (MRI-based g-ratio) and a measure of brain function (EEG-based axonal conduction velocity). While the MRI acquisition is simple and could be easily applied in clinics, the EEG acquisition involves a more complex experimental procedure with fairly long acquisition times ($\sim$ 2.5 hours), making it difficult to use in a clinical setting.

Second, the validity of the model assumptions in the context of pathological conditions is yet to be determined. In particular, the peak of the axonal radius distribution M was fixed across white matter tracts and individuals, as suggested by previous studies (Tomasi et al., 2012; Liewald et al., 2014). However, this assumption may not hold true in neurological disorders where axons are impacted differently depending on their size (section 1.3.1).

Third, the proposed approach has not been applied to the entire brain; being limited to the visual transcallosal tract, where conduction velocity estimation was possible. Moreover, the estimation of this conduction velocity relied on the IHTT. Although the estimated IHTT aligns with existing literature, the underlying mechanisms and anatomical pathways involved in the neuronal transfer of information using the Poffenberger paradigm are still not clear, and further investigation is needed.

Fourth, our method does not explicitly model orientation dispersions or crossing fibres, contrary to other state-of-the-art methods (e.g. Zhang et al., 2011b,a). Instead, our estimation of axon morphology is performed at the single tract level, which implies that all voxels of the tract under consideration are used when calculating g_{MRI} values, including voxels with crossing fibres or orientation dispersions.

Finally, despite an agreement with the histological literature, our axonal morphological estimates showed a high level of variability mainly attributed to the estimation of the IHTT at the single-subject level. Increasing the reproducibility of the IHTT estimates is necessary to improve the specificity of the axonal estimates at the individual level and their subsequent use as brain biomarkers.

4.1.4 Future applications

In this work, we focused on the morphological assessment of axons only within the visual transcallosal tract, as axonal conduction velocities are challenging to estimate in all white matter

tracts. An alternative approach that overcomes the need for conduction velocity, allowing for the morphological characterization of white matter tracts throughout the entire brain, is to, instead of estimating both $P(r)$ and $g(r)$ from MRI and EEG data, compute only $P(r)$ from the MRI data (Fig. 3.1). To accomplish this, one could assume that the axonal g-ratio dependence on the radius ($g(r)$) is the same all over the brain. This assumption implies that axons of equivalent calibres in different tracts would be composed of equal amounts of myelin. To find $g(r)$ *in vivo*, one could use the visual transcallosal tract as a calibration step, wherein its scaling factor β is estimated using both MRI and EEG data (as performed in this thesis). Once β is determined, its value can be fixed and $P(r)$ can then be estimated in other white matter tracts from the MRI data alone. Despite promising preliminary results (Fig. 4.1), validation of the assumption of a constant β across tracts is essential for future analysis.

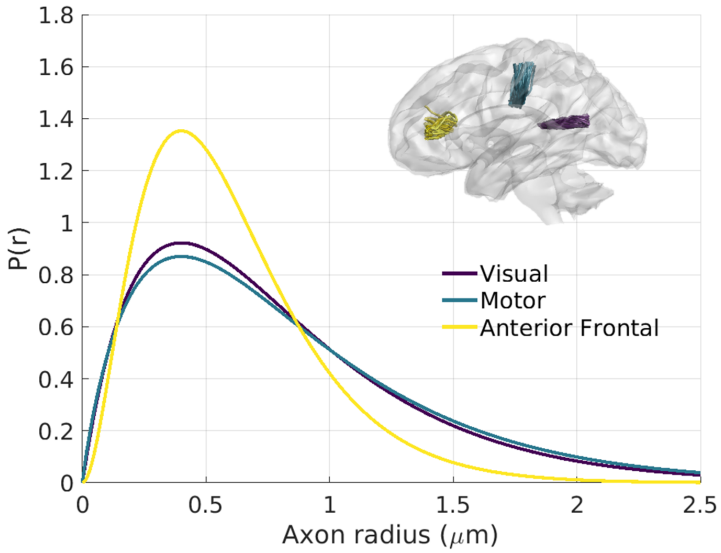

Fig. 4.1. Future applications of the proposed axonal morphology model. Axonal radius distribution can be estimated for different white matter tracts by assuming a constant axonal g-ratio dependence on the radius $g(r)$ across tracts. $g(r)$ was estimated *in vivo* in the visual transcallosal tract from conduction velocity estimates obtained using group-averaged EEG data. $P(r)$ was then estimated for the motor and anterior frontal transcallosal tracts from MRI data alone, by assuming the same $g(r)$ as in the visual tract. Visual (0.40 μm) and motor (0.44 μm) transcallosal tracts have a larger θ compared to the frontal tract (0.20 μm); a larger θ indicates a broader spread of the distribution into larger radii. (Unpublished results presented in a conference abstract at OHBM 2022).

Although the previous proposal bypasses the need for conduction velocities to be acquired *in vivo*, the ideal case would be to actually have conduction velocities estimated *in vivo* for several white matter tracts. Having structural ($P(r)$ and $g(r)$) and functional (velocity) measures acquired in the same white matter tract would allow for the investigation of the relationship between structure and function across cortical brain regions. Moreover, the *in vivo* estimation of both axonal radius distribution ($P(r)$) and axonal g-ratio dependence on the radius ($g(r)$) in several white matter tracts would offer novel insights into the structural organization of the different brain regions. For example, it could validate or refute the assumption of constant axonal g-ratio dependence on the radius across tracts mentioned in the previous paragraph.

4.2 Characterization of magnetic deposits in subcortical tissue

4.2.1 Key contributions

To accomplish the characterization of iron deposits within subcortical brain tissue, it was necessary to identify first the non-exponential behaviour of the transverse relaxation signal decay caused by the iron deposits (Fig. 3.2). In this work, that was made possible through the dense sampling of the transverse decay and the implementation of acquisition strategies that reduce the noise level in the data. With this experimental set-up, we were able to provide *in vivo* evidence in humans for non-exponential MRI signal decay due to transverse relaxation in brain regions containing magnetic content, such as subcortical grey matter. To the best of our knowledge, this is the first account of the detection of non-exponential signal decay in subcortical brain tissue *in vivo*.

The non-exponential decay was observed across the 5 subjects analyzed and consisted of a gaussian-like behaviour at short echo times ($<$ 5-10 ms) followed by a transition toward exponential decay at longer echo times ($>$ 5-10 ms), in agreement with theoretical models that account for the effect of magnetic deposits on the MRI signal decay (Jensen and Chandra, 2000; Sukstanskii and Yablonskiy, 2003; Anderson and Weiss, 1953). Beyond this agreement, the use of these theoretical models offered an improved fit to *in vivo* MRI data compared to the commonly assumed exponential model. Furthermore, the strongest deviations from exponential behaviour were observed in the GP and SN, which is consistent with the known higher concentration of iron within these regions (Hallgren and Sourander, 1958).

The detection of the non-exponential behaviour of the signal decay allows the subsequent calculation of properties specific to the magnetic deposits at the source of that behaviour, including the volume fraction ζ and magnetic susceptibility χ of the deposits under the assumption of the SDR and the radius of the deposits r under the DNR (see Chapter 2 for SDR and DNR definitions).

Under the assumption of SDR, iron-rich regions such as the GP and SN showed the largest value of ζ ($\sim$0.04 to 0.06), compared to the putamen, caudate and thalamus ($\sim$0.03 to 0.04). Our ζ estimates were in the same order of magnitude as the experimental volume fractions of neuromelanin obtained in the SN (Brammerloh et al., 2021). The magnetic susceptibility χ was also shown to be larger in the SN and GP ($\chi \sim$ 2 ppm) compared to the remaining regions ($\chi \sim$ 1.4 ppm). Our χ estimates fall in the same range as the intracellular susceptibilities of neuromelanin estimated in the SN (Brammerloh et al., 2021). From the χ estimates one can calculate the concentration of iron within the iron deposits. Although several iron-carrying complexes, such as hemosiderin, neuromelanin, and transferrin, are also present in the brain (Möller et al., 2019), here, for the sake of simplicity, we consider ferritin as the exclusive source of magnetic material within iron deposits. This leads to iron concentrations of $\sim$1.6, 1.8, 1.3, 1.1, and 1.1 mg/g in the SN, GP, putamen, thalamus, and caudate, respectively, in line with intra-cellular iron concentrations reported in the literature (Friedrich et al., 2021). Under the assumption of the DNR, the typical radius r of the magnetic deposits is $\sim$ 3 μm, in the order of a typical cell size and in agreement with the SDR analysis.

In summary, our results are consistent with *ex vivo* studies and suggest that non-exponential signal decay arises from spatially localized magnetic deposits consistent with iron-loaded cells. We were able to estimate the magnetic susceptibility within these iron deposits as well as their volume fraction. Our provided measures offer a higher degree of specificity to iron deposits compared to many current approaches that primarily rely on voxel-averaged measures to characterize iron content (section 1.6).

Of additional importance, the proposed approach also has technical advantages. It requires short MRI acquisition times ($<$20 minutes) and it uses a clinical 3T MRI scanner, making it easily adaptable to clinical settings.

4.2.2 Limitations and applications

Despite the noteworthy advantages of our model, there are several limitations to consider. First, this approach requires a minimized level of noise in the data in order to capture small non-exponential effects. To achieve this, during MRI acquisition we mitigate image degradation due to patient motion (Zaitsev et al., 2006; Maclaren et al., 2012) and cardiac-induced noise (Raynaud et al., 2022). These corrections involve the use of a motion correction camera and the acquisition of pulse oximetry data, which introduces further technical challenges and potentially limits the widespread implementation of this approach, in research and in clinics.

A second limitation to note is that our approach does not allow for a distinction to be made between iron and myelin content. Indeed, the microstructural estimates obtained herein can be the consequence of any magnetic material, such as iron, myelin or blood vessels. Nonetheless, it is reasonable to hypothesize that within subcortical grey matter, the region of interest of this study, the primary source of magnetic material is iron-rich cells (Hallgren and Sourander, 1958).

Another important limitation of this approach is that the volume fraction ζ and magnetic susceptibility of the magnetic material χ can only be estimated independently if the SDR is assumed (Chapter 2). Thus, care must be taken before the application of this approach in other brain regions, where the SDR assumption may not hold. Under the assumption of the other limiting regime, DNR, the fitted parameters ($< \Omega^2 >$ and R_2^*) depend on 3 tissue features of iron deposits: volume fraction ζ, magnetic susceptibility χ and diffusion time τ (or radius r). Therefore, unlike under the assumption of SDR, ζ and χ cannot be disentangled from the two fitted parameters only. This limitation could be addressed by incorporating QSM maps into this model as magnetic susceptibilities measured with QSM (χ_{MRI}) depend on our parameters ζ and χ ($\chi_{MRI} = \zeta\chi$, see Chapter 2). This extra data point would therefore enable the independent estimation of magnetic susceptibility and volume fraction under the assumption of DNR. This model enhancement would also enable an improved assessment of the validity of the two limiting regimes (SDR and DNR) in subcortical grey matter. This assessment would be achieved by comparing the plausibility of the ζ and χ estimates obtained under each regime with *ex vivo* literature.

Rather than using models that assume one of the limiting regimes (SDR or DNR) to describe the transverse relaxation as we did here, one could use models that describe the relaxation process for all diffusion regimes, thereby not relying on the assumptions made under the SDR

or the DNR (e.g. Jensen and Chandra, 1999; Bauer and Nadler, 2002; Ziener et al., 2005). Ultimately, such models may allow for more accurate characterization of the magnetic deposits at the source of non-exponential transverse relaxation in subcortical brain regions.

Finally, this approach is of particular relevance in the context of clinical research. One noteworthy example is its potential application in the study of neurodegenerative disorders such as Parkinson's disease, where pathological iron accumulation is at play (Thompson et al., 2001; Zecca et al., 2004; Hare et al., 2013). The measurement of magnetic susceptibility within iron deposits and their volume fraction, as offered by our approach, can improve our understanding of the iron-related mechanisms underlying this disease. For instance, one can address whether iron accumulation in Parkinson's is a consequence of increased iron content within cells or a higher number of iron-rich cells. Similarly, if these iron-related mechanisms differ across Parkinson's disease subtypes, these measures could facilitate the more precise classification of individuals with Parkinson's disease.

4.3 Final remarks

Bridging the gap between the low resolution of non-invasive imaging techniques, such as MRI, and the high resolution obtained using *post mortem* microscopy methods constitutes an ongoing challenge in neuroscience. This challenging yet intriguing task known as *in vivo* histology was the central focus of this thesis. Our successful contributions to this field involved the non-invasive estimation of axonal morphological features and iron content in healthy participants, consistent with *ex vivo* histological studies. This consistency underscores the robustness of our approaches, highlighting their potential as valuable tools for probing microstructural changes in neural tissue. Our estimated features may be particularly useful for the *in vivo* assessment of axonal damage, demyelination and remyelination, and abnormal iron accumulation. To conclude, our estimates of microstructure represent promising candidates for novel clinical biomarkers that can offer novel insights into healthy development and ageing as well as into pathophysiology in numerous clinical conditions.

Bibliography

Aboitiz, F., Scheibel, A. B., Fisher, R. S., and Zaidel, E. (1992). Fiber composition of the human corpus callosum. *Brain Research*, 598:143–153.

Alexander, D. C., Dyrby, T. B., Nilsson, M., and Zhang, H. (2019). Imaging brain microstructure with diffusion MRI: practicality and applications. *NMR in Biomedicine*, 32(4):1–26.

Alexander, D. C., Hubbard, P. L., Hall, M. G., Moore, E. A., Ptito, M., Parker, G. J., and Dyrby, T. B. (2010). Orientationally invariant indices of axon diameter and density from diffusion MRI. *NeuroImage*, 52(4):1374–1389.

Anderson, P. W. and Weiss, P. R. (1953). Exchange Narrowing in Paramagnetic Resonance. *Exchange Organizational Behavior Teaching Journal*, 679(1948).

Andersson, M., Kjer, H. M., Rafael-Patino, J., Pacureanu, A., Pakkenberg, B., Thiran, J. P., Ptito, M., Bech, M., Bjorholm Dahl, A., Andersen Dahl, V., and Dyrby, T. B. (2020). Axon morphology is modulated by the local environment and impacts the noninvasive investigation of its structure-function relationship. *Proceedings of the National Academy of Sciences of the United States of America*, 117(52):33649–33659.

Ashburner, J. and Friston, K. J. (2005). Unified segmentation. *NeuroImage*, 26(3):839–851.

Assaf, Y. and Basser, P. J. (2005). Composite hindered and restricted model of diffusion (CHARMED) MR imaging of the human brain. *NeuroImage*, 27(1):48–58.

Assaf, Y., Blumenfeld-Katzir, T., Yovel, Y., and J. Basser, P. (2008). AxCaliber: A Method for Measuring Axon Diameter Distribution from Diffusion MRI. *Magn Reson Med.*, 59(6):1347–1354.

Bagnato, F., Hametner, S., Boyd, E., Endmayr, V., Shi, Y., Ikonomidou, V., Chen, G., Pawate, S., Lassmann, H., Smith, S., and Brian Welch, E. (2018). Untangling the R2* contrast in multiple sclerosis: A combined MRI-histology study at 7.0 Tesla. *PLoS ONE*, 13(3):1–19.

Barakovic, M., Girard, G., Schiavi, S., Romascano, D., Descoteaux, M., Granziera, C., Jones, D. K., Innocenti, G. M., Thiran, J.-P., and Daducci, A. (2021). Bundle-Specific Axon Diameter Index as a New Contrast to Differentiate White Matter Tracts. *Frontiers in Neuroscience*, 15(June):1–13.

Barakovic, M., Pizzolato, M., Tax, C. M. W., Rudrapatna, U., Magon, S., Dyrby, T. B., Granziera, C., Thiran, J.-P., Jones, D. K., and Canales-Rodríguez, E. J. (2023). Relax! Diffusion is not the only way to estimate axon radius in vivo. *arXiv*, pages 1–48.

Barazany, D., Basser, P. J., and Assaf, Y. (2009). In vivo measurement of axon diameter distribution in the corpus callosum of rat brain. *Brain*, 132(5):1210–1220.

Barazany, D., Jones, D., and Assaf, Y. (2011). AxCaliber 3D. In *Proc. Intl. Soc. Mag. Reson. Med*, volume 19, page 76.

Barber, T. W., Brockway, J. A., and Higgins, L. S. (1970). The density of tissues in and about the head.

Acta Neurol. Scandinav., 46,:85–92.

Bartzokis, G., Sultzer, D., Mintz, J., Holt, L. E., Marx, P., Phelan, C. K., and Marder, S. R. (1994). In vivo evaluation of brain iron in Alzheimer's disease and normal subjects using MRI. *Biological Psychiatry*, 35(7):480–487.

Basso, D., Vecchi, T., Kabiri, L. A., Baschenis, I., Boggiani, E., and Bisiacchi, P. S. (2006). Handedness effects on interhemispheric transfer time: A TMS study. *Brain Research Bulletin*, 70(3):228–232.

Bauer, W. R. and Nadler, W. (2002). Spin dephasing in the extended strong collision approximation. *Physical Review E - Statistical Physics, Plasmas, Fluids, and Related Interdisciplinary Topics*, 65(6):1–15.

Benjamini, D., Komlosh, M. E., Basser, P. J., and Nevo, U. (2014). Nonparametric pore size distribution using d-PFG: Comparison to s-PFG and migration to MRI. *J Magn Reson*, 246(1):36–45.

Benjamini, D., Komlosh, M. E., Holtzclaw, L. A., Nevo, U., and Basser, P. J. (2016). White matter microstructure from nonparametric axon diameter distribution mapping. *NeuroImage*, 135:333–344.

Berman, S., Filo, S., and Mezer, A. A. (2019). Modeling conduction delays in the corpus callosum using MRI-measured g-ratio. *NeuroImage*, 195(March):128–139.

Berman, S., West, K. L., Does, M. D., Yeatman, J. D., and Mezer, A. A. (2018). Evaluating g-ratio weighted changes in the corpus callosum as a function of age and sex. *NeuroImage*, 182(June 2017):304–313.

Bilgic, B., Pfefferbaum, A., Rohlfing, T., Sullivan, E. V., and Adalsteinsson, E. (2012). MRI estimates of brain iron concentration in normal aging using quantitative susceptibility mapping. *NeuroImage*, 59(3):2625–2635.

Brammerloh, M., Morawski, M., Friedrich, I., Reinert, T., Lange, C., Pelicon, P., Vavpetič, P., Jankuhn, S., Jäger, C., Alkemade, A., Balesar, R., Pine, K., Gavriilidis, F., Trampel, R., Reimer, E., Arendt, T., Weiskopf, N., and Kirilina, E. (2021). Measuring the iron content of dopaminergic neurons in substantia nigra with MRI relaxometry. *NeuroImage*, 239(June):118255.

Brooks, R. A., Vymazal, J., Goldfarb, R. B., Bulte, J. W. M., and Aisen, P. (1998). Relaxometry and Magnetometry of Ferritin. *MRM*, 40:227–235.

Brown, W. S. and Jeeves, M. A. (1993). Bilateral visual field processing and evoked potential interhemispheric transmission time. *Neuropsychologia*, 31(12):1267–1281.

Brun, A. and Englund, E. (1986). A white matter disorder in dementia of the Alzheimer type: A pathoanatomical study. *Annals of Neurology*, 19(3):253–262.

Burcaw, L. M., Fieremans, E., and Novikov, D. S. (2015). Mesoscopic structure of neuronal tracts from time-dependent diffusion. *NeuroImage*, 114:18–37.

Caminiti, R., Ghaziri, H., Galuske, R., Hof, P. R., and Innocenti, G. M. (2009). Evolution amplified processing with temporally dispersed slow neuronal connectivity in primates. *PNAS*, 106(46):19551–19556.

Campbell, J. S., Leppert, I. R., Narayanan, S., Boudreau, M., Duval, T., Cohen-Adad, J., Pike, G. B., and Stikov, N. (2018). Promise and pitfalls of g-ratio estimation with MRI. *NeuroImage*, 182(July 2017):80–96.

Castella, R., Arn, L., Dupuis, E., Callaghan, M. F., Draganski, B., and Lutti, A. (2018). Controlling motion artefact levels in MR images by suspending data acquisition during periods of head motion. *Magnetic Resonance in Medicine*, 80(6):2415–2426.

Chaumillon, R., Blouin, J., and Guillaume, A. (2018). Interhemispheric transfer time asymmetry of visual information depends on eye dominance: An electrophysiological study. *Frontiers in Neuroscience*, 12(72):1–19.

Cluskey, S. and Ramsden, D. B. (2001). Mechanisms of neurodegeneration in amyotrophic lateral sclerosis. *Journal of Clinical Pathology - Molecular Pathology*, 54(6):386–392.

Creel, D. (2012). Visually evoked potentials. In *The Organization of the Retina and Visual System*. Webvision: The Organization of the Retina and Visual System [Internet].

Damulina, A., Pirpamer, L., Soellradl, M., Sackl, M., Tinauer, C., Hofer, E., Enzinger, C., Gesierich, B., Duering, M., Ropele, S., Schmidt, R., and Langkammer, C. (2020). Cross-sectional and longitudinal assessment of brain iron level in Alzheimer disease using 3-T MRI. *Radiology*, 296(3):619–626.

Deftereos, S. N., Panagopoulos, G., Georgonikou, D., Karageorgiou, E., Andriopoulos, P., and Karageorgiou, C. E. (2008). On the calculation of transcallosal conduction time using transcranial magnetic stimulation. *Functional Neurology*, 23(3):137–140.

Deistung, A., Schäfer, A., Schweser, F., Biedermann, U., Turner, R., and Reichenbach, J. R. (2013). Toward in vivo histology: A comparison of quantitative susceptibility mapping (QSM) with magnitude-, phase-, and R2*-imaging at ultra-high magnetic field strength. *NeuroImage*, 65:299–314.

Deistung, A., Schweser, F., and Reichenbach, J. R. (2017). Overview of quantitative susceptibility mapping. *NMR in Biomedicine*, 30(4).

Dell'Acqua, V. P., Tax, C. M. W., Molendowska, M., Parker, G. D., Jones, D. K., Barakovic, M., and Canales-Rodriguez, E. J. (2023). Assessing the robustness of the correlation between intra-axonal T2 and axon diameter across participants. *Proc. Intl. Soc. Mag. Reson. Med. 23*, page 2028.

Deslauriers-Gauthier, S. and Deriche, R. (2019). Estimation of axonal conduction speed and the inter hemispheric transfer time using connectivity informed maximum entropy on the mean. *HAL*, page 12.

Deslauriers-Gauthier, S., Lina, J. M., Butler, R., Whittingstall, K., Gilbert, G., Bernier, P. M., Deriche, R., and Descoteaux, M. (2019). White matter information flow mapping from diffusion MRI and EEG. *NeuroImage*, 201:116017.

Dick, F., Tierney, A. T., Lutti, A., Josephs, O., Sereno, M. I., and Weiskopf, N. (2012). In vivo functional and myeloarchitectonic mapping of human primary auditory areas. *Journal of Neuroscience*, 32(46):16095–16105.

Does, M. D. (2018). Inferring Brain Tissue Composition and Microstructure via MR Relaxometry. *Neuroimage*, 182:136–148.

Does, M. D., Olesen, J. L., Harkins, K. D., Serradas-Duarte, T., Gochberg, D. F., Jespersen, S. N., and Shemesh, N. (2019). Evaluation of principal component analysis image denoising on multi-exponential MRI relaxometry. *Magnetic Resonance in Medicine*, 81:3503–3514.

Drakesmith, M., Harms, R., Rudrapatna, S. U., Parker, G. D., Evans, C. J., and Jones, D. K. (2019). Estimating axon conduction velocity in vivo from microstructural MRI. *NeuroImage*, 203:116186.

Duyn, J. H. and Schenck, J. (2017). Contributions to magnetic susceptibility of brain tissue. *NMR in Biomedicine*, 30(4).

Duyn, J. H., Van Gelderen, P., Li, T. Q., De Zwart, J. A., Koretsky, A. P., and Fukunaga, M. (2007). High-field MRI of brain cortical substructure based on signal phase. *Proceedings of the National Academy of Sciences of the United States of America*, 104(28):11796–11801.

Edwards, L. J., Kirilina, E., Mohammadi, S., and Weiskopf, N. (2018). Microstructural imaging of human

neocortex in vivo. *NeuroImage*, 182(February):184–206.

Evangelou, N., Konz, D., Esiri, M. M., Smith, S., Palace, J., and Matthews, P. M. (2001). Size-selective neuronal changes in the anterior optic pathways suggest a differential susceptibility to injury in multiple sclerosis. *Brain*, 124(9):1813–1820.

Fan, Q., Nummenmaa, A., Witzel, T., Ohringer, N., Tian, Q., Setsompop, K., Klawiter, E. C., Rosen, B. R., Wald, L. L., and Huang, S. Y. (2020). Axon diameter index estimation independent of fiber orientation distribution using high-gradient diffusion MRI. *NeuroImage*, 222(August):117197.

Fan, Q., Tian, Q., Ohringer, N. A., Nummenmaa, A., Witzel, T., Tobyne, S. M., Klawiter, E. C., Mekkaoui, C., Rosen, B. R., Wald, L. L., Salat, D. H., and Huang, S. Y. (2019). Age-related alterations in axonal microstructure in the corpus callosum measured by high-gradient diffusion MRI. *NeuroImage*, 191(February):325–336.

Fieremans, E., Novikov, D. S., Jensen, J. H., and Helpern, J. A. (2010). Monte Carlo study of a two-compartment exchange model of diffusion. *NMR in Biomedicine*, 23(7):711–724.

Fischl, B. and Dale, A. M. (2000). Measuring the thickness of the human cerebral cortex from magnetic resonance images. *Proceedings of the National Academy of Sciences of the United States of America*, 97(20):11050–11055.

Friederici, A. D., von Cramon, D. Y., and Kotz, S. A. (2007). Role of the Corpus Callosum in Speech Comprehension: Interfacing Syntax and Prosody. *Neuron*, 53(1):135–145.

Friedrich, I., Reimann, K., Jankuhn, S., Kirilina, E., Stieler, J., Sonntag, M., Meijer, J., Weiskopf, N., Reinert, T., Arendt, T., and Morawski, M. (2021). Cell specific quantitative iron mapping on brain slices by immuno-µPIXE in healthy elderly and Parkinson's disease. *Acta Neuropathologica Communications*, 9(1):1–17.

Friedrich, P., Ocklenburg, S., Mochalski, L., Schlüter, C., Güntürkün, O., and Genc, E. (2017). Long-term reliability of the visual EEG Poffenberger paradigm. *Behavioural Brain Research*, 330:85–91.

Fukunaga, M., Li, T. Q., Van Gelderen, P., De Zwart, J. A., Shmueli, K., Yao, B., Lee, J., Maric, D., Aronova, M. A., Zhang, G., Leapman, R. D., Schenck, J. F., Merkle, H., and Duyn, J. H. (2010). Layer-specific variation of iron content in cerebral cortex as a source of MRI contrast. *Proceedings of the National Academy of Sciences of the United States of America*, 107(8):3834–3839.

Gast, H., Horowitz, A., Krupnik, R., Barazany, D., Lifshits, S., Ben-Amitay, S., and Assaf, Y. (2023). A Method for In-Vivo Mapping of Axonal Diameter Distributions in the Human Brain Using Diffusion-Based Axonal Spectrum Imaging (AxSI). *Neuroinformatics*.

Gerlach, M., Ben-Shachar, D., Riederer, P., and Youdim, M. B. (1994). Altered brain metabolism of iron as a cause of neurodegenerative diseases? *Journal of Neurochemistry*, 63(3):793–807.

Glover, G. H. (2011). Overview of functional magnetic resonance imaging. *Neurosurgery Clinics of North America*, 22(2):133–139.

Graham, J. M., Paley, M. N., Grünewald, R. A., Hoggard, N., and Griffiths, P. D. (2000). Brain iron deposition in Parkinson's disease imaged using the PRIME magnetic resonance sequence. *Brain*, 123(12):2423–2431.

Grossman, R. I. and McGowan, J. C. (1998). Perspectives on multiple sclerosis. *American Journal of Neuroradiology*, 19(7):1251–1265.

Haacke, E. M., Cheng, N. Y., House, M. J., Liu, Q., Neelavalli, J., Ogg, R. J., Khan, A., Ayaz, M., Kirsch, W., and Obenaus, A. (2005). Imaging iron stores in the brain using magnetic resonance imaging.

Magnetic Resonance Imaging, 23(1):1–25.

Haacke, E. M., Liu, S., Buch, S., Zheng, W., Wu, D., and Ye, Y. (2015). Quantitative susceptibility mapping: Current status and future directions. *Magnetic Resonance Imaging*, 33(1):1–25.

Hagiwara, A., Hori, M., Yokoyama, K., Nakazawa, M., Ueda, R., Horita, M., Andica, C., Abe, O., and Aoki, S. (2017). Analysis of white matter damage in patients with multiple sclerosis via a novel in Vivo MR method for measuring myelin, axons, and G-ratio. *American Journal of Neuroradiology*, 38(10):1934–1940.

Hagmann, P., Jonasson, L., Maeder, P., Thiran, J. P., Wedeen, J. V., and Meuli, R. (2006). Understanding diffusion MR imaging techniques: From scalar diffusion-weighted imaging to diffusion tensor imaging and beyond. *Radiographics*, 26:205–223.

Hallgren, B. and Sourander, P. (1958). The effect of age on non-haemin iron in the human brain. *Journal of Neurochemistry*, 3:41–51.

Hare, D., Ayton, S., Bush, A., and Lei, P. (2013). A delicate balance: Iron metabolism and diseases of the brain. *Frontiers in Aging Neuroscience*, 5:1–19.

Helbling, S., Teki, S., Callaghan, M. F., Sedley, W., Mohammadi, S., Griffiths, T. D., Weiskopf, N., and Barnes, G. R. (2015). Structure predicts function: Combining non-invasive electrophysiology with in-vivo histology. *NeuroImage*, 108:377–385.

Helms, G., Dathe, H., and Dechent, P. (2008a). Quantitative FLASH MRI at 3T using a rational approximation of the Ernst equation. *Magnetic Resonance in Medicine*, 59(3):667–672.

Helms, G., Dathe, H., Kallenberg, K., and Dechent, P. (2008b). High-resolution maps of magnetization transfer with inherent correction for RF inhomogeneity and T1 relaxation obtained from 3D FLASH MRI. *Magnetic Resonance in Medicine*, 60(6):1396–1407.

Honey, C. J., Thivierge, J. P., and Sporns, O. (2010). Can structure predict function in the human brain? *NeuroImage*, 52(3):766–776.

Horowitz, A., Barazany, D., Tavor, I., Bernstein, M., Yovel, G., and Assaf, Y. (2015). In vivo correlation between axon diameter and conduction velocity in the human brain. *Brain Structure and Function*, 220(3):1777–1788.

Huang, S. Y., Nummenmaa, A., Witzel, T., Duval, T., Cohen-Adad, J., Wald, L. L., and McNab, J. A. (2015). The impact of gradient strength on in vivo diffusion MRI estimates of axon diameter. *NeuroImage*, 106:464–472.

Jelescu, I. O., Palombo, M., Bagnato, F., and Schilling, K. G. (2020). Challenges for biophysical modeling of microstructure. *Journal of Neuroscience Methods*, 344:108861.

Jelescu, I. O., Veraart, J., Fieremans, E., and Novikov, D. S. (2016). Degeneracy in model parameter estimation for multi-compartmental diffusion in neuronal tissue. *NMR in Biomedicine*, 29:33–47.

Jensen, J. H. and Chandra, R. (1999). Transverse relaxation time field dependence for tissues with microscopic magnetic susceptibility variations. *Proc. Int. Soc. Mag. Reson. Med.*, 7:656.

Jensen, J. H. and Chandra, R. (2000). NMR relaxation in tissues with weak magnetic inhomogeneities. *Magnetic Resonance in Medicine*, 44(1):144–156.

Jones, D. K., Alexander, D. C., Bowtell, R., Cercignani, M., Dell'Acqua, F., McHugh, D. J., Miller, K. L., Palombo, M., Parker, G. J., Rudrapatna, U. S., and Tax, C. M. (2018). Microstructural imaging of the human brain with a 'super-scanner': 10 key advantages of ultra-strong gradients for diffusion MRI. *NeuroImage*, 182:8–38.

Jung, W., Lee, J., Shin, H. G., Nam, Y., Zhang, H., Oh, S. H., and Lee, J. (2018). Whole brain g-ratio mapping using myelin water imaging (MWI) and neurite orientation dispersion and density imaging (NODDI). *NeuroImage*, 182(September 2017):379–388.

Kirilina, E., Helbling, S., Morawski, M., Pine, K., Reimann, K., Jankuhn, S., Dinse, J., Deistung, A., Reichenbach, J. R., Trampel, R., Geyer, S., Müller, L., Jakubowski, N., Arendt, T., Bazin, P. L., and Weiskopf, N. (2020). Superficial white matter imaging: Contrast mechanisms and whole-brain in vivo mapping. *Science Advances*, 6(41).

Kiselev, V. G. and Novikov, D. S. (2002). Transverse NMR Relaxation as a Probe of Mesoscopic Structure. *Physical Review Letters*, 89(27):2–5.

Kiselev, V. G. and Novikov, D. S. (2018). Transverse NMR relaxation in biological tissues. *NeuroImage*, 182(June):149–168.

Koenig, S. H. (1991). Cholesterol of myelin is the determinant of gray-white contrast in MRI of brain. *Magnetic Resonance in Medicine*, 20(2):285–291.

Krebs, N., Langkammer, C., Goessler, W., Ropele, S., Fazekas, F., Yen, K., and Scheurer, E. (2014). Assessment of trace elements in human brain using inductively coupled plasma mass spectrometry. *Journal of Trace Elements in Medicine and Biology*, 28(1):1–7.

Lamantia, A. S. and Rakic, P. (1990). Cytological and quantitative characteristics of four cerebral commissures in the rhesus monkey. *The Journal of Comparative Neurology*, 291(4):520–537.

Langkammer, C., Krebs, N., Goessler, W., Scheurer, E., Ebner, F., Yen, K., Fazekas, F., and Ropele, S. (2010). Quantitative MR imaging of brain iron: A postmortem validation study. *Radiology*, 257(2):455–462.

Langkammer, C., Schweser, F., Krebs, N., Deistung, A., Goessler, W., Scheurer, E., Sommer, K., Reishofer, G., Yen, K., Fazekas, F., Ropele, S., and Reichenbach, J. R. (2012). Quantitative susceptibility mapping (QSM) as a means to measure brain iron? A post mortem validation study. *NeuroImage*, 62(3):1593–1599.

Laule, C., Vavasour, I. M., Kolind, S. H., Li, D. K. B., Traboulsee, T. L., Moore, G. R. W., and MacKay, A. L. (2007). Magnetic Resonance Imaging of Myelin. *Neurotherapeutics: The Journal of the American Society for Experimental NeuroTherapeutics Magnetic*, 4(July):460–484.

Lazari, A. and Lipp, I. (2021). Can MRI measure myelin? Systematic review, qualitative assessment, and meta-analysis of studies validating microstructural imaging with myelin histology. *NeuroImage*, 230(January):117744.

Lee, H. H., Fieremans, E., and Novikov, D. S. (2018). What dominates the time dependence of diffusion transverse to axons: Intra- or extra-axonal water? *NeuroImage*, 182:500–510.

Lee, H. H., Yaros, K., Veraart, J., Pathan, J. L., Liang, F. X., Kim, S. G., Novikov, D. S., and Fieremans, E. (2019). Along-axon diameter variation and axonal orientation dispersion revealed with 3D electron microscopy: implications for quantifying brain white matter microstructure with histology and diffusion MRI. *Brain Structure and Function*, 224(4):1469–1488.

Lee, J., Shmueli, K., Kang, B. T., Yao, B., Fukunaga, M., Van Gelderen, P., Palumbo, S., Bosetti, F., Silva, A. C., and Duyn, J. H. (2012). The contribution of myelin to magnetic susceptibility-weighted contrasts in high-field MRI of the brain. *NeuroImage*, 59(4):3967–3975.

Lemarechal, J. D., Jedynak, M., Trebaul, L., Boyer, A., Tadel, F., Bhattacharjee, M., Deman, P., Tuyisenge, V., Ayoubian, L., Hugues, E., Chanteloup-Forêt, B., Saubat, C., Zouglech, R., Reyes Mejia, G. C., Tourbier, S., Hagmann, P., Adam, C., Barba, C., Bartolomei, F., Blauwblomme, T., Curot, J.,

Dubeau, F., Francione, S., Garces, M., Hirsch, E., Landre, E., Liu, S., Maillard, L., Metsähonkala, E. L., Mindruta, I., Nica, A., Pail, M., Petrescu, A. M., Rheims, S., Rocamora, R., Schulze-Bonhage, A., Szurhaj, W., Taussig, D., Valentin, A., Wang, H., Kahane, P., George, N., David, O., Adam, C., Navarro, V., Biraben, A., Nica, A., Menard, D., Brazdil, M., Kuba, R., Kočvarová, J., Pail, M., Dolealová, I., Dubeau, F., Gotman, J., Ryvlin, P., Isnard, J., Catenoix, H., Montavont, A., Rheims, S., Bartolomei, F., Trebuchon, A., Mcgonigal, A., Zhou, W., Wang, H., Liu, S., Wei, Z., Dan, Z., Qiang, G., Xiangshu, H., Hua, L., Gang, H., Wensheng, W., Xi, M., Yigang, F., Nabbout, R., Bourgeois, M., Kaminska, A., Blauwblomme, T., Garces, M., Valentin, A., Singh, R., Metsähonkala, L., Gaily, E., Lauronen, L., Peltola, M., Chassoux, F., Landre, E., Derambure, P., Szurhaj, W., Chochois, M., Hirsch, E., Paola Valenti, M., Scholly, J., Valton, L., Denuelle, M., Curot, J., Rocamora, R., Principe, A., Ley, M., Mindruta, I., Barborica, A., Francione, S., Mai, R., Nobili, L., Sartori, I., Tassi, L., Maillard, L., Vignal, J. P., Jonas, J., Tyvaert, L., Chipaux, M., Taussig, D., Kahane, P., Minotti, L., Job, A. S., Michel, V., De Montaudoin, M., Aupy, J., Bouilleret, V., Maria Petrescu, A., Masnou, P., Dussaule, C., Quirins, M., Taussig, D., Barba, C., Guerrini, R., Lenge, M., and Nacci, E. (2022). A brain atlas of axonal and synaptic delays based on modelling of cortico-cortical evoked potentials. *Brain*, 145(5):1653–1667.

Li, L. and Leigh, J. S. (2004). Quantifying Arbitrary Magnetic Susceptibility Distributions with MR. *Magnetic Resonance in Medicine*, 51(5):1077–1082.

Liewald, D., Miller, R., Logothetis, N., Wagner, H. J., and Schüz, A. (2014). Distribution of axon diameters in cortical white matter: an electron-microscopic study on three human brains and a macaque. *Biological Cybernetics*, 108(5):541–557.

Lo, Y. L. and Fook-Chong, S. (2004). A transcranial magnetic stimulation study of the ipsilateral silent period in lower limb muscles. *Neuroscience Letters*, 368(3):337–340.

Lutti, A., Corbin, N., Ashburner, J., Ziegler, G., Draganski, B., Phillips, C., Kherif, F., Callaghan, M. F., and Domenicantonio, G. D. (2022). Restoring statistical validity in group analyses of motion- corrupted MRI data. *Human Brain Mapping*, pages 1–11.

Lutti, A., Hutton, C., Finsterbusch, J., Helms, G., and Weiskopf, N. (2010). Optimization and validation of methods for mapping of the radiofrequency transmit field at 3T. *Magnetic Resonance in Medicine*, 64(1):229–238.

Lutti, A., Stadler, J., Josephs, O., Windischberger, C., Speck, O., Bernarding, J., Hutton, C., and Weiskopf, N. (2012). Robust and fast whole brain mapping of the RF transmit field B1 at 7T. *PLoS ONE*, 7(3):1–7.

Mackay, A., Whittall, K., Adler, J., Li, D., Paty, D., and Graeb, D. (1994). In vivo visualization of myelin water in brain by magnetic resonance. *Magnetic Resonance in Medicine*, 31(6):673–677.

MacKay, A. L. and Laule, C. (2016). Magnetic Resonance of Myelin Water: An in vivo Marker for Myelin. *Brain Plasticity*, 2(1):71–91.

Maclaren, J., Armstrong, B. S., Barrows, R. T., Danishad, K. A., Ernst, T., Foster, C. L., Gumus, K., Herbst, M., Kadashevich, I. Y., Kusik, T. P., Li, Q., Lovell-Smith, C., Prieto, T., Schulze, P., Speck, O., Stucht, D., and Zaitsev, M. (2012). Measurement and Correction of Microscopic Head Motion during Magnetic Resonance Imaging of the Brain. *PLoS ONE*, 7(11):3–11.

Mahjoory, K., Nikulin, V. V., Botrel, L., Linkenkaer-Hansen, K., Fato, M. M., and Haufe, S. (2017). Consistency of EEG source localization and connectivity estimates. *NeuroImage*, 152(February):590–601.

Mancini, M., Karakuzu, A., Cohen-Adad, J., Cercignani, M., Nichols, T. E., and Stikov, N. (2020). An interactive meta-analysis of MRI biomarkers of Myelin. *eLife*, 9:1–23.

Marques, J. P., Khabipova, D., and Gruetter, R. (2017). Studying cyto and myeloarchitecture of the

human cortex at ultra-high field with quantitative imaging: R1, R2* and magnetic susceptibility. *NeuroImage*, 147:152–163.

Marzi, C. (1999). The Poffenberger paradigm: A first, simple, behavioural tool to study interhemispheric transmission in humans. *Brain Research Bulletin*, 50(5-6):421–422.

Marzi, C. A., Bisiacchi, P., and Nicoletti, R. (1991). Is interhemispheric transfer of visuomotor information asymmetric? Evidence from a meta-analysis. *Neuropsychologia*, 29(12):1163–1177.

Marzi, C. A., Mancini, F., and Savazzi, S. (2009). Interhemispheric transfer of phosphenes generated by occipital versus parietal transcranial magnetic stimulation. *Experimental Brain Research*, 192(3):431–441.

Miller, T. R., Mohan, S., Choudhri, A. F., Gandhi, D., and Jindal, G. (2014). Advances in Multiple Sclerosis and its Variants. Conventional and Newer Imaging Techniques. *Radiologic Clinics of North America*, 52(2):321–336.

Mohammadi, S. and Callaghan, M. F. (2021). Towards in vivo g-ratio mapping using MRI: Unifying myelin and diffusion imaging. *Journal of Neuroscience Methods*, 348(September 2020):108990.

Möller, H. E., Bossoni, L., Connor, J. R., Crichton, R. R., Does, M. D., Ward, R. J., Zecca, L., Zucca, F. A., and Ronen, I. (2019). Iron , Myelin , and the Brain : Neuroimaging Meets Neurobiology. *Trends in Neurosciences*, 42(6):384–401.

Nilsson, M., Lasič, S., Drobnjak, I., Topgaard, D., and Westin, C. F. (2017). Resolution limit of cylinder diameter estimation by diffusion MRI: The impact of gradient waveform and orientation dispersion. *NMR in Biomedicine*, 30(7):1–13.

Novikov, D. S., Kiselev, V. G., and Jespersen, S. N. (2018). On modeling. *Magn Reson Med*, 79(6):3172–3193.

Ogg, R. J. and Steen, R. G. (1998). Age-related changes in Brain T1 are correlated with iron concentration. *Magn Reson Med*, 40(5):749–753.

Oliveira, R., Lucia, M. D., and Lutti, A. (2023). Single-subject electroencephalography measurement of interhemispheric transfer time. *Human Brain Mapping*, pages 1–16.

Oliveira, R., Pelentritou, A., Di Domenicantonio, G., De Lucia, M., and Lutti, A. (2022). In vivo Estimation of Axonal Morphology From Magnetic Resonance Imaging and Electroencephalography Data. *Frontiers in Neuroscience*, 16(April):1–18.

Panagiotaki, E., Schneider, T., Siow, B., Hall, M. G., Lythgoe, M. F., and Alexander, D. C. (2012). Compartment models of the diffusion MR signal in brain white matter: A taxonomy and comparison. *NeuroImage*, 59(3):2241–2254.

Paquette, M., Eichner, C., and Kn, T. R. (2020). Axon Diameter Measurements using Diffusion MRI are Infeasible. *BioRxiv*, pages 1–29.

Péran, P., Cherubini, A., Luccichenti, G., Hagberg, G., Démonet, J. F., Rascol, O., Celsis, P., Caltagirone, C., Spalletta, G., and Sabatini, U. (2009). Volume and iron content in basal ganglia and thalamus. *Human Brain Mapping*, 30(8):2667–2675.

Peters, A. (2009). The effects of normal aging on myelinated nerve fibers in monkey central nervous system. *Frontiers in Neuroanatomy*, 3(11):1–10.

Pike, G. B. (1996). Pulsed Magnetization Transfer Contrast in Gradient Echo Imaging: A Two-Pool Analytic Description of Signal Response. *MRM*, 36:95–103.

Plomp, G., Michel, C. M., and Herzog, M. H. (2010). Electrical source dynamics in three functional localizer paradigms. *NeuroImage*, 53(1):257–267.

Raynaud, Q., Yerly, J., Heeswijk, R. B. v., and Lutti, A. (2022). Characterization of cardiac noise in brain quantitative relaxometry MRI data. In *Proc. Intl. Soc. Mag. Reson. Med.*, page 3908.

Romascano, D., Barakovic, M., Rafael-Patino, J., Dyrby, T. B., Thiran, J. P., and Daducci, A. (2019). ActiveAxADD: Toward non-parametric and orientationally invariant axon diameter distribution mapping using PGSE. *Magnetic Resonance in Medicine*, 00:1–9.

Rushton, W. (1951). A theory of the effects of fibre size in medullated nerve. *J. Physiol.*, pages 101–122.

Saron, C. and Foxe, J. J. (2003). Complexities of Interhemispheric Communication in Sensorimotor Tasks Revealed by High-Density Event-Related Potential Mapping. In Eds., R. J., editor, *The Asymmetrical Brain*, chapter 10, page 342-408. Cambridge, MA: MIT press.

Saron, C. D. and Davidson, R. J. (1989). Visual Evoked Potential Measures of Interhemispheric Transfer Time in Humans. *Behavioral Neuroscience*, 103(5):1115–1138.

Schenck, J. F. (1992). Health and Physiological Effects of Human Exposure to Whole-Body Four-Tesla Magnetic Fields during MRI. *Annals of the New York Academy of Sciences*, 649(1):285–301.

Schenck, J. F. (1996). The role of magnetic susceptibility in magnetic resonance imaging: MRI magnetic compatibility of the first and second kinds. *Medical Physics*, 23(6):815–850.

Schweser, F., Deistung, A., Lehr, B. W., and Reichenbach, J. R. (2011a). Quantitative imaging of intrinsic magnetic tissue properties using MRI signal phase: An approach to in vivo brain iron metabolism? *NeuroImage*, 54(4):2789–2807.

Schweser, F., Deistung, A., Lehr, B. W., Sommer, K., and Reichenbach, J. R. (2011b). SEMI-TWInS: Simultaneous Extraction of Myelin and Iron using a T2*-Weighted Imaging Sequence. *Proc. Intl. Soc. Mag. Reson. Med. 19*, page 120.

Sedlacik, J., Boelmans, K., Löbel, U., Holst, B., Siemonsen, S., and Fiehler, J. (2014). Reversible, irreversible and effective transverse relaxation rates in normal aging brain at 3T. *NeuroImage*, 84:1032–1041.

Shin, H. G., Lee, J., Yun, Y. H., Yoo, S. H., Jang, J., Oh, S. H., Nam, Y., Jung, S., Kim, S., Fukunaga, M., Kim, W., Choi, H. J., and Lee, J. (2021). χ-separation: Magnetic susceptibility source separation toward iron and myelin mapping in the brain. *NeuroImage*, 240(February):118371.

Sorrentino, P., Petkoski, S., Sparaco, M., Lopez, E. T., Rucco, R., Signoriello, E., Baselice, F., Bonavita, S., Pirozzi, M., Quarantelli, M., Sorrentino, G., and Jirsa, V. (2021). On the topochronic map of the human brain dynamics. *bioRxiv*, page 2021.07.01.447872.

Sorrentino, P., Petkoski, S., Sparaco, M., Troisi Lopez, E., Signoriello, E., Baselice, F., Bonavita, S., Pirozzi, M. A., Quarantelli, M., Sorrentino, G., and Jirsa, V. (2022). Whole-brain propagation delays in multiple sclerosis, a combined tractography - magnetoencephalography study. *The Journal of Neuroscience*, 42(47):0938–22.

Spitzer, C., Willert, C., Grabe, H. J., Rizos, T., Möller, B., and Freyberger, H. J. (2004). Dissociation, Hemispheric Asymmetry, and Dysfunction of Hemispheric Interaction: A Transcranial Magnetic Stimulation Approach. *Journal of Neuropsychiatry and Clinical Neurosciences*, 16(2):163–169.

Stahon, K. E., Bastian, C., Griffith, S., Kidd, G. J., Brunet, S., and Baltan, S. (2016). Age-related changes in axonal and mitochondrial ultrastructure and function in white matter. *Journal of Neuroscience*, 36(39):9990–10001.

Stanisz, G. J., Szafer, A., Wright, G. A., and Henkelman, R. M. (1997). An analytical model of restricted diffusion in bovine optic nerve. *Magnetic Resonance in Medicine*, 37(1):103–111.

Stedehouder, J. and Kushner, S. A. (2017). Myelination of parvalbumin interneurons: A parsimonious locus of pathophysiological convergence in schizophrenia. *Molecular Psychiatry*, 22(1):4–12.

Stephan, K. E., Tittgemeyer, M., Knösche, T. R., Moran, R. J., and Friston, K. J. (2009). Tractography-based priors for dynamic causal models. *NeuroImage*, 47(4):1628–1638.

Stikov, N., Campbell, J. S., Stroh, T., Lavelée, M., Frey, S., Novek, J., Nuara, S., Ho, M. K., Bedell, B. J., Dougherty, R. F., Leppert, I. R., Boudreau, M., Narayanan, S., Duval, T., Cohen-Adad, J., Picard, P. A., Gasecka, A., Côté, D., and Pike, G. B. (2015). In vivo histology of the myelin g-ratio with magnetic resonance imaging. *NeuroImage*, 118:397–405.

Stikov, N., Perry, L. M., Mezer, A., Rykhlevskaia, E., Wandell, B. A., Pauly, J. M., and Dougherty, R. F. (2011). Bound pool fractions complement diffusion measures to describe white matter micro and macrostructure. *NeuroImage*, 54(2):1112–1121.

Storey, P., Chung, S., Ben-Eliezer, N., Lemberskiy, G., Lui, Y. W., and Novikov, D. S. (2015). Signatures of Microstructure in Conventional Gradient and Spin Echo Signals. In *Proc. 23rd Annual Meeting ISMRM, Toronto, Canada*, page 014.

Stüber, C., Morawski, M., Schäfer, A., Labadie, C., Wähnert, M., Leuze, C., Streicher, M., Barapatre, N., Reimann, K., Geyer, S., Spemann, D., and Turner, R. (2014). Myelin and iron concentration in the human brain: A quantitative study of MRI contrast. *NeuroImage*, 93(P1):95–106.

Sukstanskii, A. L. and Yablonskiy, D. A. (2003). Gaussian approximation in the theory of MR signal formation in the presence of structure-specific magnetic field inhomogeneities. *Journal of Magnetic Resonance*, 163(2):236–247.

Tabelow, K., Balteau, E., Ashburner, J., Callaghan, M. F., Draganski, B., Helms, G., Kherif, F., Leutritz, T., Lutti, A., Phillips, C., Reimer, E., Ruthotto, L., Seif, M., Weiskopf, N., Ziegler, G., and Mohammadi, S. (2019). hMRI – A toolbox for quantitative MRI in neuroscience and clinical research. *NeuroImage*, 194:191–210.

Taege, Y., Hagemeier, J., Bergsland, N., Dwyer, M. G., Weinstock-Guttman, B., Zivadinov, R., and Schweser, F. (2019). Assessment of mesoscopic properties of deep gray matter iron through a model-based simultaneous analysis of magnetic susceptibility and R2* - A pilot study in patients with multiple sclerosis and normal controls. *NeuroImage*, 186(November 2018):308–320.

Thompson, K. J., Shoham, S., and Connor, J. R. (2001). Iron and neurodegenerative disorders. *Brain Research Bulletin*, 55(2):155–164.

Tomasi, S., Caminiti, R., and Innocenti, G. M. (2012). Areal differences in diameter and length of corticofugal projections. *Cerebral Cortex*, 22(6):1463–1472.

Ulla, M., Bonny, J. M., Ouchchane, L., Rieu, I., Claise, B., and Durif, F. (2013). Is R2* a New MRI Biomarker for the Progression of Parkinson's Disease? A Longitudinal Follow-Up. *PLoS ONE*, 8(3):1–8.

Ulrich, X. and Yablonskiy, D. A. (2016). Separation of cellular and BOLD contributions to T2* signal relaxation. *Magnetic Resonance in Medicine*, 75(2):606–615.

Veraart, J., Nunes, D., Rudrapatna, U., Fieremans, E., Jones, D. K., Novikov, D. S., and Shemesh, N. (2020). Nonivasive quantification of axon radii using diffusion MRI. *eLife*, pages 1–27.

Veraart, J., Raven, E. P., Jones, D. K., and Palombo, M. (2023). Axon diameter mapping is confounded

by glial cells. *Proc. Intl. Soc. Mag. Reson. Med. 23*, page 0973.

Vymazal, J., Hajek, M., Patronas, N., Giedd, J. N., Bulte, J. W., Baumgarner, C., Tran, V., and Brooks, R. A. (1995). The quantitative Relation Between T1-Weighted and T2-Weighted MRI of Normal gray Matter and iron concentration. *Journal of Magnetic Resonance Imaging*, 5(5):554–560.

Ward, R. J., Zucca, F. A., Duyn, J. H., Crichton, R. R., and Zecca, L. (2014). The role of iron in brain ageing and neurodegenerative disorders. *The Lancet Neurology*, 13(10):1045–1060.

Waxman, S. and Bennett, M. (1972). Relative Conduction Velocities of Small Myelinated and Non-myelinated Fibres in the Central Nervous System. *Nature New Biology*, 238:217–219.

Wegiel, J., Kaczmarski, W., Flory, M., Martinez-Cerdeno, V., Wisniewski, T., Nowicki, K., Kuchna, I., and Wegiel, J. (2018). Deficit of corpus callosum axons, reduced axon diameter and decreased area are markers of abnormal development of interhemispheric connections in autistic subjects. *Acta neuropathologica communications*, 6(1):143.

Weiskopf, N., Callaghan, M. F., Josephs, O., Lutti, A., and Mohammadi, S. (2014). Estimating the apparent transverse relaxation time (R2*) from images with different contrasts (ESTATICS) reduces motion artifacts. *Frontiers in Neuroscience*, 8:1–10.

Weiskopf, N., Mohammadi, S., Lutti, A., and Callaghan, M. F. (2015). Advances in MRI-based computational neuroanatomy: From morphometry to in-vivo histology. *Current Opinion in Neurology*, 28(4):313–322.

West, K. L., Kelm, N. D., Carson, R. P., and Does, M. D. (2016). A revised model for estimating g-ratio from MRI. *NeuroImage*, 125:1155–1158.

Westerhausen, R., Kreuder, F., Woerner, W., Huster, R. J., Smit, C. M., Schweiger, E., and Wittling, W. (2006). Interhemispheric transfer time and structural properties of the corpus callosum. *Neuroscience Letters*, 409(2):140–145.

Wharton, S. and Bowtell, R. (2012). Fiber orientation-dependent white matter contrast in gradient echo MRI. *Proceedings of the National Academy of Sciences of the United States of America*, 109(45):18559–18564.

Yablonskiy, D. A. and Haacke, E. M. (1994). Theory of NMR signal behavior in magnetically inhomogeneous tissues: The static dephasing regime. *Magnetic Resonance in Medicine*, 32(6):749–763.

Yablonskiy, D. A., Wen, J., Kothapalli, S. V., and Sukstanskii, A. L. (2021). In vivo evaluation of heme and non-heme iron content and neuronal density in human basal ganglia. *NeuroImage*, 235(April):118012.

Yao, B., Li, T. Q., Gelderen, P. v., Shmueli, K., de Zwart, J. A., and Duyn, J. H. (2009). Susceptibility contrast in high field MRI of human brain as a function of tissue iron content. *NeuroImage*, 44(4):1259–1266.

Zaitsev, M., Dold, C., Sakas, G., Hennig, J., and Speck, O. (2006). Magnetic resonance imaging of freely moving objects: prospective real-time motion correction using an external optical motion tracking system. *NeuroImage*, 31(3):1038–1050.

Zecca, L., Stroppolo, A., Gatti, A., Tampellini, D., Toscani, M., Gallorini, M., Giaveri, G., Arosio, P., Santambrogio, P., Fariello, R. G., Karatekin, E., Kleinman, M. H., Turro, N., Hornykiewicz, O., and Zucca, F. A. (2004). The role of iron and molecules in the neuronal vulnerability of locus coeruleus and substantia nigra during aging. *Proceedings of the National Academy of Sciences of the United States of America*, 101(26):9843–9848.

Zhang, H., Dyrby, T. B., and Alexander, D. C. (2011a). Axon diameter mapping in crossing fibers with

diffusion MRI. *MICCAI*, 14:82–89.

Zhang, H., Hubbard, P. L., Parker, G. J., and Alexander, D. C. (2011b). Axon diameter mapping in the presence of orientation dispersion with diffusion MRI. *NeuroImage*, 56(3):1301–1315.

Zhang, H., Schneider, T., Wheeler-kingshott, C. A., and Alexander, D. C. (2012). NODDI : Practical in vivo neurite orientation dispersion and density imaging of the human brain. *NeuroImage*, 61(4):1000–1016.

Zhao, Y., Wen, J., Cross, A. H., and Yablonskiy, D. A. (2016). On the relationship between cellular and hemodynamic properties of the human brain cortex throughout adult lifespan. *NeuroImage*, 133:417–429.

Ziegler, G., Hauser, T. U., Moutoussis, M., Bullmore, E. T., Goodyer, I. M., Fonagy, P., Jones, P. B., Lindenberger, U., and Dolan, R. J. (2019). Compulsivity and impulsivity traits linked to attenuated developmental frontostriatal myelination trajectories. *Nature Neuroscience*, 22(6):992–999.

Ziener, C. H., Bauer, W. R., and Jakob, P. M. (2005). Transverse relaxation of cells labeled with magnetic nanoparticles. *Magnetic Resonance in Medicine*, 54(3):702–706.

Zikopoulos, B. and Barbas, H. (2010). Changes in prefrontal axons may disrupt the network in autism. *Journal of Neuroscience*, 30(44):14595–14609.

Appendix

Published Papper 1:

Oliveira, R., Pelentritou, A., Di Domenicantonio, G., De Lucia, M., and Lutti, A. (2022). In vivo Estimation of Axonal Morphology From Magnetic Resonance Imaging and Electroencephalography Data. Front. Neurosci. 16, 1–18. doi: 10.3389/fnins.2022.874023

Published Papper 2:

Oliveira, R., Lucia, M. De, and Lutti, A. (2023). Single-subject electroencephalography measurement of interhemispheric transfer time. Hum. Brain Mapp., 1–16. doi: 10.1002/hbm.26420

frontiers | Frontiers in Neuroscience

ORIGINAL RESEARCH
published: 21 April 2022
doi: 10.3389/fnins.2022.874023

In vivo Estimation of Axonal Morphology From Magnetic Resonance Imaging and Electroencephalography Data

Rita Oliveira, Andria Pelentritou, Giulia Di Domenicantonio, Marzia De Lucia and Antoine Lutti**

Laboratory for Research in Neuroimaging, Department of Clinical Neuroscience, Lausanne University Hospital and University of Lausanne, Lausanne, Switzerland

OPEN ACCESS

Edited by:
Andrada Ianus, Champalimaud Foundation, Portugal

Reviewed by:
Maryam Afzali, Cardiff University, United Kingdom
Eirini Messaritaki, Cardiff University, United Kingdom

***Correspondence:**
Rita Oliveira
Ana.Veiga-De-Oliveira@chuv.ch
Antoine Lutti
Antoine.Lutti@chuv.ch

Specialty section:
This article was submitted to Brain Imaging Methods, a section of the journal Frontiers in Neuroscience

Received: *11 February 2022*
Accepted: *24 March 2022*
Published: *21 April 2022*

Citation:
Oliveira R, Pelentritou A, Di Domenicantonio G, De Lucia M and Lutti A (2022) In vivo Estimation of Axonal Morphology From Magnetic Resonance Imaging and Electroencephalography Data. Front. Neurosci. 16:874023. doi: 10.3389/fnins.2022.874023

Purpose: We present a novel approach that allows the estimation of morphological features of axonal fibers from data acquired *in vivo* in humans. This approach allows the assessment of white matter microscopic properties non-invasively with improved specificity.

Theory: The proposed approach is based on a biophysical model of Magnetic Resonance Imaging (MRI) data and of axonal conduction velocity estimates obtained with Electroencephalography (EEG). In a white matter tract of interest, these data depend on (1) the distribution of axonal radius [$P(r)$] and (2) the g-ratio of the individual axons that compose this tract [$g(r)$]. $P(r)$ is assumed to follow a Gamma distribution with mode and scale parameters, M and θ, and $g(r)$ is described by a power law with parameters α and β .

Methods: MRI and EEG data were recorded from 14 healthy volunteers. MRI data were collected with a 3T scanner. MRI-measured g-ratio maps were computed and sampled along the visual transcallosal tract. EEG data were recorded using a 128-lead system with a visual Poffenberg paradigm. The interhemispheric transfer time and axonal conduction velocity were computed from the EEG current density at the group level. Using the MRI and EEG measures and the proposed model, we estimated morphological properties of axons in the visual transcallosal tract.

Results: The estimated interhemispheric transfer time was 11.72 ± 2.87 ms, leading to an average conduction velocity across subjects of 13.22 ± 1.18 m/s. Out of the 4 free parameters of the proposed model, we estimated θ – the width of the right tail of the axonal radius distribution – and β – the scaling factor of the axonal g-ratio, a measure of fiber myelination. Across subjects, the parameter θ was 0.40 ± 0.07 μm and the parameter β was 0.67 ± 0.02 $\mu m^{-\alpha}$.

Conclusion: The estimates of axonal radius and myelination are consistent with histological findings, illustrating the feasibility of this approach. The proposed method allows the measurement of the distribution of axonal radius and myelination within a white matter tract, opening new avenues for the combined study of brain structure and function, and for *in vivo* histological studies of the human brain.

Keywords: MRI, EEG, axonal morphology, IHTT, *in vivo* histology

INTRODUCTION

The characterization of microscopic brain changes *in vivo* in clinical populations is essential to the understanding of brain disease. Magnetic Resonance Imaging (MRI) is non-invasive and the primary technique for the assessment of brain structure *in vivo* (Weiskopf et al., 2015; Kiselev and Novikov, 2018). MRI is sensitive to a large array of microscopic properties of brain tissue such as cell density, fiber radius and directionality, myelin, and iron concentration (Fukunaga et al., 2010; Lutti et al., 2014; Weiskopf et al., 2015; Jelescu et al., 2020). Biophysical models of the relationship between tissue microstructure and the MRI signal allow the assessment of microscopic properties of brain tissue from *in vivo* MRI data ("*in vivo* histology") (Weiskopf et al., 2015; Edwards et al., 2018; Kiselev and Novikov, 2018; Jelescu et al., 2020). Since MRI gives rise to a variety of image contrasts, each contrast being differentially sensitive to multiple microscopic properties of brain tissue, such biophysical models are intrinsically tuned to specific types of MR images (MacKay and Laule, 2016; Does, 2018; Kiselev and Novikov, 2018; Jelescu et al., 2020). Here, we focus on axonal radius and myelination and on the main biophysical models that allow their measurement from *in vivo* data.

Axonal radius is a key property of neurons and is the main determinant of the speed of conduction of action potentials along axonal fibers (Rushton, 1951; Waxman and Bennett, 1972). Axonal radius plays an essential role in neuronal communications and is an instrumental structural underpinning of brain function (Liewald et al., 2014). Axonal radius estimates have been used as measures of functional connectivity in generative models of brain function, e.g., using dynamic causal modeling (Stephan et al., 2009; Honey et al., 2010). Moreover, axonal radius is a biomarker of brain development and healthy aging (Weiskopf et al., 2015) and is of high clinical relevance for a range of disorders such as autism (Wegiel et al., 2018), multiple sclerosis (Evangelou et al., 2001) and motor-neuron disease (Cluskey and Ramsden, 2001). Diffusion contrast is the main type of MRI data used for the measurement of axonal radius *in vivo*. Suitable biophysical models include AxCaliber (Assaf et al., 2008; Barazany et al., 2009), which enables the estimation of the full distribution of axonal radius. ActiveAx is an alternative model that enables the estimation of axonal radius in all white matter tracts without *a priori* knowledge of fiber orientation (Alexander et al., 2010). However, this model provides a single summary index of axonal radius distribution, weighted toward larger axons (Jones et al., 2018; Veraart et al., 2020). Axonal radius estimates obtained *in vivo* from diffusion MRI data are often overestimated compared to histological values (Aboitiz et al., 1992; Liewald et al., 2014) due to the limited gradient strength of MRI scanners and other confounding factors, such as the dominance of the extra-axonal signal (Burcaw et al., 2015; Nilsson et al., 2017; Jones et al., 2018; Lee et al., 2018; Jelescu et al., 2020; Veraart et al., 2020).

Besides axonal radius, axonal fiber myelination is also a crucial factor in the transmission of neuronal information and brain function (MacKay and Laule, 2016). The non-invasive assessment of myelination enables the study of brain plasticity in healthy individuals and brain changes in a range of neurological disorders (Lazari and Lipp, 2021). Relaxometry MRI data are *in vivo* biomarkers of bulk myelin concentration within brain tissue (Lutti et al., 2014; Stüber et al., 2014). While their validity is supported by a large array of empirical evidence, these biomarkers lack an explicit link with the underlying histological properties of brain tissue, consequently hindering the interpretability of results (Weiskopf et al., 2015). Further specificity may be gained from MRI measures of the fraction of water embedded within the myelin sheath (Feintuch et al., 2007; MacKay and Laule, 2016; Does, 2018). Nonetheless, important aspects pertaining to exchange between compartments and suitable MRI acquisition sequences remain unclear (Dortch et al., 2013). Another effort toward improved specificity lies in MRI measures of the g-ratio, the relative thickness of the myelin sheath around axons (Stikov et al., 2011, 2015). MRI-measured g-ratio estimates are aggregate measures of the axonal g-ratio, across all fibers present in each voxel of an MR image (West et al., 2016).

In summary, current MRI markers of axonal radius and fiber myelination are averages across populations of axons present in each voxel of an MR image. To date, estimating the distribution of these morphological features across axonal populations remain largely out of reach. To address this limitation, we propose a novel approach that enables the estimation, from *in vivo* data, of the radius and myelination of axonal fibers, across the distribution of axonal populations in a white matter tract. This approach is based on the combination of electroencephalography (EEG) measures of signal conduction velocity along a white matter tract of interest, and of MRI measures of the g-ratio, sampled along the same tract. MRI and EEG have been jointly used in brain connectivity studies and for the combined study of brain structure and function (Westerhausen et al., 2006; Sui et al., 2014; Helbling et al., 2015; Horowitz et al., 2015; Deslauriers-Gauthier et al., 2019). In particular, the high temporal resolution of EEG allows the estimation of the interhemispheric transfer time (IHTT) (Saron and Davidson, 1989; Marzi, 1999) using the established visual Poffenberger paradigm (Westerhausen et al., 2006; Whitford et al., 2011; Friedrich et al., 2017; Chaumillon et al., 2018). Subsequently, an estimate of axonal conduction

velocity can be computed (Caminiti et al., 2013; Horowitz et al., 2015). The dominant contributions of axonal radius and myelination to conduction velocity (Drakesmith et al., 2019) underline the complementarity of this EEG measure with the MRI measures described above. In the first part of this paper, we present the biophysical model underlying the proposed approach (**Figure 1**). Numerical simulations are then conducted to illustrate the plausibility of our results in light of the histology literature and to assess the variability and accuracy of the morphological estimates. To illustrate the feasibility of the proposed approach, we present estimates of axonal morphology obtained using *in vivo* data from the visual transcallosal white matter tract of healthy volunteers.

THEORY—BIOPHYSICAL MODEL

Axon Morphological Properties

With the proposed model (**Figure 1**), both the MRI and EEG data are described as a function of the distribution of axonal radius [$P(r)$] and of the axonal g-ratio [$g(r)$] within a given white matter tract. The axonal radius distribution is assumed to be a Gamma distribution (Sepehrband et al., 2016):

$$P(r) = P(r|M,\theta) = \frac{1}{\Gamma\left(\frac{M}{\theta}+1\right)\theta^{\frac{M}{\theta}+1}} r^{\frac{M}{\theta}} e^{\frac{-r}{\theta}} \quad (1)$$

where r is the axonal radius. M represents the mode, i.e., the peak of the axonal radius distribution and the parameter θ represents the width of the right tail of the axonal radius distribution, a measure of the number of large axons in a white matter fiber tract.

Histological studies have shown that larger axons exhibit comparatively thinner myelin sheaths, i.e., larger g-ratios (Ikeda and Oka, 2012; Gibson et al., 2014). From data obtained in the peripheral nervous system of the rat, the radius dependence of the g-ratio was shown to follow (Ikeda and Oka, 2012): $g_{REF}(r) = 0.22\ log(2r) + 0.508$. However, to facilitate the mathematical manipulation of the biophysical model (Eqs. 3 and 5 below), we write the radius dependence of the axonal g-ratio as:

$$g(r) = \beta * r^{\alpha} \quad (2)$$

With this power law, the exponent α represents the slope of the radius dependence of the axonal g-ratio, while the parameter β is a scaling factor. Unlike the mathematical expression for g_{REF}, this power law does not include an offset term. To verify its validity, we fitted this power law with the reference relationship (g_{REF}) of Ikeda and Oka (2012). The result shows an excellent level of agreement between both expressions ($R^2 = 0.99$), with $\alpha = 0.18$ and $\beta = 0.57$ (**Figure 2A**). We also verified the applicability of the power law in the human central nervous system, where the higher axonal g-ratio requires the addition of a systematic offset to g_{REF}. We estimated this offset to be 0.14, assuming a g-ratio of 0.7 for an axonal radius of 0.9 μm, based on studies showing g-ratio estimates between 0.65 and 0.79 (Mohammadi et al., 2015; Stikov et al., 2015) across the range of axonal radius observed in the human brain (Aboitiz et al., 1992; Caminiti et al., 2009; Liewald et al., 2014). Fitting of the power law (Eq. 2) with the reference relationship (g_{REF}) after addition of this offset leads to an excellent agreement ($R^2 = 0.99$), with $\alpha = 0.14$ and $\beta = 0.71$ (**Figure 2B**). The latter values will be used when the parameters α and β are set constant to allow for the estimation of other model parameters (see section "Model Parameters").

Modeling of the *in vivo* Data

In agreement with West et al. (2016), the MRI-measured g-ratio is written as an ensemble average of the axonal g-ratios within each image voxel, weighted by the axons' cross-sectional area:

$$g_{MRI}{}^2 = \frac{\int_0^\infty R^2 g(r)^2 P(r) dr}{\int_0^\infty R^2 P(r) dr} = \frac{\int_0^\infty r^2 P(r) dr}{\int_0^\infty \frac{r^2}{g(r)^2} P(r) dr} \quad (3)$$

where R is the fiber radius [$R = r/g(r)$]. From Eqs. (1) and (2), Eq. (3) becomes (see **Supplementary Appendix A**):

$$g_{MRI}{}^2 = \beta^2 \theta^{2\alpha} * \frac{\Gamma\left(\frac{M}{\theta}+1\right)}{\Gamma\left(\frac{M}{\theta}+1-2\alpha\right)} * \frac{M+3\theta+2\frac{\theta^2}{M}}{M+(3-4\alpha)\theta+\left(2+4\alpha^2-6\alpha\right)\frac{\theta^2}{M}} \quad (4)$$

As described in Waxman and Bennett (1972), axonal conduction velocity (v) can be derived from the morphological properties of axons using: $v\ [m/s] = p\ \frac{d\ [\mu m]}{g}$, where p (∼5.5–6.0) represents the contribution of additional axonal factors to the propagation of action potentials (e.g., length of Ranvier nodes, electrical properties of the myelin membranes). Assuming an equal contribution from all axons to the conduction velocity V measured with EEG, we obtain:

$$V = 5.5 \int_0^\infty \frac{2r\ P(r)}{g(r)}\ dr \quad (5)$$

From Eqs. (1) and (2), Eq. (5) becomes (see **Supplementary Appendix A**):

$$V = \frac{11\theta^{1-\alpha}}{\beta} \frac{\Gamma\left(\frac{M}{\theta}+1-\alpha\right)}{\Gamma\left(\frac{M}{\theta}+1\right)} \left(\frac{M}{\theta} + 1 - \alpha\right) \quad (6)$$

Model Parameters

The proposed model (Eqs. 4 and 6) includes 4 free parameters, pertaining to the distribution of axonal radius (M and θ) and to the radius-dependent axonal g-ratio (α and β). However, our proposed model uses only two data types acquired *in vivo* (MRI-measured g-ratio and EEG-based axonal conduction velocity). It is therefore necessary to set two parameters to reference values.

In general terms, the choice of model parameters to estimate should take into consideration the neural mechanisms underlying each application study of this model. The exponent α of the power law $g(r)$ represents the rate of change in thickness of the myelin sheath with axonal radius and may be a parameter of interest when considering changes in neuronal shape that differentially affect axons of different sizes. In contrast, the scale parameter β equally affects axons of all sizes. Concerning the distribution of axonal radius, we highlight that histological studies across white matter tracts and animal species have reported that, for reasons pertaining to brain size limitations and metabolism, the mode M of the axonal radius distribution remains largely constant (Tomasi et al., 2012; Liewald et al., 2014). This motivates setting M to a constant value from the

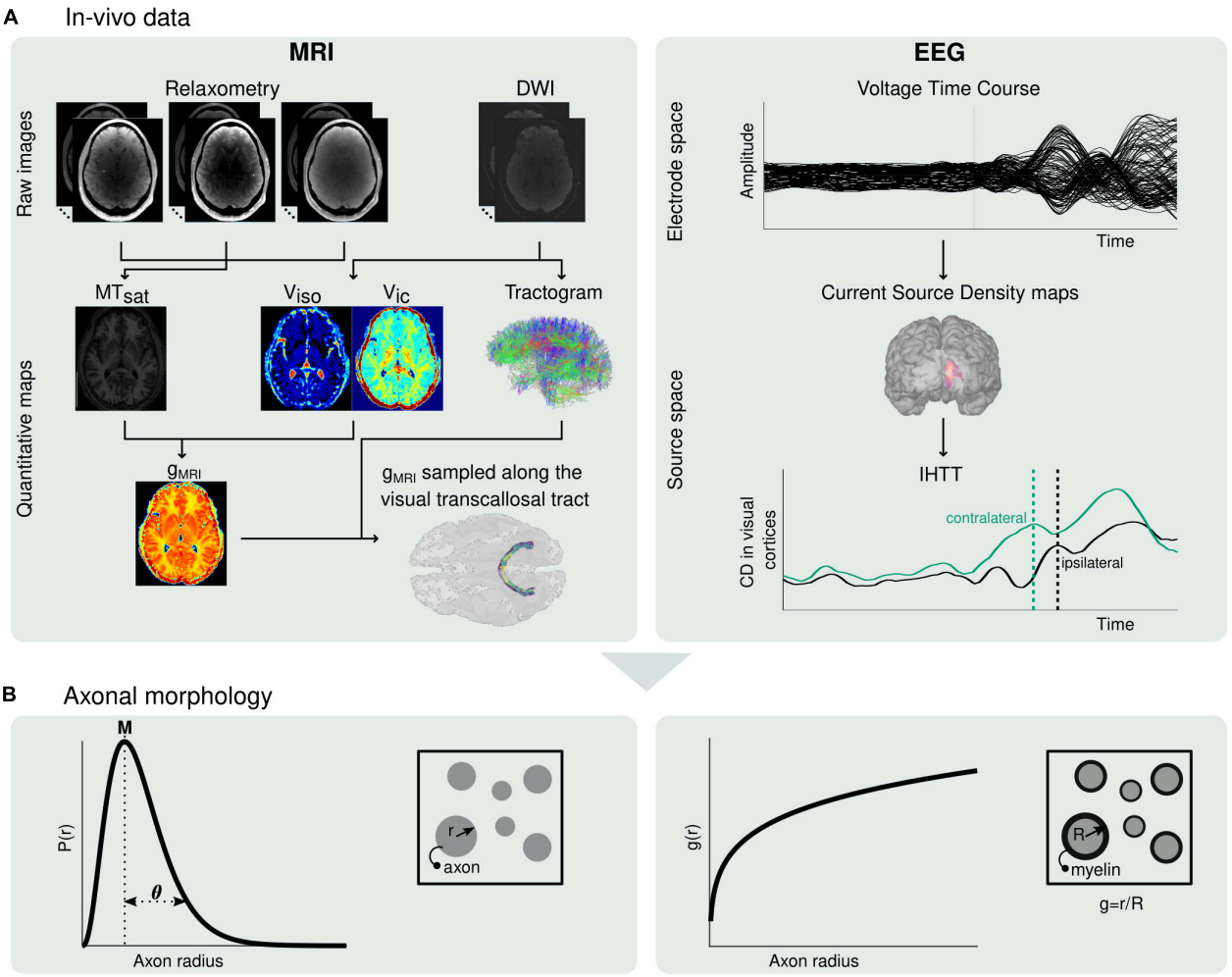

FIGURE 1 | Estimation of microscopic morphological properties of axons from *in vivo* MRI and EEG data. **(A)** Maps of MT_{sat}, v_{iso} and v_{ic} are computed from the raw MRI data and subsequently used to compute maps of the MRI-measured g-ratio (g_{MRI}) (left). The MRI-measured g-ratio maps are sampled along the visual transcallosal tract using the streamlines obtained with diffusion MRI tractography. Estimation of the IHTT is performed after source reconstruction of the EEG data, based on the difference in latency between the two maxima of activation at the two hemispheres observed on the group-averaged current source time course (right). **(B)** The g_{MRI} and IHTT estimates are used to estimate morphological properties of axons within the visual transcallosal tract axonal radius distribution [$P(r)$, left] and axonal g-ratio [$g(r)$, right].

histological literature and estimating the tail parameter θ from the *in vivo* data.

The choice of constant model parameters may also be guided by the impact of inaccurate constant values on the estimated morphological features. The bias of the parameter estimates arising from inaccuracies of 10% in α, M or β was evaluated using numerical simulations (with the procedure described in methods section "Estimation of Axonal Morphology From *in vivo* Data"). Across a range of plausible g_{MRI} and V, an inaccuracy of 10% in α leads to an average bias of ∼10 and ∼15% on the estimated M and θ, respectively (**Supplementary Figure 1A**). Similarly, an inaccuracy of 10% in M leads to an average bias of ∼1 and ∼22% for β and θ, respectively (**Supplementary Figure 1B**). However, an inaccuracy of 10% in β leads to an average bias of ∼155% and ∼92% for M and θ, respectively (**Supplementary Figure 1C**).

From the biological and numerical considerations above, in this study, we chose to set α to 0.14 (see section "Axon Morphological Properties") and M to 0.40 μm (Tomasi et al., 2012; Liewald et al., 2014) and to estimate the parameters β and θ.

MATERIALS AND METHODS

Numerical Simulations

Numerical simulations were conducted using Eqs. (4) and (6), to examine the values of the model parameters (M, θ, α, and β) obtained from combinations of the *in vivo* data (g_{MRI} and V) using the procedure described in methods section "Estimation of Axon Morphology From *in vivo* Data", and vice versa.

In order to highlight the range of *in vivo* data values compatible with the proposed model, estimates of M and θ were

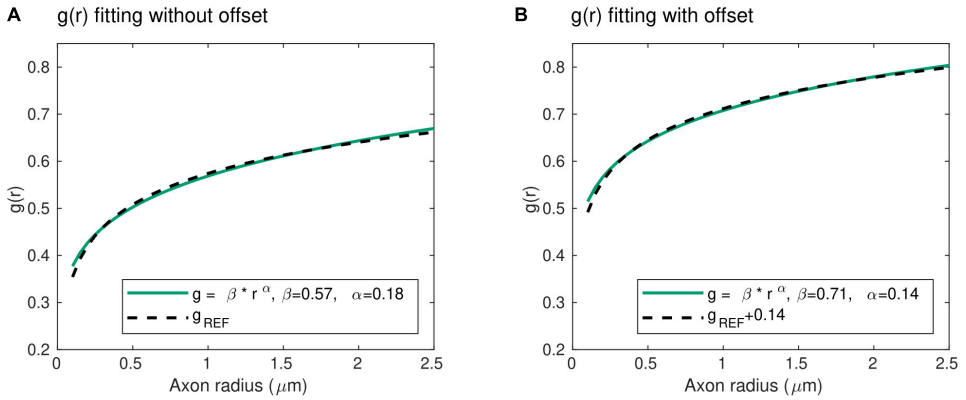

FIGURE 2 | Radius dependence of the g-ratio. **(A)** An excellent agreement (R^2 = 0.99) is found between the proposed power law (green line) and reference histological measures of the g-ratio [g_{REF} (Ikeda and Oka, 2012), dashed line], with $\alpha = 0.18$ and $\beta = 0.57\ \mu m^{-\alpha}$. **(B)** The higher axonal g-ratios in the human central nervous system were accounted for by adding an offset of 0.14 to the reference peripherical nervous system data. The agreement between the proposed power law and the reference g_{REF} remains very high (R^2 = 0.99), with $\alpha = 0.14$ and $\beta = 0.71\ \mu m^{-\alpha}$.

computed across a large range of g_{MRI} and V values, setting $\alpha = 0.14$ and $\beta = 0.71$ (section "Axon Morphological Properties"). The range of *in vivo* data values compatible with the proposed model was determined by comparison of the M and θ estimates against reference literature values.

Subsequent numerical simulations were conducted by estimating the parameters β and θ across the range of compatible *in vivo* data values, setting $\alpha = 0.14$ and M to 0.40 μm (section "Model Parameters"). In particular, we examined the range of the parameters β and θ across values of g_{MRI} and V reported in the literature.

The variability of the model parameter estimates in the presence of noise was also investigated. Simulated estimates of the *in vivo* data g_{MRI} and V were computed from combinations of θ and β values using Eqs. (4) and (6). Noise was added to the computed g_{MRI} and V values with a standard deviation of 0.03 for g_{MRI} and 0.50 m/s for V, representative of intra-subject variability in *in vivo* data. To replicate *in vivo* conditions, 700 samples of g_{MRI} and one sample of V were taken from the resulting distributions of g_{MRI} and V, and estimates of θ and β from noisy data were calculated. This process was repeated 2,000 times and the standard deviation of the θ and β estimates across repetitions was computed as a measure of their variability.

Finally, we set out to investigate the effect of using a group averaged conduction velocity rather than subject-specific velocities. We selected 15 samples of g_{MRI} and V values from distributions with means of 0.70 and 10 m/s and standard deviations of 0.05 and 0.80 m/s, respectively, representative of inter-subject variability in *in vivo* data. From these simulated *in vivo* data, reference values of β and θ were calculated. Estimates of β and θ were also computed from the average of the 15 samples of V. We then estimated the bias between the reference β and θ values and those obtained from the average value of V.

In vivo Data

We acquired data from 17 right-handed healthy volunteers. All participants had normal or corrected-to-normal vision and hearing and had no history of psychiatric or neurological disorders. Participant handedness was evaluated with the Edinburgh Handedness Inventory (Oldfield, 1971). All participants gave written informed consent and received 80 Swiss Francs as monetary compensation. The study was approved by the local ethics committee.

MRI data quality was assessed using the Motion Degradation Index (MDI) described in Castella et al. (2018) and Lutti et al. (2022). MDI values were $\lesssim 4\ s^{-1}$ for the PD- and T1-weighted raw images, and $\lesssim 5\ s^{-1}$ MT-weighted raw images, indicative of good quality images (Lutti et al., 2022; see **Supplementary Figure 2**). Three participants were excluded due to artifacted EEG recordings. The final sample consisted of 14 participants (6 females; age = 27.14 ± 3.86 years). Three participants had left eye dominance, as determined by the eye viewing an object at a distance when the participant looks through a small opening (Miles, 1930). An overview of the data processing pipeline of the *in vivo* data is shown in **Figure 1A**.

Magnetic Resonance Imaging-Based Estimation of the G-Ratio

MRI data were collected on a whole-body 3T MRI system (Magnetom Prisma; Siemens Medical Systems, Erlangen, Germany) using a 64-channel receive head coil at the Laboratory for Neuroimaging Research, Lausanne University Hospital.

Structural Magnetic Resonance Imaging Acquisition

A 3D structural T1-weighted Magnetization-Prepared Rapid Gradient-Echo (MPRAGE) image was acquired with a 1 mm^3 isotropic voxel size and a matrix size of 176 × 232 × 256. TR/TE = 2,000/2.39 ms. TI/α = 920 ms/9°. Parallel imaging (acceleration factor 2, GRAPPA reconstruction) was used along the phase-encoding direction (Griswold et al., 2002). The total acquisition time was 4 min.

Relaxometry Magnetic Resonance Imaging Acquisition

The relaxometry MRI protocol consisted of multi-echo 3D fast low angle shot (FLASH) acquisitions with magnetization

transfer-weighted (TR/α = 24.5 ms/6°, 6 echos), proton density-weighted (TR/α = 24.5 ms/6°, 8 echos) and T1-weighted (TR/α = 24.5 ms/21°, 8 echos) (Melie-Garcia et al., 2018) image contrasts (**Figure 1A**). The echo spacing and minimal echo time were both 2.34 ms. The MR images had a 1 mm^3 isotropic voxel size. Parallel imaging (acceleration factor 2, GRAPPA reconstruction) was used along the phase-encoding direction (Griswold et al., 2002) and Partial Fourier (acceleration factor 6/8) was used along the partition direction. B1-field mapping data was acquired to correct for RF transmit field inhomogeneities (Lutti et al., 2010, 2012): 4 mm^3 voxel size, TR/TE = 500/39.1 ms. B0-field mapping data was acquired to correct for image distortions in the B1 mapping data: 2D double-echo FLASH, TR/ α = 1,020 ms/90°, TE1/TE2 = 10/12.46 ms, BW = 260 Hz/pixel, slice thickness = 2 mm. The total acquisition time was 27 min.

Diffusion-Weighted Imaging

Diffusion-weighted imaging (DWI) data were acquired using a 2D echo-planar imaging sequence (TR/TE = 7,420/69 ms) along 15, 30, and 60 diffusion directions with b = 650/1,000/2,000 s/mm^2, respectively (**Figure 1A**). 13 images with $b = 0$ were acquired, interleaved throughout the acquisition (Slater et al., 2019), making a total of 118 isotropically distributed directions. Images had a 2 mm^2 isotropic voxel size and a matrix size of 96 × 106, with 70 axial slices. Parallel imaging was used along the phase-encoding direction (acceleration factor 2, GRAPPA reconstruction). The total acquisition time was 15 min.

Estimation of Magnetic Resonance Imaging Quantitative Maps

Maps of Magnetization Transfer (MT_{sat}) were computed from the raw FLASH images as in Helms et al. (2008a,b) (**Figure 1A**). The map computation was conducted using the hMRI toolbox (Tabelow et al., 2019) and included corrections for local RF transmit field inhomogeneities (Helms et al., 2008a) and for imperfect RF spoiling (Preibisch and Deichmann, 2009).

DWI data were corrected for geometrical distortions, using *eddy* from FMRIB's Diffusion Toolbox (Andersson and Sotiropoulos, 2016), and for echo-planar imaging susceptibility distortions using the SPM12 fieldmap toolbox (Hutton et al., 2002). DWI images were aligned to the MT_{sat} map using SPM12 and a rigid body transformation. Finally, maps of the isotropic diffusion (v_{iso}) and intracellular (v_{ic}) compartments volume fractions were computed from the DWI data using the NODDI model (Zhang et al., 2012) and the AMICO toolbox (Daducci et al., 2015; **Figure 1A**).

Maps of the MRI-measured g-ratio were estimated from: $g_{MRI} = \sqrt{1/(1 + MVF/AVF)}$, where MVF and AVF are the myelin and the axonal volume fractions, respectively (Stikov et al., 2015; **Figure 1A**). The MVF maps were estimated from the MT_{sat} maps according to: $MVF = \alpha MT_{sat}$, where the calibration factor α was set by assuming a median g_{MRI} value of 0.70 in the splenium of the CC of 11 subjects of a separate cohort ($\alpha = 0.23$) (Campbell et al., 2018; Slater et al., 2019). The AVF maps were estimated as: $AVF = (1 - \alpha MT_{sat})\ (1 - v_{iso})v_{ic}$ (Stikov et al., 2015).

The Freesurfer 6.0 software (Schiffler et al., 2017) was used to delineate each subject's Brodmann areas 17 and 18 (Fischl et al., 2008) from their MPRAGE image, corresponding to the primary (V1) and secondary (V2) visual cortical areas, respectively. These regions of interest (ROIs), henceforth called "V1V2", were grouped and registered to the diffusion data using FMRIB's Linear Image Registration Tool (Jenkinson and Smith, 2001).

Tractography analysis was conducted using the mrTrix software (Tournier et al., 2019): whole-brain anatomically constrained tractography was performed using the iFOD2 algorithm, with dynamic seeding to improve the distribution of reconstructed streamlines density, a maximum of 45° between successive steps, a cut-off of 0.05 in the fiber orientation distribution amplitude, backtrack and streamlines cropping in the gray-white matter interface. A total of 20 million streamlines between 5 and 250 mm in length were selected and submitted to SIFT2 to penalize streamlines with a reduced agreement with diffusion data. The visual transcallosal tract was isolated by selecting the streamlines connecting the V1V2 ROIs in each hemisphere across the CC. This tract was used to extract samples from the MRI-measured g-ratio maps (**Figure 1A**).

Electroencephalography-Based Estimation of the Interhemispheric Transfer Time

Experimental Paradigm

We implemented the visual Poffenberger paradigm on a 61 cm widescreen (60 Hz refreshing rate), in line with the literature (Westerhausen et al., 2006; Whitford et al., 2011; Friedrich et al., 2017; Chaumillon et al., 2018). The experiment was administered using Psychtoolbox-3.0.16 in MATLAB (R2019b, The Mathworks, Natick, MA). Participants were comfortably seated on a chair in a dimly lit room, at a standardized distance of 80 cm from the screen, thus 1 cm on the screen represented 0.72° of the visual angle. Each trial consisted of the presentation of a black and white circular checkerboard with a pattern reversal of 15 Hz on a gray background (20 cd/m^2) and with a duration of 100 ms. The stimuli were of 4° diameter and their outer edge appeared at 6° horizontal and 6° vertical distance from the centrally-located fixation cross (0.8° size) to the lower left or right visual hemifield. The acquisition was structured in 6 blocks with an approximate duration of 6 min each; a short break was allowed between each experimental block. Each block consisted of 205 trials (95 for right visual field, 95 for left visual field, and 15 where no stimulus appeared), presented in a pseudorandom order and with inter-trial intervals randomly assigned between 1.0 and 2.0 s. Participants were instructed to avoid unnecessary movements and to press a button as quickly as possible after the appearance of a stimulus while keeping their gaze on the fixation cross. Responses were given with the index finger via a keyboard button press placed centrally to the subject's body. The administered blocks alternated between left and right-hand index finger button presses (three blocks per hand).

Electroencephalography Data Acquisition

Continuous 128-channel EEG was recorded using the Micromed recording system (Micromed SystemPlus Evolution, Mogliano

Veneto, Italy) and an Ag/AgCl electrode cap (waveguard^{TM} original, ANT Neuro, Hengelo, Netherlands) at a sampling rate of 1,024 Hz with FPz as the reference electrode and AFFz as the ground electrode. Two additional horizontal EOG electrodes were attached to the outer canthi of each eye. Electrode impedance was kept below 20 kΩ. Electrode positions and head shape were acquired for each participant using the xensor^{TM} digitizer (ANT Neuro, Hengelo, Netherlands).

Electroencephalography Data Analysis

EEG data analysis utilized custom-made MATLAB (R2021a, The Mathworks, Natick, MA) scripts and open-source toolboxes Fieldtrip (version 20191206, Oostenveld et al., 2011), EEGLAB (version 13.4.4b, Delorme and Makeig, 2004), and Brainstorm (Tadel et al., 2011). Continuous raw EEG was bandpass-filtered between 0.1 and 40 Hz (digital filters). EEG epochs were extracted from the filtered data ranging from -100 to 300 ms relative to visual stimulus onset. Artifact trials were removed based first, on visual inspection. Next, we identified and removed components containing eye movement related artifacts by running an Independent Component Analysis based on the *runica* algorithm (Bell and Sejnowski, 1995). Epochs containing additional artifacts were identified based on a threshold of 80 μV and excluded from further analysis. Across participants, an average of 20.5% (SD: 10.1%, range: 43–220 trials) and 21.3% (SD: 11.0%, range: 42–206 trials) of the trials were rejected for the left and right visual field stimulation, respectively. Artifact electrodes were identified based on a threshold of 80 μV and were interpolated using the nearest neighbors. On average, 5.9% of electrodes (SD: 2.4%, range 3–14 electrodes) were interpolated across participants. Epoched data were re-referenced to the average reference. We removed DC drift by subtracting the average within each epoch.

Source reconstruction was performed to identify the neural origins underlying the visual evoked response to the left and right hemifield visual stimuli (**Figure 1A**). Virtual sensors from artifact-free EEG data were calculated using the minimum-norm current density method (Hämäläinen and Ilmoniemi, 1994) as implemented in Brainstorm. The MRI image of each subject was registered to the electrode positions using an iterative algorithm that finds the best fit between the head shape obtained using the MRI data and that obtained via EEG digitization. Surface reconstructions were obtained using a 3-layer Boundary Element Method (Kybic et al., 2005; Gramfort et al., 2010) model on each subject's MRI image. The source grid was defined with 15,000 points on the gray matter. This way, we estimated the current densities (CD, pA.m) for each condition, source, and time point within each subject. The CDs were extracted for the V1V2 ROI defined in section "MRI-Based Estimation of the G-Ratio" — for the left and right brain hemisphere — for each trial and each subject. Next, V1V2 ROI CDs were averaged across trials within each subject. Given that cortical anatomies vary considerably across participants due to the folding patterns of each individual, current source density maps have ambiguous signs on the group level. Consequently, we took the absolute value of the CDs of each subject before computing a group average.

Estimation of the Interhemispheric Transfer Time and Conduction Velocity

We assumed that lateralized visual stimuli would induce first, a contralateral activation of the visual cortex, followed by an activation of the ipsilateral cortex. This visual information transfer is assumed to be achieved through the CC (Marzi, 1999).

For the IHTT estimation, we identified the first peaks of activation in each hemisphere based on the maximum of the average current density value at the group level (**Figure 1A**). IHTT was calculated as the latency difference between the ipsilateral and contralateral activation peaks on the group average CDs within the V1V2 ROI. A Wilcoxon signed-rank test ($p < 0.05$; *signrank*, in MATLAB) comparing the CDs across participants at these two maxima to the time-average baseline values was used to evaluate the significance of these activations as evoked activity in response to the visual stimuli.

To obtain a confidence interval on the computed IHTT, we subdivided the artifact-free EEG trials available for each participant into four non-overlapping splits. We then repeated four times the CD estimation at group-level where each subject contributed with data coming from one of the split in order to obtain four independent estimations of the IHTT. This allowed us to obtain a standard deviation on the IHTT estimation, which we used to define a confidence interval on the IHTT estimation: *[IHTT-standard deviation; IHTT+standard deviation]*.

Of note, we assumed that the right eye dominance of the majority of the included participants elicited a more reliable estimation of the evoked activity following the left visual stimuli in comparison to the right. For this reason, here, we used the IHTT estimation following the left hemifield visual stimuli.

At the individual level, we extracted the visual transcallosal tract length as the tractography-based mean streamline length. V was calculated by dividing the tract length by the IHTT.

Estimation of Axonal Morphology From *in vivo* Data

Estimation of axonal morphological features from the *in vivo* MRI and EEG data was implemented using MATLAB-based custom-made analysis scripts. The MRI-measured g-ratio samples along the visual transcallosal tract and the estimate of the IHTT were used to estimate model parameter values using Eqs. (4) and (6) (see section "Axon Morphological Properties", **Figure 1B**). This was achieved using MATLAB's non-linear least-square routine (*lsqnonl*) with a trust-region-reflective minimization, which minimizes the sum of the squares of the residuals. The initial conditions used to ensure convergence of the fitting routine were set to $\beta = 0.70\ \mu m^{-\alpha}$ and $\theta = 0.10\ \mu$m.

All codes are available on our online repository: https://github.com/LREN-physics/AxonalMorphology.

RESULTS

Numerical Simulations

We investigated the range of *in vivo* data compatible with the proposed model by considering the values of the model

parameters M and θ computed from each combination of g_{MRI} and V (**Figure 3**). Combinations of large values of g_{MRI} and low values of V lead to unrealistically low values of M ($\sim 10^{-14}$ μm). Conversely, small values of g_{MRI} and large values of V lead to excessively large values of M (∼1 μm) and low values of θ (∼0.001 μm) (Aboitiz et al., 1992; Caminiti et al., 2009, 2013; Tomasi et al., 2012; Liewald et al., 2014).

Figure 4 shows the range of the model parameters θ and β across a large range of g_{MRI} and V values. According to the literature, frontal transcallosal white matter exhibits MRI-measured g-ratio values of ∼0.62 (Mohammadi et al., 2015; Slater et al., 2019) and conduction velocities of ∼8 m/s (Caminiti et al., 2013; see red cross in **Figure 4A**). The proposed model yields θ ∼0.05 μm for such combination of g_{MRI} and V, equivalent to a mean axonal radius of 0.45 μm (**Figure 4B**). This value is consistent with histological analyses of such white matter fibers, with a narrow range of axonal radius (mean∼0.48 μm; Caminiti et al., 2009). For visual transcallosal white matter (MRI-measured g-ratio ∼0.72; conduction velocity ∼10 m/s; Caminiti et al., 2013; Mohammadi et al., 2015; Slater et al., 2019), the proposed model yields θ ∼0.23μm (see black cross in **Figure 4A**), leading to a mean axonal radius of ∼0.63 μm (**Figure 4B**). This value is also consistent with histological analyses of such white matter fibers, with a broad range of axonal radius (mean∼0.62 μm; Caminiti et al., 2009). For both types of white matter tracts, fibers with a radius above 1.5 μm represent less than 4% of the total number of fibers, consistently with previous histological studies (Aboitiz et al., 1992; Caminiti et al., 2009; Liewald et al., 2014). The value of the model parameter β for frontal and visual transcallosal white matter were 0.68 and 0.73 $\mu m^{-\alpha}$, respectively (**Figures 4C,D**), in line with histological analyses of the axonal g-ratio in the genu and splenium of the CC (Stikov et al., 2015).

Figure 5 shows the variability of the θ and β estimates in the presence of noise in the *in vivo* data, computed from combinations of conduction velocity and MRI-measured g-ratio across a plausible range with 700 g_{MRI} samples and one V sample. The highest errors in θ (∼35%) are found for the smallest values of θ, with only a small effect of the parameter β. The highest errors in β (∼1%) are obtained from a combination of small values of θ and large values of β. **Supplementary Figure 3** shows the dependence of the variability of the θ and β estimates on the number of samples of V and g_{MRI} ($\beta = 0.71\ \mu m^{-\alpha}$ and $\theta = 0.22$ μm). With only one estimate of V, as was the case in this study, errors of up to 11% on the θ estimates are observed. The errors on the β estimates are mostly driven by the number of g_{MRI} samples included in the estimation: for 100 g_{MRI} samples or more, these errors are below 1% regardless of the number of V samples.

Figure 6 shows the bias in the θ and β estimates arising from an estimation of conduction velocity from a cohort of participants. The bias in θ and β is on average 12 and 0.90% across participants, reaching up to 40 and 3%, respectively.

Estimation of the Interhemispheric Transfer Time and Conduction Velocity

At the sensor level, the group-averaged visual evoked response revealed a positive peak activation, between 115 and 134 ms post-stimulus onset, contralaterally to the stimulus presentation (**Figure 7**, top). The latency of this positive activation corresponds to the expected latency of the P100 component (Di Russo et al., 2001) and was followed by asymmetrically distributed voltage topographies with maximal voltage values at posterior sites at latencies starting at approximately 153 ms post-stimulus onset (**Figure 7**, bottom). After approximately 180 ms, post-stimulus onset voltage topographies showed an ipsilateral positivity to the stimulus presentation, suggesting that the P100 activation has traveled to the opposite hemisphere.

Qualitative observations at the electrode-level were confirmed by the source reconstruction results. Group-averaged absolute CD exhibited a sharp increase at approximately 100 ms post-stimulus onset in the right hemisphere compared to the baseline, peaking at 141 ms (**Figure 8B** for an overview of the spatial

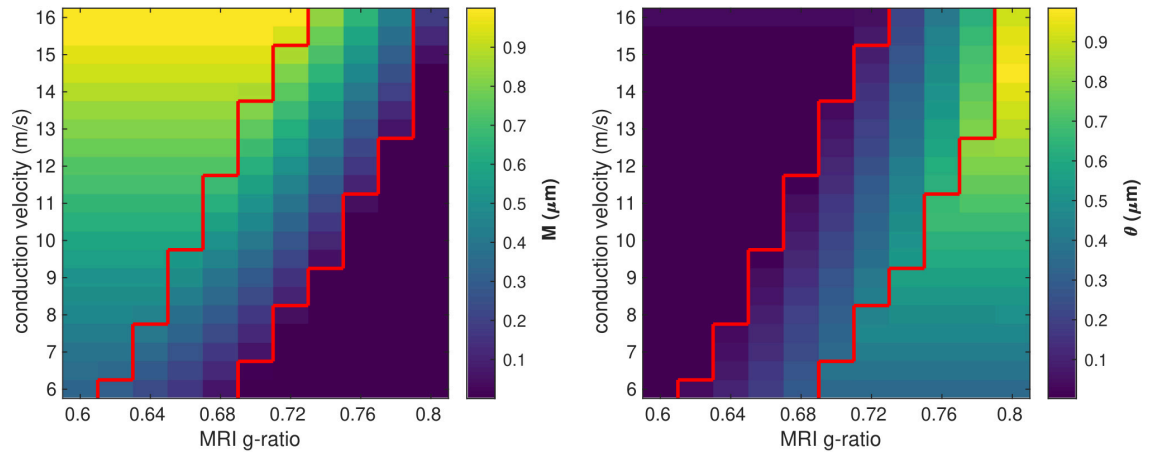

FIGURE 3 | Range of *in vivo* data compatible with the proposed model. Combinations of g_{MRI} and V that lead to biologically plausible values of the model parameters ($0.05 < M < 0.9$ μm and $0.01 < \theta < 0.9$ μm) are located between the two red contour lines.

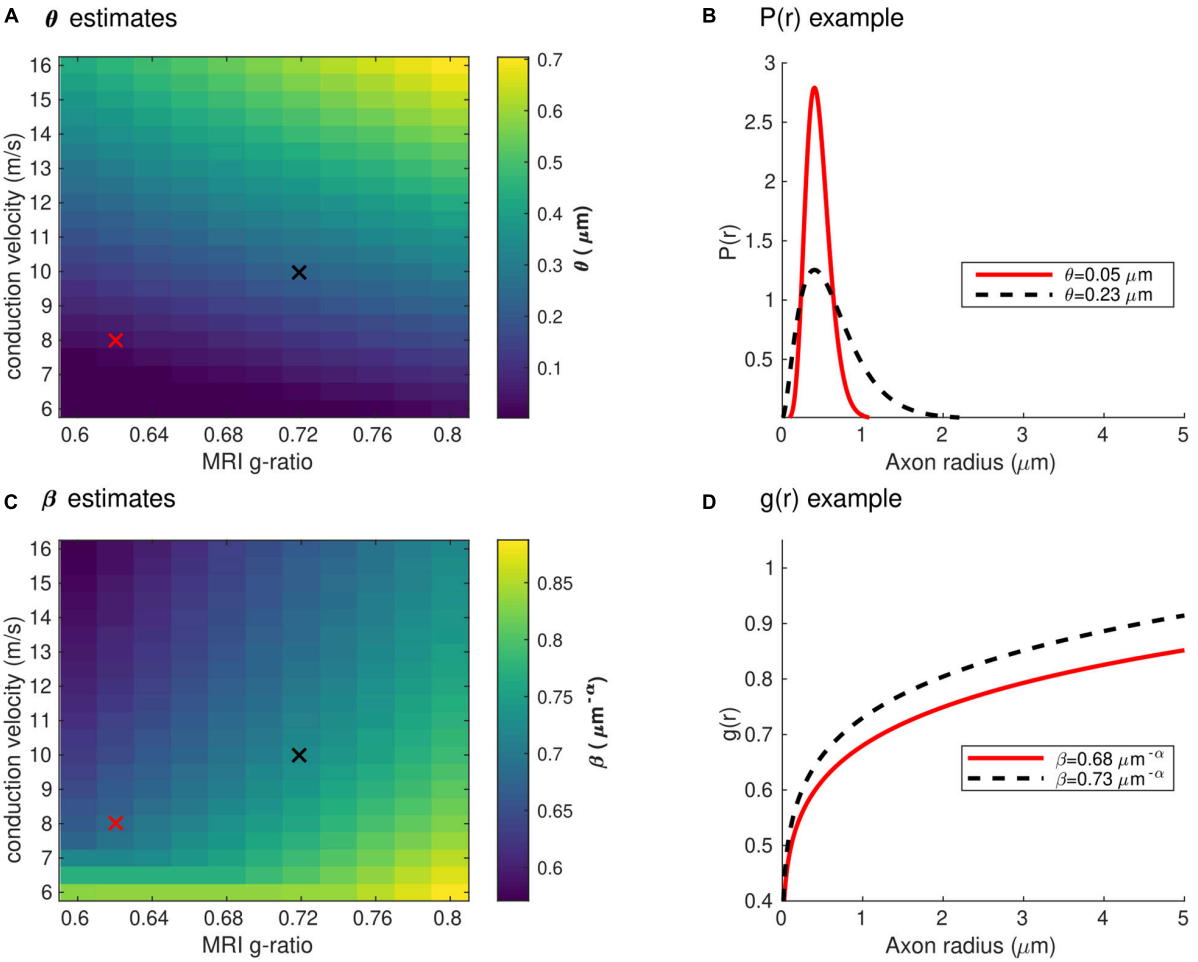

FIGURE 4 | Range of the model parameters θ and β. **(A)** Range of the model parameter θ, computed from combinations of simulated *in vivo* g_{MRI} and V. **(B)** Axonal radius distributions representative of frontal and visual transcallosal white matter (θ = 0.05 and 0.23 μm). **(C)** Range of the model parameter β, computed from combinations of simulated *in vivo* g_{MRI} and V. **(D)** Dependence of the fiber g-ratio on the axonal radius, representative of frontal and visual transcallosal white matter (β = 0.68 and 0.73 $\mu m^{-\alpha}$). In **(A,C)**, the red and black crosses illustrate values of g_{MRI} and V for frontal and visual transcallosal tracts, taken from the literature (Caminiti et al., 2013; Mohammadi et al., 2015; Slater et al., 2019).

distribution of the CD for an exemplar subject). The group-averaged absolute CD on the left visual hemisphere followed the right visual hemisphere, peaking later on at 152 ms.

The IHTT group estimation yielded a value of 11.72 ms with a standard deviation of 2.87 ms. The identified peaks were statistically significantly larger upon visual stimulation when compared to the baseline with p-values of $p < 0.01$.

Using the estimated group IHTT, we calculated the conduction velocity for the visual transcallosal tract using each participant's tract length. The average conduction velocity was 13.22 ± 1.18 m/s across participants (**Table 1**).

Estimation of Axonal Morphology From *in vivo* Data

Estimates of the model parameters θ and β were computed using the proposed model, from the *in vivo* samples of the MRI-measured g-ratio along the visual transcallosal tract and estimates of conduction velocity (**Table 1**). The average value of θ was 0.40 ± 0.07 μm across all subjects and ranged between 0.31 and 0.54 μm (**Figure 9A**). A θ value of 0.40 μm is equivalent to a mean axonal radius of 0.80 μm, inline with previous estimates from histological studies (0.62 μm; Caminiti et al., 2009). For such a value of θ, axons with a radius above 2 μm represent only < 5% of the total fiber count, in agreement with histological studies that show that axonal radius does not exceed ∼1.5–3 μm in the human brain (Aboitiz et al., 1992; Caminiti et al., 2009; Liewald et al., 2014). The average value of β was 0.67 ± 0.02 $\mu m^{-\alpha}$ across all subjects, and ranged between 0.64 and 0.70 $\mu m^{-\alpha}$ (**Figure 9B**). **Figure 9C** shows the axonal radius distribution $P(r)$ for a representative subject (θ = 0.43 μm), with a confidence interval of 0.27–0.69 μm obtained from the IHTT estimation. The estimated value of β for this subject was 0.68 $\mu m^{-\alpha}$, with a confidence interval between 0.64 and 0.71 $\mu m^{-\alpha}$ (**Figure 9D**).

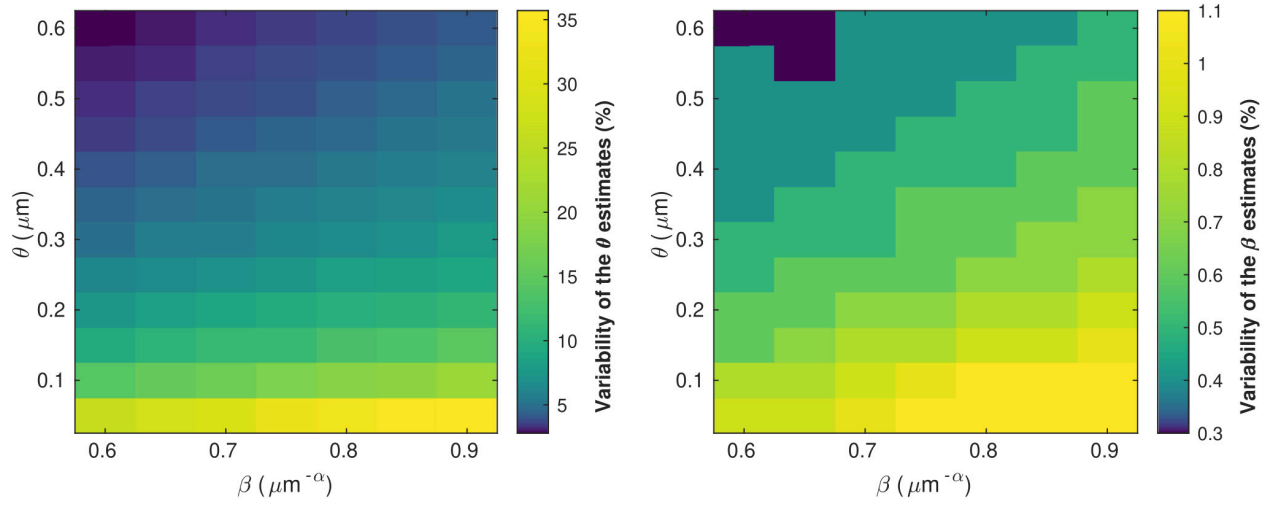

FIGURE 5 | Variability of the θ (left) and β (right) parameter estimates due to noise in the *in vivo* samples of g_{MRI} and V. The highest errors in θ (∼35%) are found for the smallest values of θ, with only a small effect of the parameter β. The highest errors in β (∼1%) are obtained from a combination of small values of θ and large values of β.

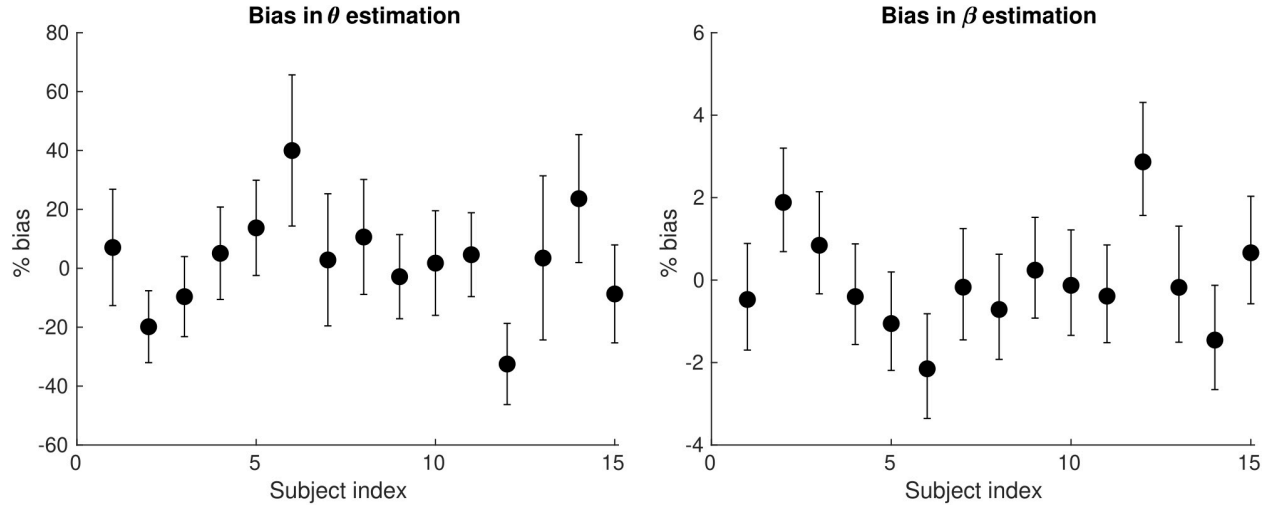

FIGURE 6 | Bias of the θ (left) and the β (right) parameter estimates arising from the computation of axonal conduction velocity across a group of subjects (N = 15). The error bars indicate the standard deviation on the parameter estimates. The bias of θ and β reaches up to 40 and 3%, respectively.

DISCUSSION

In this paper, we propose a novel method that allows the non-invasive estimation of morphological properties of white matter axons from *in vivo* human data. This approach requires MRI-measured g-ratio and EEG-based measures of axonal conduction velocity computed from estimates of the IHTT. From these measures, we estimated the axonal radius and myelination of axonal fibers, distinct histological features of white matter. These morphological features were assessed across the distribution of axons in the visual transcallosal tract, providing a detailed insight into the microscopic properties of these white matter fibers.

Estimation of Axonal Morphology From *in vivo* Data

The proposed model is based on an explicit link between the data acquired *in vivo* and a limited set of histological properties of white matter axons. The MRI-measured g-ratio is expressed as a function of the axonal radius distribution [$P(r)$] and the g-ratio of axonal fibers [$g(r)$], inline with recent studies conducted using MRI and histology data (Stikov et al., 2011, 2015; West et al., 2016). Similarly, axonal conduction velocity — computed from the IHTT estimates — is an ensemble average across the same distribution $P(r)$, assuming an equal contribution of all axons to the EEG data. As a result, both types of *in vivo* data depend on the same properties of axonal fibers: $P(r)$ and $g(r)$. This

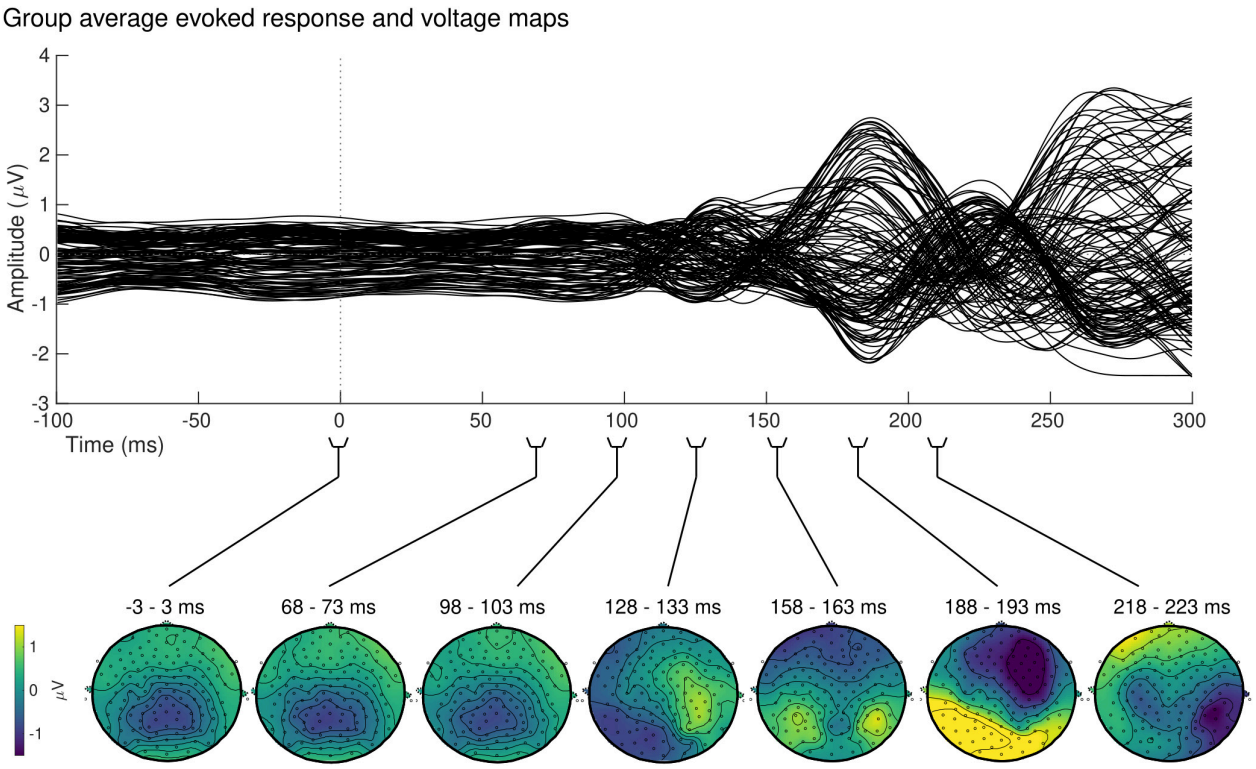

FIGURE 7 | Group sensor space results. Grand-average evoked response (top) and corresponding voltage topographic maps (bottom) after left visual field stimulation. Topographic maps are shown on a flattened electrode layout with anterior regions at the top and posterior regions at the bottom. Time 0 ms identifies the onset of the stimulus presentation. Positive amplitudes (yellow) were observed in the hemisphere contralateral to the stimulus presentation between 115 and 134 ms, followed by a bilateral positivity starting at approximately 153 ms.

approach is supported by recent findings which show that from the numerous histological determinants of conduction velocity (e.g., axonal radius, g-ratio, the conductance of ion channels, diameter and length of Ranvier nodes and internodes), the properties of axons that bring the largest contribution to the determination of conduction velocity are measurable with MRI (Drakesmith et al., 2019).

The mathematical definitions of $P(r)$ and $g(r)$ are grounded on well-established histological findings. $P(r)$ is assumed to follow a gamma distribution, as commonly posited by models of axonal radius distribution (Assaf et al., 2008; Sepehrband et al., 2016). $g(r)$, expressed using a power law, shows a high level of agreement with histological studies (Ikeda and Oka, 2012; Gibson et al., 2014; **Figure 2**). Besides supporting the proposed model, the histological basis for the expressions of $P(r)$ and $g(r)$ allows freedom in the choice of the model parameters estimated from the data, because they reflect different properties of axon populations that can be set constant or variable according to their relevance in a neuroscience application of this model.

From the set of 4 model parameters, we opted to set the mode M of the axonal radius distribution to a constant value, based on the histological literature (Tomasi et al., 2012; Liewald et al., 2014). Similarly, the parameter α was set from a calibration with histological findings (g_{REF}) (Ikeda and Oka, 2012; see section "Axon Morphological Properties"). The estimated parameters — θ, the right tail of $P(r)$ and β, the scaling parameter of $g(r)$ — enabled the simultaneous assessment of axonal radius and myelination, across the distribution of axons in the visual transcallosal white matter tract. The average value of θ was 0.40 μm across participants, leading to a mean axonal radius of 0.80 μm, inline with previous estimates from histological studies (0.62 μm; Caminiti et al., 2009). The average value of β was 0.67 $\mu m^{-\alpha}$ across participants, consistent with histological measures of the axonal g-ratio in the splenium of the CC (Jung et al., 2018).

The proposed approach inherits the limitations of the MRI methodologies used to estimate the intra-cellular and myelin volume fractions, and subsequently the MRI-measured g-ratio. In the current application, the NODDI model was used to estimate the intra-cellular volume fraction (Zhang et al., 2012). This model assumes identical parallel diffusivity in the extra- and intra-cellular spaces, set to 1.7 μm^2/ms (Zhang et al., 2012). This simplifying assumption might lead to potential bias of the parameter estimates (Jelescu et al., 2015). We estimated that a change in diffusivity within a realistic range (1.5–1.9 μm^2/ms, Guerrero et al., 2019) leads to a change of 4–5% and 1–2% for θ and β, respectively, smaller than the bias arising from the use of group-averaged conduction velocities (12% for θ and 0.90% for β). Alternatives models (e.g., Assaf and Basser, 2005; Fieremans et al., 2011; Campbell et al., 2018;

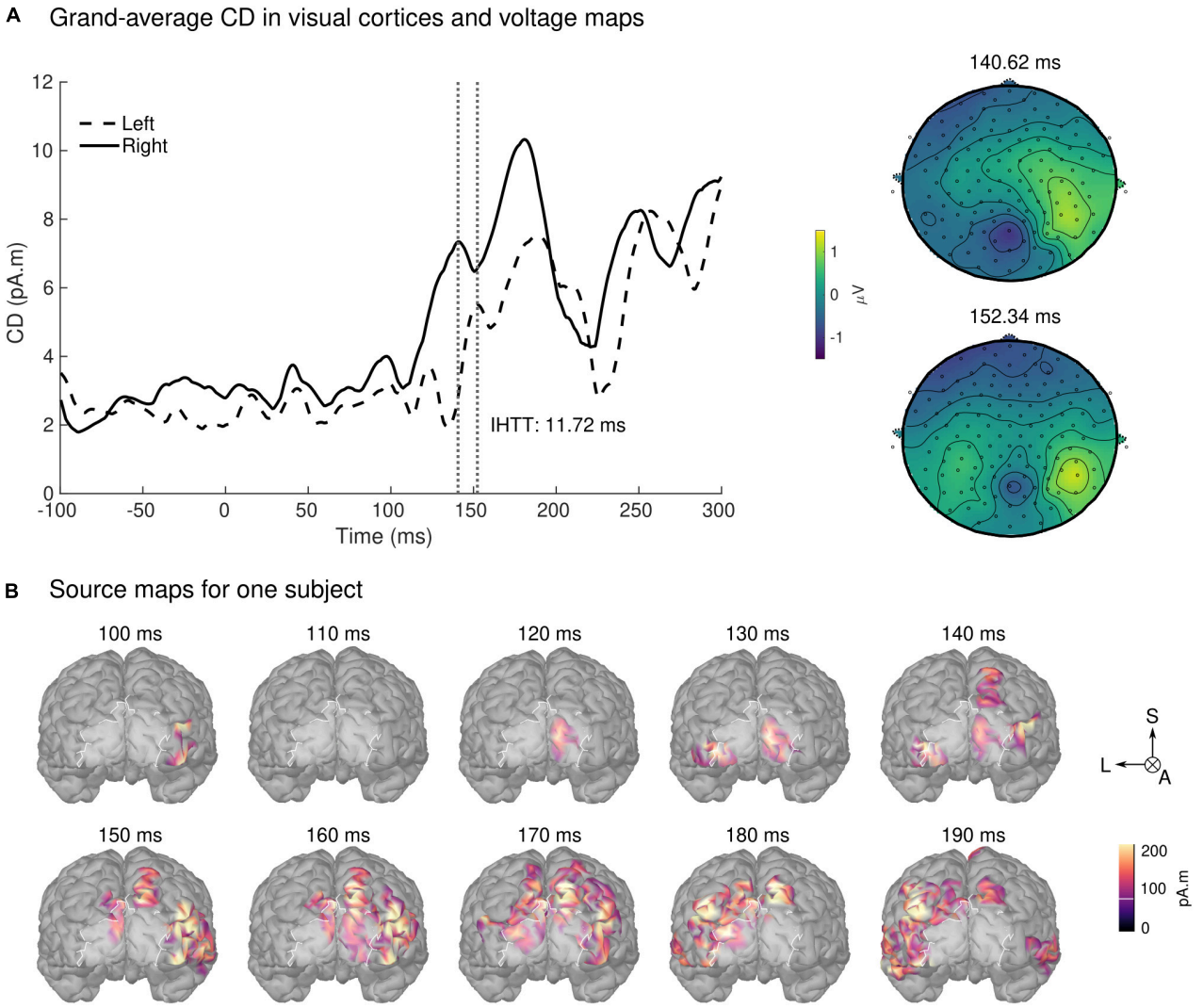

FIGURE 8 | Source space results. **(A)** Group averaged CD for the left visual field stimulation (left panel). The mean activation in the V1V2 ROI on the left and right hemispheres are shown in dashed and solid lines, respectively. Time 0 ms identifies the onset of the stimulus presentation. A first peak on the right hemisphere is observed between 100 and 145 ms, followed by a peak on the left hemisphere after 145 ms. Vertical lines identify the peaks of activation in both hemispheres. IHTT was calculated as the difference between the peak of activation on the hemisphere ipsilateral (left) and contralateral (right) to the stimulation visual field: 11.72 ms. The grand-average sensor level topographic voltage maps corresponding to the identified peaks are shown on the right panel. **(B)** Spatial distribution of the CDs of one exemplar subject projected on this subject's cortex for the left visual field stimulation during the post-stimulus period. Highlighted in white is the V1V2 ROI of interest. For the sake of clarity, we show only groups of source values that contained more than 30 vertices and were 36% above minimal activation. L: Left; S: Superior; A: Anterior.

Ellerbrock and Mohammadi, 2018) may be considered in light of their assumptions, as well as their applicability given the available data.

Estimation of the Interhemispheric Transfer Time and Conduction Velocity

The IHTT was estimated from the group averaged CDs, which allowed for easy identification of the first two maxima of activation in the two hemispheres (**Figure 8**). The IHTT derived as a result of the time interval separating the peaks of CDs at the group level (11.72 ± 2.87 ms) falls within the range (i.e., 8 and 30 ms) of previous IHTT estimates based on *a priori* selection of voltage measurement at electrodes at occipital sites (e.g., Saron and Foxe, 2003; Westerhausen et al., 2006; Whitford et al., 2011; Friedrich et al., 2017; Chaumillon et al., 2018). In our study, we opted for a CD-based estimation of the IHTT as the closest reflection of the evoked neural activity in the regions of interest, consistent with the corresponding white matter tract selection (section "MRI-Based Estimation of the g-ratio"). In addition, this approach helps to overcome the ambiguity of electrode selection in electrode-based IHTT estimations. The resulting estimates of conduction velocity are in agreement with the values reported by Caminiti and colleagues (10 m/s, Caminiti et al., 2013), obtained

TABLE 1 | MRI-measured g-ratios, measured tract length, and estimated conduction velocity with corresponding confidence interval, for each subject in the visual transcallosal tract.

g_{MRI}	Tract length (mm)	Velocity (m/s)	Velocity confidence interval (m/s)
0.69 ± 0.03	155.03	13.23	[10.63; 17.52]
0.71 ± 0.03	149.38	12.75	[10.20; 16.88]
0.71 ± 0.04	133.43	11.38	[9.15; 15.08]
0.69 ± 0.04	136.25	11.63	[9.34; 15.40]
0.67 ± 0.04	154.32	13.17	[10.58; 17.44]
0.69 ± 0.03	171.41	14.63	[11.75; 19.37]
0.71 ± 0.04	157.94	13.48	[10.83; 17.85]
0.71 ± 0.03	149.95	12.79	[10.28; 16.94]
0.69 ± 0.04	152.98	13.05	[10.49; 17.29]
0.68 ± 0.03	142.29	12.14	[9.75; 16.08]
0.68 ± 0.04	155.49	13.27	[10.66; 17.57]
0.69 ± 0.03	172.32	14.70	[11.81; 19.47]
0.69 ± 0.03	184.48	15.74	[12.64; 20.85]
0.69 ± 0.04	154.40	13.17	[10.58; 17.45]

from human histological samples of the same fiber tract. Our results are also consistent with a more recent report that uses a different approach based on Bayesian networks to map the flow of information following left visual stimulation (Deslauriers-Gauthier et al., 2019). The authors observed a transfer of information from the right to the left occipital cortex, between 140 and 160 ms (Deslauriers-Gauthier et al., 2019), in agreement with the latencies of the right and left activations observed in our analysis.

Ideally, IHTT estimates should be performed at the single-subject level to provide microstructure measures specific to each subject. However, the presence of multiple peaks of activation in some individual datasets and the resulting ambiguity in defining the maxima of activation consistently across subjects prevented the estimation of individual IHTT values. These singularities might arise from differences in brain morphology (Saron and Foxe, 2003), inaccurate estimation of the sources, or from the lack of an objective criterion for selecting subjects fulfilling our assumptions on the expected pattern of activations. The difficulty in estimating the IHTT at the subject level has been pointed out in many other studies that showed inconsistent IHTT values across participants and counterintuitively, even negative values in some cases (e.g., Saron and Davidson, 1989; Marzi et al., 1991; Westerhausen et al., 2006; Friedrich et al., 2017). Estimation of the IHTT might be improved with further development on the computation of the inverse solution (Plomp et al., 2010; Mahjoory et al., 2017), and by introducing priors to constrain the time courses of the activations.

Anatomical Substrate for the Interhemispheric Transfer

The proposed model is based on the combination of a structural measure of white matter (MRI-measured g-ratio) and a measure of brain function (axonal conduction velocity). The validity of this model relies on the assumption that both measures may be obtained for a given white matter tract. Anatomical delineation of a white matter tract is generally a routine procedure thanks to MRI tractography techniques (Caminiti et al., 2013; Horowitz et al., 2015; Tournier et al., 2019), allowing the sampling of the MRI-measured g-ratio data along this tract (Schiavi et al., 2022). On the other hand, the underlying mechanisms and anatomy of the inter-hemispheric transfer of the evoked visual activity with Poffenberger's paradigm are still under investigation. Previous literature has used this paradigm to demonstrate an increase in IHTT in acallosal subjects, highlighting the primary role of the CC in visual interhemispheric transfer (Marzi et al., 1991; Di Stefano et al., 1992; Aglioti et al., 1993; Tassinari et al., 1994). In addition, Westerhausen et al. (2006) showed that IHTT is significantly correlated with the structural integrity of the posterior CC, suggesting splenium fibers as the most likely pathway for visual interhemispheric transfer.

The source and target cortical areas of the visual interhemispheric transfer remain to be fully identified. Previous studies have demonstrated the existence of a small patch of transcallosal axons between visual areas 17 and 18 (Clarke and Miklossy, 1990; Aboitiz and Montiel, 2003). This motivated our choice of source and target cortical areas, which led to conduction velocity estimates consistent with previous studies (Caminiti et al., 2013). However, it has been suggested that these connections alone might be insufficient to produce an effective interhemispheric transfer (Innocenti et al., 2015) and higher visual processing areas might be involved.

Future Prospects

The proposed model requires a measure of the MRI-measured g-ratio and axonal conduction velocity in a specific white matter tract of interest. Since measurements of conduction velocity may only be conducted for a limited set of white matter tracts in the human brain, this model, in its current form, cannot be extended to the entire white matter in contrast to other models (e.g., Assaf et al., 2008; Zhang et al., 2011). Instead, this model is geared toward the detailed characterization of a restricted set of white matter tracts. In its proposed form, two parameters relating to the morphology of white matter axons may be estimated from a total of four. Extending the number of estimated parameters requires the use of additional data integrated into the proposed framework. The nature of this data needs to be carefully considered. Alternatively, as was outlined in this work, a subset of the model parameters may be set to a constant value based on histological studies. A prime candidate is the mode of the axonal radius distribution (M), preserved between white matter tracts, individuals, and animal species (Tomasi et al., 2012; Liewald et al., 2014). This choice may need to be reconsidered for the study of brain pathologies that might differentially affect axons of different sizes. Other potential candidates are the parameters α or β that describe the dependence of the fiber g-ratio on axonal radius. In this study, we opted to set α to a constant in expectation of fiber myelination differences identical for all radii. Alternatively, setting β to a constant value may be preferred to allow for the estimation of α, in cases where myelin thickness differences are expected to depend on axonal radius.

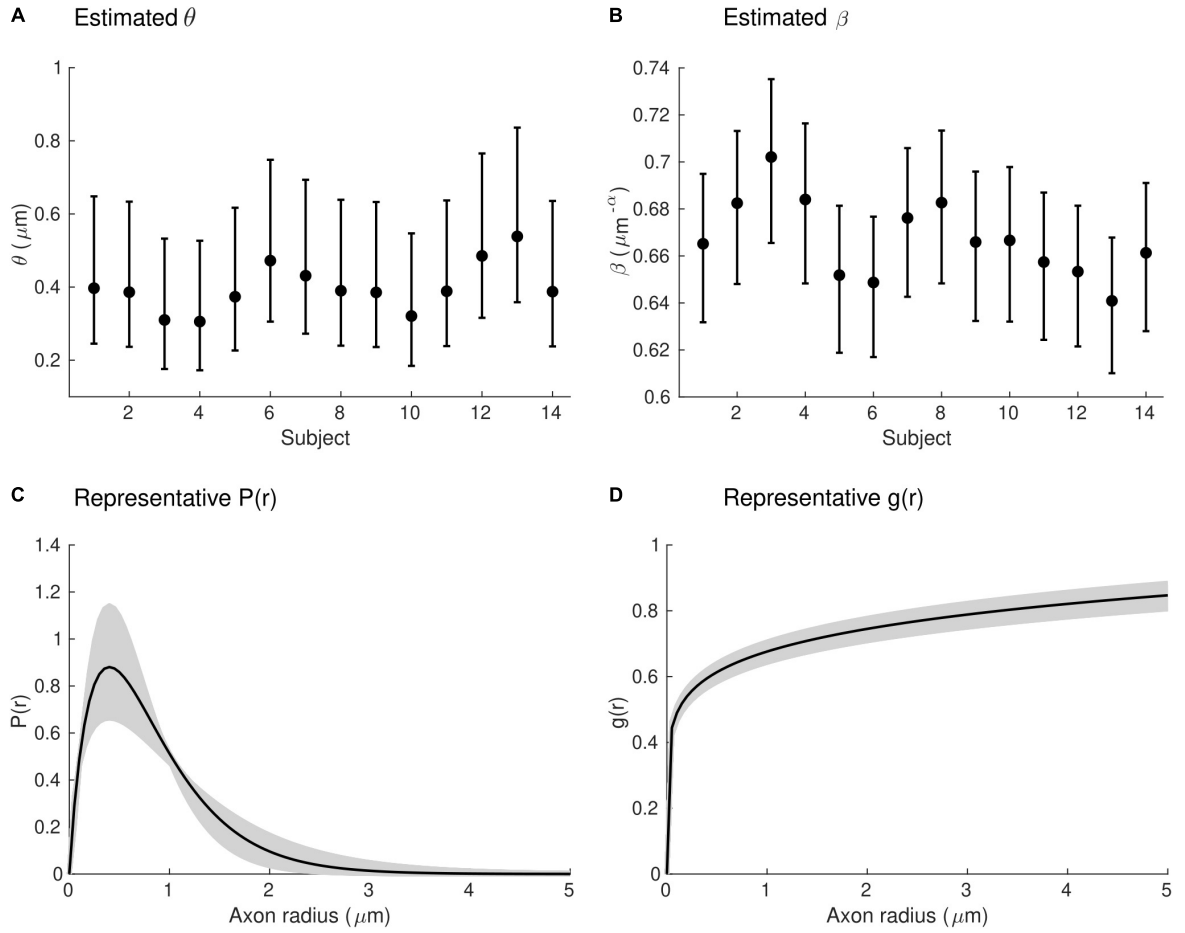

FIGURE 9 | Estimates of axonal morphology obtained from the *in vivo* g_{MRI} and IHTT samples. **(A)** Estimates of the model parameter θ — the width of the right tail of the axonal radius distribution — in the visual transcallosal tract across all study participants. **(B)** Estimates of the model parameter θ — the scaling factor of the axonal g-ratio — in the visual transcallosal tract across all study participants. The error bars indicate the confidence intervals on the parameter estimates. **(C)** Exemplar axonal radius distribution in the visual transcallosal tract for a representative subject (θ = 0.43 μm; confidence interval: 0.27–0.69 μm, shaded area). **(D)** Exemplar dependence of the fiber g-ratio on the axonal radius for the same subject (β = 0.68 $\mu m^{-\alpha}$, confidence interval: 0.64–0.71 $\mu m^{-\alpha}$, shaded area).

In the current study, the estimate of the IHTT was calculated from the average of the EEG-based CD across participants. This led to an average bias in θ and β of 12% and 0.90% across participants, reaching up to 40 and 3%, respectively (**Figure 6**). While small compared to differences between tracts (∼350% for θ and ∼7% for β, see **Figure 4**), this is of the order of the inter-subject differences for these parameters (**Figure 9**) and prevents the estimation of axonal morphological features at the individual level. This limitation represents the primary avenue for future improvements. The question of the accuracy of the parameter estimates and their comparison with histological data might arise subsequently. Estimation of the IHTT from alternative techniques such as transcranial magnetic stimulation might also be considered (Lo and Fook-Chong, 2004; Spitzer et al., 2004; Basso et al., 2006; Deftereos et al., 2008; Marzi et al., 2009). We highlight that the parameters of the proposed model touch on properties of brain tissue that have received little attention in histological studies to date. These include the radius dependence of the axonal g-ratio and the radius dependence of fiber myelination change in health and disease. Validation of the proposed model may therefore bring opportunities for new research avenues for histological studies of the human brain.

CONCLUSION

In summary, we present a novel method that allows the estimation of morphological properties of axons from MRI and EEG data acquired *in vivo* in healthy volunteers. This method enables the combined estimation of axonal radius and myelin thickness and opens the way for improved specificity in studies of the brain conducted from *in vivo* data. The method enables the assessment of the distribution of morphological features across axons and represents a significant step toward *in vivo* histological studies in the human brain.

DATA AVAILABILITY STATEMENT

The datasets presented in this study can be found in online repositories. The names of the repository/repositories and accession number(s) can be found below: doi: 10.5281/zenodo.6027335.

ETHICS STATEMENT

The studies involving human participants were reviewed and approved by Commission d'éthique de la recherche sur l'être humain du canton de Vaud (CER-VD) Avenue de Chailly 23 1012 LAUSANNE Project-ID: 2020-02228. The patients/participants provided their written informed consent to participate in this study.

AUTHOR CONTRIBUTIONS

RO: conception, design of the study, acquisition of MRI and EEG data, data analysis, interpretation, drafting of the manuscript, and critical revision. AP: acquisition of EEG data, data interpretation, and manuscript revision. GD: acquisition of MRI data, data interpretation, and manuscript revision. MDL and AL: conception, design of the study, data interpretation, drafting of the manuscript, and critical revision. All authors contributed to the article and approved the submitted version.

FUNDING

AL was supported by the Swiss National Science Foundation (grant no 320030_184784) and the ROGER DE SPOELBERCH Foundation. MDL was funded by the University of Lausanne grant "Pro-Femmes" and the Swiss National Science Foundation (grant no CRSK-3_196194).

ACKNOWLEDGMENTS

The MRI data were acquired on the MRI platform of the Clinical Neuroscience Department, Lausanne University Hospital. We are thankful to Ileana Jelescu (Department of Radiology, Lausanne University Hospital) for insightful discussions in the process of writing this manuscript.

SUPPLEMENTARY MATERIAL

The Supplementary Material for this article can be found online at: https://www.frontiersin.org/articles/10.3389/fnins.2022.874023/full#supplementary-material

REFERENCES

Aboitiz, F., and Montiel, J. (2003). One hundred million years of interhemispheric communication: The history of the corpus callosum. *Brazilian J. Med. Biol. Res.* 36, 409–420. doi: 10.1590/S0100-879X2003000400002

Aboitiz, F., Scheibel, A. B., Fisher, R. S., and Zaidel, E. (1992). Fiber composition of the human corpus callosum. *Brain Res.* 598, 143–153. doi: 10.1016/0006-8993(92)90178-C

Aglioti, S., Berlucchi, G., Pallini, R., Rossi, G. F., and Tassinari, G. (1993). Hemispheric control of unilateral and bilateral responses to lateralized light stimuli after callosotomy and in callosal agenesis. *Exp. Brain Res.* 95, 151–165. doi: 10.1007/BF00229664

Alexander, D. C., Hubbard, P. L., Hall, M. G., Moore, E. A., Ptito, M., Parker, G. J. M., et al. (2010). Orientationally invariant indices of axon diameter and density from diffusion MRI. *Neuroimage* 52, 1374–1389. doi: 10.1016/j.neuroimage.2010.05.043

Andersson, J. L. R., and Sotiropoulos, S. N. (2016). An integrated approach to correction for off-resonance effects and subject movement in diffusion MR imaging. *Neuroimage* 125, 1063–1078. doi: 10.1016/j.neuroimage.2015.10.019

Assaf, Y., and Basser, P. J. (2005). Composite hindered and restricted model of diffusion (CHARMED) MR imaging of the human brain. *Neuroimage* 27, 48–58. doi: 10.1016/j.neuroimage.2005.03.042

Assaf, Y., Blumenfeld-Katzir, T., Yovel, Y., and Basser, J. (2008). AxCaliber: A Method for Measuring Axon Diameter Distribution from Diffusion MRI. *Magn. Reson. Med.* 59, 1347–1354. doi: 10.1002/mrm.21577

Barazany, D., Basser, P. J., and Assaf, Y. (2009). In vivo measurement of axon diameter distribution in the corpus callosum of rat brain. *Brain* 132, 1210–1220. doi: 10.1093/brain/awp042

Basso, D., Vecchi, T., Kabiri, L. A., Baschenis, I., Boggiani, E., and Bisiacchi, P. S. (2006). Handedness effects on interhemispheric transfer time: A TMS study. *Brain Res. Bull.* 70, 228–232. doi: 10.1016/j.brainresbull.2006.05.009

Bell, A. J., and Sejnowski, T. J. (1995). An Information-Maximization Approach to Blind Separation and Blind Deconvolution. *Neural Comput.* 7, 1129–1159. doi: 10.1162/neco.1995.7.6.1129

Burcaw, L. M., Fieremans, E., and Novikov, D. S. (2015). Mesoscopic structure of neuronal tracts from time-dependent diffusion. *Neuroimage* 114, 18–37. doi: 10.1016/j.neuroimage.2015.03.061

Caminiti, R., Carducci, F., Piervincenzi, C., Battaglia-Mayer, A., Confalone, G., Visco-Comandini, F., et al. (2013). Diameter, length, speed, and conduction delay of callosal axons in macaque monkeys and humans: Comparing data from histology and magnetic resonance imaging diffusion tractography. *J. Neurosci.* 33, 14501–14511. doi: 10.1523/JNEUROSCI.0761-13.2013

Caminiti, R., Ghaziri, H., Galuske, R., Hof, P. R., and Innocenti, G. M. (2009). Evolution amplified processing with temporally dispersed slow neuronal connectivity in primates. *PNAS* 106, 19551–19556. doi: 10.1073/pnas.0907655106

Campbell, J. S. W., Leppert, I. R., Narayanan, S., Boudreau, M., Duval, T., Cohen-Adad, J., et al. (2018). Promise and pitfalls of g-ratio estimation with MRI. *Neuroimage* 182, 80–96. doi: 10.1016/j.neuroimage.2017.08.038

Castella, R., Arn, L., Dupuis, E., Callaghan, M. F., Draganski, B., and Lutti, A. (2018). Controlling motion artefact levels in MR images by suspending data acquisition during periods of head motion. *Magn. Reson. Med.* 80, 2415–2426. doi: 10.1002/mrm.27214

Chaumillon, R., Blouin, J., and Guillaume, A. (2018). Interhemispheric transfer time asymmetry of visual information depends on eye dominance: An electrophysiological study. *Front. Neurosci.* 12:1–19. doi: 10.3389/fnins.2018.00072

Clarke, S., and Miklossy, J. (1990). Occipital Cortex in Man: Organization of Callosal Connections, Related Myelo- and Cytoarchitecture, and Putative Boundaries of Functional Visual Areas. *J. Comp. Neurol.* 298, 188–214. doi: 10.1002/cne.902980205

Cluskey, S., and Ramsden, D. B. (2001). Mechanisms of neurodegeneration in amyotrophic lateral sclerosis. *J. Clin. Pathol. - Mol. Pathol.* 54, 386–392. doi: 10.1136/mp.54.6.386

Daducci, A., Canales-Rodríguez, E. J., Zhang, H., Dyrby, T. B., Alexander, D. C., and Thiran, J. P. (2015). Accelerated Microstructure Imaging via Convex

Optimization (AMICO) from diffusion MRI data. *Neuroimage* 105, 32–44. doi: 10.1016/j.neuroimage.2014.10.026

Deftereos, S. N., Panagopoulos, G., Georgonikou, D., Karageorgiou, E., Andriopoulos, P., and Karageorgiou, C. E. (2008). On the calculation of transcallosal conduction time using transcranial magnetic stimulation. *Funct. Neurol.* 23, 137–140.

Delorme, A., and Makeig, S. (2004). EEGLAB: An open source toolbox for analysis of single-trial EEG dynamics including independent component analysis. *J. Neurosci. Methods* 134, 9–21. doi: 10.1016/j.jneumeth.2003.10.009

Deslauriers-Gauthier, S., Lina, J. M., Butler, R., Whittingstall, K., Gilbert, G., Bernier, P. M., et al. (2019). White matter information flow mapping from diffusion MRI and EEG. *Neuroimage* 201:116017. doi: 10.1016/j.neuroimage.2019.116017

Di Russo, F., Martínez, A., Sereno, M. I., Pitzalis, S., and Hillyard, S. A. (2001). Cortical sources of the early components of the visual evoked potential. *Hum. Brain Mapp.* 15, 95–111. doi: 10.1002/hbm.10010

Di Stefano, M. R., Sauerwein, H. C., and Lassonde, M. (1992). Influence of anatomical factors and spatial compatibility on the stimulus-response relationship in the absence of the corpus callosum. *Neuropsychologia* 30, 177–185. doi: 10.1016/0028-3932(92)90026-I

Does, M. D. (2018). Inferring Brain Tissue Composition and Microstructure via MR Relaxometry. *Neuroimage* 182, 136–148. doi: 10.1016/j.neuroimage.2017.12.087

Dortch, R. D., Harkins, K. D., Juttukonda, M. R., Gore, J. C., and Does, M. D. (2013). Characterizing Inter-Compartmental Water Exchange in Myelinated Tissue using Relaxation Exchange Spectroscopy Richard. *Magn. Reson. Med.* 70, 1–20. doi: 10.1002/mrm.24571

Drakesmith, M., Harms, R., Rudrapatna, S. U., Parker, G. D., Evans, C. J., and Jones, D. K. (2019). Estimating axon conduction velocity in vivo from microstructural MRI. *Neuroimage* 203:116186. doi: 10.1016/j.neuroimage.2019.116186

Edwards, L. J., Kirilina, E., Mohammadi, S., and Weiskopf, N. (2018). Microstructural imaging of human neocortex in vivo. *Neuroimage* 182, 184–206. doi: 10.1016/j.neuroimage.2018.02.055

Ellerbrock, I., and Mohammadi, S. (2018). Four in vivo g-ratio-weighted imaging methods: Comparability and repeatability at the group level. *Hum. Brain Mapp.* 39, 24–41. doi: 10.1002/hbm.23858

Evangelou, N., Konz, D., Esiri, M. M., Smith, S., Palace, J., and Matthews, P. M. (2001). Size-selective neuronal changes in the anterior optic pathways suggest a differential susceptibility to injury in multiple sclerosis. *Brain* 124, 1813–1820. doi: 10.1093/brain/124.9.1813

Feintuch, A., Zhu, Y., Bishop, J., Davidson, L., Dazai, J., Bruneau, B. G., et al. (2007). 4D cardiac MRI in the mouse. *NMR Biomed.* 20, 360–365. doi: 10.1002/nbm.1164

Fieremans, E., Jensen, J. H., and Helpern, J. A. (2011). White matter characterization with diffusional kurtosis imaging. *Neuroimage* 58, 177–188. doi: 10.1016/j.neuroimage.2011.06.006

Fischl, B., Rajendran, N., Busa, E., Augustinack, J., Hinds, O., Yeo, B. T. T., et al. (2008). Cortical folding patterns and predicting cytoarchitecture. *Cereb. Cortex* 18, 1973–1980. doi: 10.1093/cercor/bhm225

Friedrich, P., Ocklenburg, S., Mochalski, L., Schlüter, C., Güntürkün, O., and Genc, E. (2017). Long-term reliability of the visual EEG Poffenberger paradigm. *Behav. Brain Res.* 330, 85–91. doi: 10.1016/j.bbr.2017.05.019

Fukunaga, M., Li, T. Q., Van Gelderen, P., De Zwart, J. A., Shmueli, K., Yao, B., et al. (2010). Layer-specific variation of iron content in cerebral cortex as a source of MRI contrast. *Proc. Natl. Acad. Sci. U. S. A.* 107, 3834–3839. doi: 10.1073/pnas.0911177107

Gibson, E. M., Purger, D., Mount, C. W., Goldstein, A. K., Lin, G. L., Wood, L. S., et al. (2014). Neuronal Activity Promotes Oligodendrogenesis and Adaptive Myelination in the Mammalian Brain. *Science.* 344:1252304. doi: 10.1126/science.1252304

Gramfort, A., Papadopoulo, T., Olivi, E., and Clerc, M. (2010). OpenMEEG: opensource software for quasistatic bioelectromagnetics. *Biomed. Eng. Online* 9:45. doi: 10.1186/1475-925X-9-45

Griswold, M. A., Jakob, P. M., Heidemann, R. M., Nittka, M., Jellus, V., Wang, J., et al. (2002). Generalized Autocalibrating Partially Parallel Acquisitions (GRAPPA). *Magn. Reson. Med.* 47, 1202–1210. doi: 10.1002/mrm.10171

Guerrero, J. M., Adluru, N., Bendlin, B. B., Goldsmith, H. H., Schaefer, S. M., Davidson, R. J., et al. (2019). Optimizing the intrinsic parallel diffusivity in NODDI: An extensive empirical evaluation. *PLoS One* 14:1–17. doi: 10.1371/journal.pone.0217118

Hämäläinen, M. S., and Ilmoniemi, R. J. (1994). Interpreting magnetic fields of the brain: minimum norm estimates. *Med. Biol. Eng. Comput.* 32, 35–42. doi: 10.1007/BF02512476

Helbling, S., Teki, S., Callaghan, M. F., Sedley, W., Mohammadi, S., Griffiths, T. D., et al. (2015). Structure predicts function: Combining non-invasive electrophysiology with in-vivo histology. *Neuroimage* 108, 377–385. doi: 10.1016/j.neuroimage.2014.12.030

Helms, G., Dathe, H., and Dechent, P. (2008a). Quantitative FLASH MRI at 3T using a rational approximation of the Ernst equation. *Magn. Reson. Med.* 59, 667–672. doi: 10.1002/mrm.21542

Helms, G., Dathe, H., Kallenberg, K., and Dechent, P. (2008b). High-resolution maps of magnetization transfer with inherent correction for RF inhomogeneity and T1 relaxation obtained from 3D FLASH MRI. *Magn. Reson. Med.* 60, 1396–1407. doi: 10.1002/mrm.21732

Honey, C. J., Thivierge, J. P., and Sporns, O. (2010). Can structure predict function in the human brain? *Neuroimage* 52, 766–776. doi: 10.1016/j.neuroimage.2010.01.071

Horowitz, A., Barazany, D., Tavor, I., Bernstein, M., Yovel, G., and Assaf, Y. (2015). In vivo correlation between axon diameter and conduction velocity in the human brain. *Brain Struct. Funct.* 220, 1777–1788. doi: 10.1007/s00429-014-0871-0

Hutton, C., Bork, A., Josephs, O., Deichmann, R., Ashburner, J., and Turner, R. (2002). Image distortion correction in fMRI: A quantitative evaluation. *Neuroimage* 16, 217–240. doi: 10.1006/nimg.2001.1054

Ikeda, M., and Oka, Y. (2012). The relationship between nerve conduction velocity and fiber morphology during peripheral nerve regeneration. *Brain Behav.* 2, 382–390. doi: 10.1002/brb3.61

Innocenti, G. M., Caminiti, R., and Aboitiz, F. (2015). Comments on the paper by Horowitz et al. (2014). *Brain Struct. Funct.* 220, 1789–1790. doi: 10.1007/s00429-014-0974-7

Jelescu, I. O., Palombo, M., Bagnato, F., and Schilling, K. G. (2020). Challenges for biophysical modeling of microstructure. *J. Neurosci. Methods* 344:108861. doi: 10.1016/j.jneumeth.2020.108861

Jelescu, I. O., Veraart, J., Adisetiyo, V., Milla, S. S., Novikov, D. S., and Fieremans, E. (2015). One diffusion acquisition and different white matter models: How does microstructure change in human early development based on WMTI and NODDI? *Neuroimage* 107, 242–256. doi: 10.1016/j.neuroimage.2014.12.009

Jenkinson, M., and Smith, S. (2001). A global optimisation method for robust affine registration of brain images. *Med. Image Anal.* 5, 143–156. doi: 10.1016/s1361-8415(01)00036-6

Jones, D. K., Alexander, D. C., Bowtell, R., Cercignani, M., Dell'Acqua, F., McHugh, D. J., et al. (2018). Microstructural imaging of the human brain with a 'super-scanner': 10 key advantages of ultra-strong gradients for diffusion MRI. *Neuroimage* 182, 8–38. doi: 10.1016/j.neuroimage.2018.05.047

Jung, W., Lee, J., Shin, H. G., Nam, Y., Zhang, H., Oh, S. H., et al. (2018). Whole brain g-ratio mapping using myelin water imaging (MWI) and neurite orientation dispersion and density imaging (NODDI). *Neuroimage* 182, 379–388. doi: 10.1016/j.neuroimage.2017.09.053

Kiselev, V. G., and Novikov, D. S. (2018). Transverse NMR relaxation in biological tissues. *Neuroimage* 182, 149–168. doi: 10.1016/j.neuroimage.2018.06.002

Kybic, J., Clerc, M., Abboud, T., Faugeras, O., Keriven, R., and Papadopoulo, T. (2005). A common formalism for the integral formulations of the forward EEG problem. *IEEE Trans. Med. Imaging* 24, 12–28. doi: 10.1109/TMI.2004.837363

Lazari, A., and Lipp, I. (2021). Can MRI measure myelin? Systematic review, qualitative assessment, and meta-analysis of studies validating microstructural imaging with myelin histology. *Neuroimage* 230:117744. doi: 10.1016/j.neuroimage.2021.117744

Lee, H. H., Fieremans, E., and Novikov, D. S. (2018). What dominates the time dependence of diffusion transverse to axons: Intra- or extra-axonal water? *Neuroimage* 182, 500–510. doi: 10.1016/j.neuroimage.2017.12.038

Liewald, D., Miller, R., Logothetis, N., Wagner, H. J., and Schüz, A. (2014). Distribution of axon diameters in cortical white matter: an electron-microscopic study on three human brains and a macaque. *Biol. Cybern.* 108, 541–557. doi: 10.1007/s00422-014-0626-2

Lo, Y. L., and Fook-Chong, S. (2004). A transcranial magnetic stimulation study of the ipsilateral silent period in lower limb muscles. *Neurosci. Lett.* 368, 337–340. doi: 10.1016/j.neulet.2004.07.080

Lutti, A., Corbin, N., Ashburner, J., Ziegler, G., Draganski, B., Phillips, C., et al. (2022). Restoring statistical validity in group analyses of motion-corrupted MRI data. *Hum. Brain Mapp* 43, 1973–1983. doi: 10.1002/hbm.25767

Lutti, A., Dick, F., Sereno, M. I., and Weiskopf, N. (2014). NeuroImage Using high-resolution quantitative mapping of R1 as an index of cortical myelination. *Neuroimage* 93, 176–188. doi: 10.1016/j.neuroimage.2013.06.005

Lutti, A., Hutton, C., Finsterbusch, J., Helms, G., and Weiskopf, N. (2010). Optimization and validation of methods for mapping of the radiofrequency transmit field at 3T. *Magn. Reson. Med.* 64, 229–238. doi: 10.1002/mrm.22421

Lutti, A., Stadler, J., Josephs, O., Windischberger, C., Speck, O., Bernarding, J., et al. (2012). Robust and fast whole brain mapping of the RF transmit field B1 at 7T. *PLoS One* 7:1–7. doi: 10.1371/journal.pone.0032379

MacKay, A. L., and Laule, C. (2016). Magnetic Resonance of Myelin Water: An in vivo Marker for Myelin. *Brain Plast.* 2, 71–91. doi: 10.3233/bpl-160033

Mahjoory, K., Nikulin, V. V., Botrel, L., Linkenkaer-Hansen, K., Fato, M. M., and Haufe, S. (2017). Consistency of EEG source localization and connectivity estimates. *Neuroimage* 152, 590–601. doi: 10.1016/j.neuroimage.2017.02.076

Marzi, C. A. (1999). The Poffenberger paradigm: A first, simple, behavioural tool to study interhemispheric transmission in humans. *Brain Res. Bull.* 50, 421–422. doi: 10.1016/S0361-9230(99)00174-4

Marzi, C. A., Bisiacchi, P., and Nicoletti, R. (1991). Is interhemispheric transfer of visuomotor information asymmetric? Evidence from a meta-analysis. *Neuropsychologia* 29, 1163–1177. doi: 10.1016/0028-3932(91)90031-3

Marzi, C. A., Mancini, F., and Savazzi, S. (2009). Interhemispheric transfer of phosphenes generated by occipital versus parietal transcranial magnetic stimulation. *Exp. Brain Res.* 192, 431–441. doi: 10.1007/s00221-008-1496-4

Melie-Garcia, L., Slater, D., Ruef, A., Sanabria-Diaz, G., Preisig, M., Kherif, F., et al. (2018). Networks of myelin covariance Lester. *Hum. Brain Mapp.* 39, 1532–1554. doi: 10.1002/hbm.23929

Miles, W. R. (1930). Ocular dominance in human adults. *J. Gen. Psychol.* 3, 412–430. doi: 10.1080/00221309.1930.9918218

Mohammadi, S., Carey, D., Dick, F., Diedrichsen, J., Sereno, M. I., Reisert, M., et al. (2015). Whole-brain in-vivo measurements of the axonal G-ratio in a group of 37 healthy volunteers. *Front. Neurosci.* 9:1–13. doi: 10.3389/fnins.2015.00441

Nilsson, M., Lasič, S., Drobnjak, I., Topgaard, D., and Westin, C. F. (2017). Resolution limit of cylinder diameter estimation by diffusion MRI: The impact of gradient waveform and orientation dispersion. *NMR Biomed.* 30, 1–13. doi: 10.1002/nbm.3711

Oldfield, R. C. (1971). The assessment and analysis of handedness: the Edinburgh inventory. *Neuropsychologia* 9, 97–113. doi: 10.1016/0028-3932(71)90067-4

Oostenveld, R., Fries, P., Maris, E., and Schoffelen, J. M. (2011). FieldTrip: Open source software for advanced analysis of MEG, EEG, and invasive electrophysiological data. *Comput. Intell. Neurosci.* 2011:156869. doi: 10.1155/2011/156869

Plomp, G., Michel, C. M., and Herzog, M. H. (2010). Electrical source dynamics in three functional localizer paradigms. *Neuroimage* 53, 257–267. doi: 10.1016/j.neuroimage.2010.06.037

Preibisch, C., and Deichmann, R. (2009). Influence of RF spoiling on the stability and accuracy of T1 mapping based on spoiled FLASH with varying flip angles. *Magn. Reson. Med.* 61, 125–135. doi: 10.1002/mrm.21776

Rushton, W. A. H. (1951). A theory of the effects of fibre size in medullated nerve. *J. Physiol.* 115, 101–122. doi: 10.1113/jphysiol.1951.sp004655

Saron, C., and Foxe, J. J. (2003). ""Complexities of Interhemispheric Communication in Sensorimotor Tasks Revealed by High-Density Event-Related Potential Mapping," in *The Asymmetrical Brain*, ed. R. J. Eds ((Cambridge, MA: MIT press), 342-408. doi: 10.7551/mitpress/1463.003.0014

Saron, C. D., and Davidson, R. J. (1989). Visual Evoked Potential Measures of Interhemispheric Transfer Time in Humans. *Behav. Neurosci.* 103, 1115–1138. doi: 10.1037/0735-7044.103.5.1115

Schiavi, S., Lu, P. J., Weigel, M., Lutti, A., Jones, D. K., Kappos, L., et al. (2022). Bundle myelin fraction (BMF) mapping of different white matter connections using microstructure informed tractography. *Neuroimage* 249:118922. doi: 10.1016/j.neuroimage.2022.118922

Schiffler, P., Tenberge, J.-G., Wiendl, H., and Meuth, S. G. (2017). Cortex Parcellation Associated Whole White Matter Parcellation in Individual Subjects. *Front. Hum. Neurosci.* 11:1–10. doi: 10.3389/fnhum.2017.00352

Sepehrband, F., Alexander, D. C., Clark, K. A., Kurniawan, N. D., Yang, Z., and Reutens, D. C. (2016). Parametric probability distribution functions for axon diameters of corpus callosum. *Front. Neuroanat.* 10, 1–9. doi: 10.3389/fnana.2016.00059

Slater, D. A., Melie-Garcia, L., Preisig, M., Kherif, F., Lutti, A., and Draganski, B. (2019). Evolution of white matter tract microstructure across the life span. *Hum. Brain Mapp.* 40, 2252–2268. doi: 10.1002/hbm.24522

Spitzer, C., Willert, C., Grabe, H. J., Rizos, T., Möller, B., and Freyberger, H. J. (2004). Dissociation, Hemispheric Asymmetry, and Dysfunction of Hemispheric Interaction: A Transcranial Magnetic Stimulation Approach. *J. Neuropsychiatry Clin. Neurosci.* 16, 163–169. doi: 10.1176/jnp.16.2.163

Stephan, K. E., Tittgemeyer, M., Knösche, T. R., Moran, R. J., and Friston, K. J. (2009). Tractography-based priors for dynamic causal models. *Neuroimage* 47, 1628–1638. doi: 10.1016/j.neuroimage.2009.05.096

Stikov, N., Campbell, J. S. W., Stroh, T., Lavelée, M., Frey, S., Novek, J., et al. (2015). In vivo histology of the myelin g-ratio with magnetic resonance imaging. *Neuroimage* 118, 397–405. doi: 10.1016/j.neuroimage.2015.05.023

Stikov, N., Perry, L. M., Mezer, A., Rykhlevskaia, E., Wandell, B. A., Pauly, J. M., et al. (2011). Bound pool fractions complement diffusion measures to describe white matter micro and macrostructure. *Neuroimage* 54, 1112–1121. doi: 10.1016/j.neuroimage.2010.08.068

Stüber, C., Morawski, M., Schäfer, A., Labadie, C., Wähnert, M., Leuze, C., et al. (2014). Myelin and iron concentration in the human brain: A quantitative study of MRI contrast. *Neuroimage* 93, 95–106. doi: 10.1016/j.neuroimage.2014.02.026

Sui, J., Huster, R., Yu, Q., Segall, J. M., and Calhoun, V. D. (2014). Function-Structure Associations of the Brain: Evidence from Multimodal Connectivity and Covariance Studies. *Neuroimage* 102, 11–23. doi: 10.1016/j.neuroimage.2013.09.044

Tabelow, K., Balteau, E., Ashburner, J., Callaghan, M. F., Draganski, B., Helms, G., et al. (2019). hMRI – A toolbox for quantitative MRI in neuroscience and clinical research. *Neuroimage* 194, 191–210. doi: 10.1016/j.neuroimage.2019.01.029

Tadel, F., Baillet, S., Mosher, J. C., Pantazis, D., and Leahy, R. M. (2011). Brainstorm: A user-friendly application for MEG/EEG analysis. *Comput. Intell. Neurosci.* 2011:879716. doi: 10.1155/2011/879716

Tassinari, G., Aglioti, S., Pallini, R., Berlucchi, G., and Rossi, G. F. (1994). Interhemispheric integration of simple visuomotor responses in patients with partial callosal defects. *Behav. Brain Res.* 64, 141–149. doi: 10.1016/0166-4328(94)90126-0

Tomasi, S., Caminiti, R., and Innocenti, G. M. (2012). Areal differences in diameter and length of corticofugal projections. *Cereb. Cortex* 22, 1463–1472. doi: 10.1093/cercor/bhs011

Tournier, J. D., Smith, R., Raffelt, D., Tabbara, R., Dhollander, T., Pietsch, M., et al. (2019). MRtrix3: A fast, flexible and open software framework for medical image processing and visualisation. *Neuroimage* 202:116137. doi: 10.1016/j.neuroimage.2019.116137

Veraart, J., Nunes, D., Rudrapatna, U., Fieremans, E., Jones, D. K., Novikov, D. S., et al. (2020). Nonivasive quantification of axon radii using diffusion MRI. *Elife* 9:e49855. doi: 10.7554/eLife.49855

Waxman, S., and Bennett, M. (1972). Relative Conduction Velocities of Small Myelinated and Non-myelinated Fibres in the Central Nervous System. *Nat. New Biol.* 238, 217–219. doi: 10.1038/newbio238217a0

Wegiel, J., Kaczmarski, W., Flory, M., Martinez-Cerdeno, V., Wisniewski, T., Nowicki, K., et al. (2018). Deficit of corpus callosum axons, reduced axon diameter and decreased area are markers of abnormal development of interhemispheric connections in autistic subjects. *Acta Neuropathol. Commun.* 6:143. doi: 10.1186/s40478-018-0645-7

Weiskopf, N., Mohammadi, S., Lutti, A., and Callaghan, M. F. (2015). Advances in MRI-based computational neuroanatomy: From morphometry to in-vivo histology. *Curr. Opin. Neurol.* 28, 313–322. doi: 10.1097/WCO.0000000000000222

West, K. L., Kelm, N. D., Carson, R. P., and Does, M. D. (2016). A revised model for estimating g-ratio from MRI. *Neuroimage* 125, 1155–1158. doi: 10.1016/j.neuroimage.2015.08.017

Westerhausen, R., Kreuder, F., Woerner, W., Huster, R. J., Smit, C. M., Schweiger, E., et al. (2006). Interhemispheric transfer time and structural properties of the corpus callosum. *Neurosci. Lett.* 409, 140–145. doi: 10.1016/j.neulet.2006.09.028

Whitford, T. J., Kubicki, M., Ghorashi, S., Hawley, K. J., and McCarley, R. W. (2011). Predicting Inter-Hemispheric Transfer Time from the Diffusion Properties of the Corpus Callosum in Healthy Individuals and Schizophrenia Patients: A Combined ERP and DTI Study. *Neuroimage* 54, 2318–2329. doi: 10.1016/j.neuroimage.2010.10.048

Zhang, H., Hubbard, P. L., Parker, G. J. M., and Alexander, D. C. (2011). Axon diameter mapping in the presence of orientation dispersion with diffusion MRI. *Neuroimage* 56, 1301–1315. doi: 10.1016/j.neuroimage.2011.01.084

Zhang, H., Schneider, T., Wheeler-kingshott, C. A., and Alexander, D. C. (2012). NODDI: Practical in vivo neurite orientation dispersion and density imaging of the human brain. *Neuroimage* 61, 1000–1016. doi: 10.1016/j.neuroimage.2012.03.072

Conflict of Interest: The authors declare that the research was conducted in the absence of any commercial or financial relationships that could be construed as a potential conflict of interest.

Received: 19 December 2022 | Revised: 12 June 2023 | Accepted: 26 June 2023

DOI: 10.1002/hbm.26420

RESEARCH ARTICLE

WILEY

Single-subject electroencephalography measurement of interhemispheric transfer time for the in-vivo estimation of axonal morphology

Rita Oliveira | Marzia De Lucia | Antoine Lutti

Laboratory for Research in Neuroimaging, Department of Clinical Neuroscience, Lausanne University Hospital and University of Lausanne, Lausanne, Switzerland

Correspondence
Rita Oliveira, Laboratory for Research in Neuroimaging, Department of Clinical Neuroscience, Lausanne University Hospital and University of Lausanne, Lausanne, Switzerland.
Email: ana.veiga-de-oliveira@chuv.ch

Funding information
Bertarelli Catalyst Foundation; ROGER DE SPOELBERCH Foundation; Schweizerischer Nationalfonds zur Förderung der Wissenschaftlichen Forschung, Grant/Award Numbers: 320030_184784, 32003B_212981

Abstract

Assessing axonal morphology in vivo opens new avenues for the combined study of brain structure and function. A novel approach has recently been introduced to estimate the morphology of axonal fibers from the combination of magnetic resonance imaging (MRI) data and electroencephalography (EEG) measures of the interhemispheric transfer time (IHTT). In the original study, the IHTT measures were computed from EEG data averaged across a group, leading to bias of the axonal morphology estimates. Here, we seek to estimate axonal morphology from individual measures of IHTT, obtained from EEG data acquired in a visual evoked potential experiment. Subject-specific IHTTs are computed in a data-driven framework with minimal a priori constraints, based on the maximal peak of neural responses to visual stimuli within periods of statistically significant evoked activity in the inverse solution space. The subject-specific IHTT estimates ranged from 8 to 29 ms except for one participant and the between-session variability was comparable to between-subject variability. The mean radius of the axonal radius distribution, computed from the IHTT estimates and the MRI data, ranged from 0 to 1.09 μm across subjects. The change in axonal g-ratio with axonal radius ranged from 0.62 to 0.81 $\mu m^{-\alpha}$. The single-subject measurement of the IHTT yields estimates of axonal morphology that are consistent with histological values. However, improvement of the repeatability of the IHTT estimates is required to improve the specificity of the single-subject axonal morphology estimates.

KEYWORDS
conduction velocity, EEG, g-ratio, MRI, myelination, tractography

1 | INTRODUCTION

The radius and myelin thickness of axons are morphological features that play an essential role in neuronal communications and consequently, brain function (MacKay & Laule, 2016; Rushton, 1951; Waxman & Bennett, 1972). Axons of different radius are affected differentially over the course of diseases such as multiple sclerosis (Evangelou et al., 2001), autism (Wegiel et al., 2018), and motor neuron disease (Cluskey & Ramsden, 2001). Therefore, the specific assessment of morphological properties of axons from in-vivo data is

Marzia De Lucia and Antoine Lutti contributed equally to this study.

essential for the study of brain function, and for the monitoring of disease evolution in patient populations. Biomarkers computed from magnetic resonance imaging (MRI) data can allow the in-vivo monitoring of microscopic properties of brain tissue (Does, 2018; Lutti et al., 2014; Stikov et al., 2015). However, these biomarkers suffer from a lack of specificity with regards to morphological properties of axons, and represent averages across the large axon populations present within an MRI voxel.

Recent developments have aimed to address the lack of specificity of MRI data to morphological properties of axons. Theoretical models have been introduced that describe the MRI signal as a function of microscopic properties of brain tissue such as axonal radius (Alexander et al., 2010; Assaf et al., 2008; Barakovic et al., 2021; Benjamini et al., 2014; Fan et al., 2020; Harkins et al., 2021; Zhang et al., 2011) or relative myelination (Mohammadi & Callaghan, 2021; Stikov et al., 2015). Such models have been applied to the study of the relationship between brain structure and function (Berman et al., 2019; Horowitz et al., 2015; Mancini et al., 2021), the study of variations of axonal radius across the brain (Barakovic et al., 2021; Huang et al., 2020), and to the study of the spinal cord (Warner et al., 2023). However, diffusion MRI lacks sensitivity to small axons, leading to overestimation of axonal radius estimates in studies of the central nervous system (Drobnjak et al., 2016; Nilsson et al., 2017; Veraart et al., 2020).

Recently, we proposed a new approach that allows the non-invasive estimation of axonal radius and relative myelination of axonal fibers in humans (Oliveira et al., 2022). The proposed method relies on a biophysical model that links these morphological properties of white matter fibers and data collected in vivo. This in-vivo data consists of MRI measures of the g-ratio (gMRI, Campbell et al., 2018)—sampled along a white matter tract of interest—and a measure of axonal conduction velocity in the same tract. In Oliveira et al., 2022 we focused on the visual transcallosal tract, whose conduction velocity can be estimated with an electroencephalography (EEG) paradigm that measures the delay of visual information transfer across hemispheres, that is, the interhemispheric transfer time (IHTT).

The bedrock of visual IHTT estimation is the crossed organization of the visual system: a unilaterally presented visual stimulus first reaches the contralateral cortex and is then transferred to the ipsilateral cortex (Chaumillon et al., 2018; Saron & Davidson, 1989) via the splenium of the corpus callosum (e.g., Martin et al., 2007; Saron & Davidson, 1989). Due to its temporal resolution, EEG is particularly suited for non-invasive estimation of the IHTT. Classically, this estimation is based on the latency difference of the evoked activity recorded from homologous electrodes (e.g., Brown et al., 1994; Saron & Davidson, 1989). This approach relies on the assumption that maxima in the voltage spatial distribution across the electrode montage reflect the maxima of the underlying electromagnetic field produced by active neurons. An ad hoc selection of the electrodes of interest and of the latency at which the transfer is most likely to occur is required for this approach. Either the positive (P1) or negative (N1) components of the event-related potentials (ERPs) have been considered as a proxy for the neuronal activations (e.g., Brown et al., 1994; Ipata et al., 1997; Moes et al., 2007; Saron & Davidson, 1989; Westerhausen et al., 2006; Whitford et al., 2011). The P1 component represents an early stage of visual processing (Martin et al., 2007; Whitford et al., 2011), while N1 may be a closer reflection of callosal transfer (Brown & Jeeves, 1993; Ipata et al., 1997). Moreover, while P1 originates from spatially localized activations over the extrastriate cortex of the fusiform gyrus (Di Russo et al., 2001; Ipata et al., 1997), the voltage generators for N1 are widespread, encompassing occipital and parietal regions (Di Russo et al., 2001; Ipata et al., 1997). In the absence of sufficient knowledge of the spatio-temporal distributions of neural activations in response to visual stimuli, the ad hoc selection of electrodes and latencies remains an open question.

In this light, our previous work aimed to improve IHTT estimation by proposing an alternative source-based IHTT estimation approach that overcomes the a priori choice of electrodes and components (Oliveira et al., 2022). Performing source reconstruction on the voltage measurements enhances EEG spatial resolution. It also allows the reconstruction of neuronal activity within homologous cortical regions and consequently, the computation of the IHTT from the latency difference between the two maximal neuronal activations. In Oliveira et al., 2022, however, estimation of the IHTT was conducted from a group average of the time courses of the source reconstructed signal. According to simulation results, this may have led to bias of up to 40% in the resulting subject-specific estimates of axonal radius and myelination (Oliveira et al., 2022). Thus, estimation of the IHTT at the subject level is of the utmost importance for the accurate estimation of axonal morphological features with this approach.

In the current study, we seek to obtain subject-specific estimates of the IHTT from EEG data to allow accurate estimation of axonal morphology at the subject level. We extend the cortical region considered for the estimation of the maximal activity upon visual stimulation. This enables the inclusion of activity originating from widespread generators of the visual response and mitigates the effect of errors in the localization of the signal sources that have more impact in subject-level analyses. We introduce three quantitative metrics that help resolve ambiguities on the selection of the maximal activity in each hemisphere and support the attribution of the IHTT estimates to visual-evoked activity. We evaluate the within- and between-session repeatability of the IHTT estimates. Finally, we use the subject-specific IHTT values to compute estimates of axonal morphology in the occipital transcallosal tract of each participant. The between-session and between-subject variabilities of the morphological estimates were compared to assess the specificity of axonal morphological estimates.

2 | METHODS

2.1 | Participants

The same dataset as in Oliveira et al., 2022 was used. In brief, the data includes a set of EEG and MRI recordings obtained from 17 healthy

volunteers. Three participants were excluded due to artifacted EEG recordings, resulting in a final dataset of 14 participants (eight males; age: mean ± SD = 27.14 ± 3.86 years). All participants were right-handed as assessed with the Edinburgh Handedness Inventory (Oldfield, 1971) and three of them were left-eye dominant as evaluated by looking through a small opening at a distant object (Miles, 1930). The participants did not have neurological/psychiatric disorders and had normal or corrected-to-normal vision. Three of these participants were invited to do a second EEG recording session for a test–retest evaluation.

2.2 | Electroencephalography-based estimation of the IHTT

2.2.1 | Experimental paradigm

The experimental paradigm is the same as previously reported by our group (Oliveira et al., 2022). We presented a black and white checkerboard on a gray background presented on the lower left visual field (LVF) or right visual field (RVF). The checkboard (4° diameter) was presented on a gray background (20 cd/m^2) for 100 ms at 6° horizontal and 6° vertical distance from the centrally located fixation cross (0.8° in size). Each experimental block contained 205 trials (95 for each visual field and 15 with no stimulus). Inter-trial intervals varied randomly from 1 to 2 s—sufficient for the visual neuronal activity to reach a baseline before presentation of a new stimulus given that manual reaction times are in the range of ∼200–300 ms (e.g., Fendrich et al., 2004; Marzi et al., 1991) The trials were presented in a pseudorandom order. The experiment was administered using Psychtoolbox-3.0.16 in Matlab (R2019b, The Mathworks, Natick, MA). Participants were seated 80 cm away from a screen (61 cm, 60 Hz refreshing rate). Subjects were instructed to keep their gaze on the central fixation cross and press a button (with index finger) as quickly as possible after each stimulus appearance. There were six experimental blocks presented pseudo-randomly, three were answered with the right hand and the remaining three with the left hand.

2.2.2 | Data acquisition

Continuous 128-channel EEG was recorded with an Ag/AgCl electrode cap (waveguard™original, ANT Neuro, Hengelo, Netherlands) and the Micromed recording system (Micromed SystemPlus Evolution, Mogliano Veneto, Italy). All electrodes were referenced to FPz and grounded at AFFz. Electrooculogram was recorded using two additional horizontal electrodes placed to the outer canthi of each eye. The sampling rate was 1024 Hz. Electrode impedance was below 20 kΩ. Using the xensor™ digitizer (ANT Neuro, Hengelo, Netherlands) the 3D head shape and electrode positions were digitized for each participant.

2.2.3 | Data processing

The data was pre-processed using Fieldtrip, version 20191206 (Oostenveld et al., 2011) and EEGLAB, version 13.4.4b (Delorme & Makeig, 2004) toolboxes on MATLAB (R2021a, The Mathworks, Natick, MA). We first bandpass-filtered (digital filters) the continuous raw EEG signal at 0.1–40 Hz and extracted EEG epochs from 100 ms prior to stimulus onset to 300 ms after stimulus presentation. During this 100 ms, we could reasonably assume there was no influence of the evoked activity of the previous stimulus given the large inter-trial intervals value which ranges between 1 and 2 s; a 100-ms baseline period is also a typical choice across a range of studies of visual evoked analysis (Friedrich et al., 2017; Horowitz et al., 2015; Plomp et al., 2010; Westerhausen et al., 2006). Trials containing large eye movements were first removed on visual inspection. Next, we used Independent Component Analysis with the *runica* algorithm (Bell & Sejnowski, 1995) to identify and remove components containing eye movement-related artifacts. Semi-automatic artifact detection with a threshold of 80 μV was used to identify and exclude additional artifact epochs from further analysis: 20.5% and 21.3% of the trials were rejected on average across participants, leading to an average number of accepted trials of 453 (range: 350–528) and 449 (range: 364–528) for the LVF and RVF stimulation, respectively. The same threshold of 80 μV was used to identify artifact electrodes, which were next interpolated using the nearest neighbor: 5.9% of electrodes (range 3–14 electrodes) were interpolated on average across participants. The EEG epochs were re-referenced to the average reference and DC drift was removed by subtracting the average amplitude within each epoch. The global field power (GFP), a measure of the spatial standard deviation of the electrical potentials, was computed for each dataset in order to relate the evoked components with the IHTT latencies (Hamburger & Michelle, 1991).

For source reconstruction, we used Brainstorm, version 16-04-2021 (Tadel et al., 2011) toolbox. Each subject's MRI-based head was first registered to the EEG-digitized head with an iterative algorithm. A head model using a 3-layer Boundary Element Method (Gramfort et al., 2010; Kybic et al., 2005) was created on each subject MRI image with 15,000 vertices on the gray matter. Finally, current densities (CD, pA.m) time courses were estimated for each condition (LVF; RVF), source vertice, and trial for each subject using the minimum-norm current density approach (Hämäläinen & Ilmoniemi, 1994).

We defined the occipital region of interest (ROI) as including the *inferior parietal*, *lateral occipital*, *superior parietal*, *cuneus*, *lingual*, *fusiform*, *pericalcarine*, *precuneus* of the Desikan-Killiany atlas (Desikan et al., 2006). The use of a bigger cortical region at the subject-specific level compared to the primary and secondary visual cortices used originally (Oliveira et al., 2022) is motivated by several reasons. First, the localization of neuronal generators in deep cortical fissures and the specificities of each individual's cortex make the source reconstruction around the calcarine sulcus challenging (Creel, 2012). Consequently, mislocalization of the signal between hemispheres or across neighboring regions within the same hemisphere is likely to occur

(Cuffin, 1998; Grech et al., 2008), with a stronger impact on IHTT estimates at the subject- than group-level (lower signal-to-noise ratio). Second, the widespread distribution of generators over the posterior cortex is consistent with the late latencies of maximal cortical activity used for IHTT estimation (>140 ms). In particular, between 136 and 146 ms (late P1 component), the neuronal generators are localized in the ventral extrastriate cortex of the fusiform gyrus, and from 150 to 200 ms (N1 complex), deep sources can be found in the parietal lobe (Di Russo et al., 2001). Therefore, given that the visual response is not restricted within the primary visual areas, by adopting a larger region we include the activity originating from the main generators of such response.

2.2.4 | Cluster-based statistical test

In order to ensure that neuronal activity was due to the evoked activity in response to the visual stimuli, we identified the post-stimulus period during which the estimated CDs were statistically different compared to the baseline period (Figure S1a). To this aim, we implemented a cluster permutation statistical test (Maris & Oostenveld, 2007) on the CD waveforms (time × source vertice × trial matrix) extracted within our ROI for each participant and condition. We defined the post-stimulus period between 100 and 250 ms after stimulus onset for each trial and source vertice. This interval is shorter than the full post-stimulus period but includes the main components of the visual response (Di Russo et al., 2001), avoiding the need to extend the cluster permutation analysis to the whole post-stimulus period and alleviating computational demand. The fluctuations of the baseline activity over time are not of interest given that we aim at testing the modulation of the activity after the presentation of the stimulus in comparison to a representative average brain activity within the baseline, i.e. a period of no stimulus. Thus we defined the baseline period as the time-average of the 100 ms prior to stimulus onset for each trial and source vertice. To keep the time dimension of the baseline matrix (time × source vertice × trial matrix) consistent with the post-stimulus period in subsequent analyses, the average baseline value for each trial and source vertice was replicated along the time dimension.

In brief, the cluster permutation statistical test starts by clustering individual data samples based on temporal and spatial proximity exhibiting significant *t*-values ($p < .05$). The sum of the samples' t-values belonging to each cluster is submitted to a second-order inference stage. Trial labels (baseline and post-stimulus) are permuted 5000 times to estimate the distribution of maximal cluster-level statistics. A two-tailed Monte-Carlo *p*-value ($p < .05$) is then used to identify the significant clusters. While this statistical test identifies the clusters in time and space with significant differences between baseline and post-stimulus, the sign of the t-statistic does not provide information regarding which of the periods has a stronger response in magnitude (Figure S1a). For instance, an increase in positive activity from baseline (B) to post-stimulus (P) (e.g., from 5 to 10 pA.m) produces the same effect as a decrease in negative activity from baseline to post-stimulus (e.g., from −10 to −5 pA.m). To probe where the response was stronger, we computed the absolute difference between the post-stimulus and baseline period (|P|-|B|, Figure S1b), allowing us to distinguish between the two aforementioned cases (|P|-|B| > 0 and |P|-|B| < 0). The space–time matrix where the post-stimulus activity was higher compared to the baseline is then multiplied by the previously obtained clusters to provide the final matrix (Figure S1c). This final matrix contained the clusters in space and time (time × source vertice matrix) that were statistically significant and higher in the post-stimulus period compared to the ongoing activity and was used to mask the evoked CD within the post-stimulus period (time-× source vertice matrix).

2.2.5 | Measures of interhemispheric transfer time

The hypothesis underlying the applied EEG paradigm is that lateralized visual stimuli induce an activity increase in the contralateral hemisphere prior to the ipsilateral one. IHTT can then be estimated at the source-level by taking the latency difference between the two maximal neuronal activations of occipital homologous regions. The maximal neuronal activations are measured on the CD time courses within our ROI.

For each participant and condition, we extracted the original CD time courses, this is, without statistical analysis (of dimension time points × source vertices × number of trials) within our regions of interest in the left and right hemispheres separately. The CDs were averaged across trials (leading to a matrix of dimension time points × source vertices). The absolute value of the resulting CDs was averaged across vertices in each hemisphere, resulting in a time course of CDs (time vector) that was used to estimate IHTT for each participant and condition. For the group IHTT estimation, for each condition, the CD time courses were averaged across subjects to create a group time course.

To estimate IHTT, we first used an automatic peak-picking algorithm (*findpeaks* from MATLAB with minimum peak width of 4 ms) to identify the peak with maximum intensity in the interval between 130 and 220 ms post-stimulus onset in the ipsilateral and contralateral CD time courses. This interval was defined in order to include the two maxima in the CD time courses at the group level. IHTT was calculated by subtracting the latency of the peak associated with the direct path response (contralateral activation—e.g., right hemisphere for the LVF) from the latency of the peak of the indirect path response (ipsilateral—e.g., left hemisphere for the LVF). This procedure produced an IHTT estimation based on the reconstructed time course in the source space.

To confirm the origin of the estimated IHTT as the result of a visual-evoked activity, we computed the IHTT from an additional two waveforms obtained from the statistical analysis: the CDs masked with the masking matrix of the significant clusters (Section 2.2.4) and the time course of the number of vertices of the significant clusters of the same masking matrix. Estimating IHTT based on the number of vertices within the significant clusters rather than on the

waveforms of activity represents another proxy for the interhemispheric transfer given that the significant activation is expected to increase spatially first in the contralateral and then later in the ipsilateral hemisphere. As previously, we used the same peak-picking algorithm (*findpeaks* from MATLAB) to extract the peak of activity within our ROI in these two waveforms and estimated IHTT by taking the latency difference between the ipsilateral and contralateral peaks.

The consistency of the IHTT estimates obtained from the original CDs, from the CDs masked with the significant clusters, and from the time course of the number of significant vertices was measured with a Pearson's Correlation Coefficient.

All codes are available on our online repository: https://github.com/DNC-EEG-platform/SingleSubjectIHTTEstimation.

Peak selection reliability

To identify the subjects and conditions for which the IHTT estimates were uncertain due to the presence of multiple peaks, we searched in the three types of waveforms all possible maxima falling within 5% of the global maximum, using the *findpeaks* MATLAB command.

Within-session and between-session repeatability

The within-session repeatability of the IHTT estimates obtained on the original CDs waveforms was assessed by subdividing the trials from the first session of each participant into two non-overlapping random subsets and estimating the IHTT on each of the subsets. The consistency of the IHTT estimates between the two subsets was assessed with Pearson's Correlation Coefficient across participants. To evaluate the magnitude of the within-session IHTT variability we computed the absolute difference between the IHTT estimates from the two subsets of trials.

To measure the repeatability of the IHTT estimates between sessions, we performed a second EEG recording session on three of the participants and estimated IHTT on the original CDs waveforms. The consistency of the IHTT estimates between sessions was assessed with Pearson's Correlation Coefficient across participants. To evaluate the magnitude of the between-session IHTT variability we computed the mean absolute difference between the IHTT estimates across participants.

2.3 | Magnetic resonance imaging-based estimation of the G-Ratio

2.3.1 | Data acquisition

Data acquisition was conducted as reported in our previous work (Oliveira et al., 2022). In brief, MRI data were collected on a 3 T MRI system (Magnetom Prisma; Siemens Medical Systems, Erlangen, Germany). The MRI protocol included a 3D MPRAGE scan (1 mm^3 isotropic voxel size) with TR/TE/TI = 2000/2.39/920 ms and $\alpha = 9°$; a multi-parameter protocol that included three multi-echo 3D FLASH scans (1 mm^3 isotropic voxel size) with magnetization transfer-, proton density- and T1-weighted contrasts (TR/α/number of echoes = 24.5 ms/6°/6, 24.5 ms/6°/8 and 24.5 ms/21°/8, respectively; Melie-Garcia et al., 2018) and a B1 mapping scan as described in (Lutti et al., 2012); a 2D EPI scan (2 mm^3 isotropic voxel size) with 118 diffusion-encoding directions (15 at $b = 650$ s/mm^2, 30 at $b = 1000$ s/mm^2, 60 at $b = 2000$ s/mm^2 and 13 at $b = 0$ s/mm^2 interleaved through the acquisition; Slater et al., 2019).

2.3.2 | Data processing

A full description of the data analysis can be found in Oliveira et al., 2022. Freesurfer (Fischl, 2012) was used to delineate the occipital ROI from the MPRAGE images (defined in Section 2.2.3). We performed whole-brain anatomically constrained tractography analyses of the diffusion data with the iFOD2 algorithm of mrTrix (Tournier et al., 2019). Twenty million streamlines were generated, from 5 to 250 mm in length, and cropped at the gray-white matter interface. The SIFT2 algorithm of mrTrix was subsequently applied to improve the biological accuracy of the streamline reconstruction (Smith et al., 2015). We then delineated the tract of interest by selecting the streamlines that connected the occipital ROI of the two brain hemispheres and crossed the corpus callosum.

MTsat maps were calculated from the magnetization transfer-, proton density-, and T1-weighted images with the hMRI toolbox (Tabelow et al., 2019), as described by Helms, Dathe, and Dechent (2008) and Helms, Dathe, Kallenberg, and Dechent (2008). Eddy current effects in the diffusion data were corrected with FSL (Andersson & Sotiropoulos, 2016) and image distortions were corrected using the fieldmap toolbox of SPM (Hutton et al., 2002). The NODDI model (Zhang et al., 2012) was fitted to the preprocessed diffusion data with the AMICO toolbox (Daducci et al., 2015), leading to maps of the isotropic diffusion (v_{iso}) and intracellular (v_{ic}) compartment volume fractions.

Maps of gMRI were computed from maps of v_{iso} and v_{ic} obtained from the NODDI model and MTsat maps (Stikov et al., 2015): $\text{gMRI} = \sqrt{1/\left(1+\frac{\alpha MTsat}{(1-\alpha MTsat)\,(1-v_{iso})v_{ic}}\right)}$. The value of α ($\alpha = .23$) was taken from Slater et al., 2019, who estimated this factor using MRI data from 11 subjects assumed to show minimal variability. This data was acquired with a protocol identical to the current study. The MRI-measured g-ratio maps were sampled along the white matter transcallosal tract delineated with diffusion MRI tractography.

2.4 | Axonal morphology analysis

The IHTT values were averaged between the measures obtained from the CDs in each experimental condition (LVF and RVF). Estimates of axonal conduction velocity were computed by dividing the length of the transcallosal white matter tract in each dataset by the corresponding estimate of IHTT. Subsequently, the measures of gMRI and conduction velocity were used to estimate morphological properties of axons in the transcallosal white matter tract using the model proposed in Oliveira et al., 2022. The axonal morphological properties included:

- the scale parameter θ of the distribution of axonal radius $P(r)$, where $P(r)$ is taken as a gamma distribution: $P(r) = \frac{1}{\Gamma(\frac{M}{\theta}+1)\theta^{\frac{M}{\theta}+1}} r^{\frac{M}{\theta}} e^{\frac{-r}{\theta}}$, r is the axonal radius and M is the mode of the distribution. An increasing value of θ indicates a broader spread of $P(r)$ into large radius values.
- the scaling factor β of the dependence of the axonal g-ratio on axonal radius: $g(r) = \beta \times r^{\alpha}$.

Previous work has shown that a 10% bias of the estimate of the mode M of the axonal radius distribution leads to a moderate bias in the estimated parameters θ (∼22%) and β (1%) (Oliveira et al., 2022). Also, M has been reported to be largely constant across white matter tracts and even animal species (Liewald et al., 2014; Tomasi et al., 2012). Thus the model parameters α and M were set to 0.14 and 0.30 µm, respectively, in agreement with histological studies (Liewald et al., 2014; Tomasi et al., 2012).

The specificity of the θ and β estimates computed from each subject was assessed by comparing between-session variability and between-subject variability. Between-session variability was estimated as the mean absolute difference of the θ and β estimates between sessions. Between-subject variability was estimated as the standard deviation of the θ and β estimates across the 14 datasets of the first session.

3 | RESULTS

3.1 | Group IHTT estimation

Group-averaged CD waveforms exhibit a sharp increase compared to the baseline activity starting at approximately 115 ms post-stimulus onset (Figure 1). This increase is first observed in the hemisphere contralateral to the visual stimulation—right hemisphere (red line in Figure 1) for LVF stimulations—and later in the ipsilateral hemisphere—left hemisphere (blue line in Figure 1) for LVF stimulations. These results confirm our assumptions on the expected pattern of neuronal activations, that is, a response of the hemisphere directly stimulated (direct pathway) occurring earlier than the opposite one (indirect pathway). The group-averaged estimates of IHTT were 11 and 19 ms for the LVF and RVF, respectively.

3.2 | Subject-specific IHTT estimation

Similarly to the group CD waveforms (Figure 1), the time course of the individual original CD waveforms typically exhibit a first peak in the contralateral hemisphere, followed by a peak in the ipsilateral hemisphere (solid lines in Figure 2a,b). The same peak latencies are identified by the CD waveforms masked with the results of the cluster permutation statistical analysis, indicating that these peaks lie within the period of the stimulus-evoked activity (dashed lines in Figure 2a,b). The latency of the peaks on the CD waveforms are consistent with the latencies of the ERP component N1 (∼120–210 ms) as observed in the GFP waveforms of the corresponding ERPs (Figure 2c,d). The cluster permutation identifies clusters of activation that increase in size with time. The clusters on the contralateral and ipsilateral hemispheres show a time-lag between them and the maximum peaks of activation lie within the period of analysis (100–250 ms) (Figure 2e,f). The latencies of the maximum number of activation vertices in each hemisphere approximately correspond to the latencies of the peaks seen on the CD waveforms. The results for the remaining subjects can be found in Figure S2.

Table 1 shows the IHTT estimated from the original CDs, the CDs waveforms masked with the significant clusters, and the time course

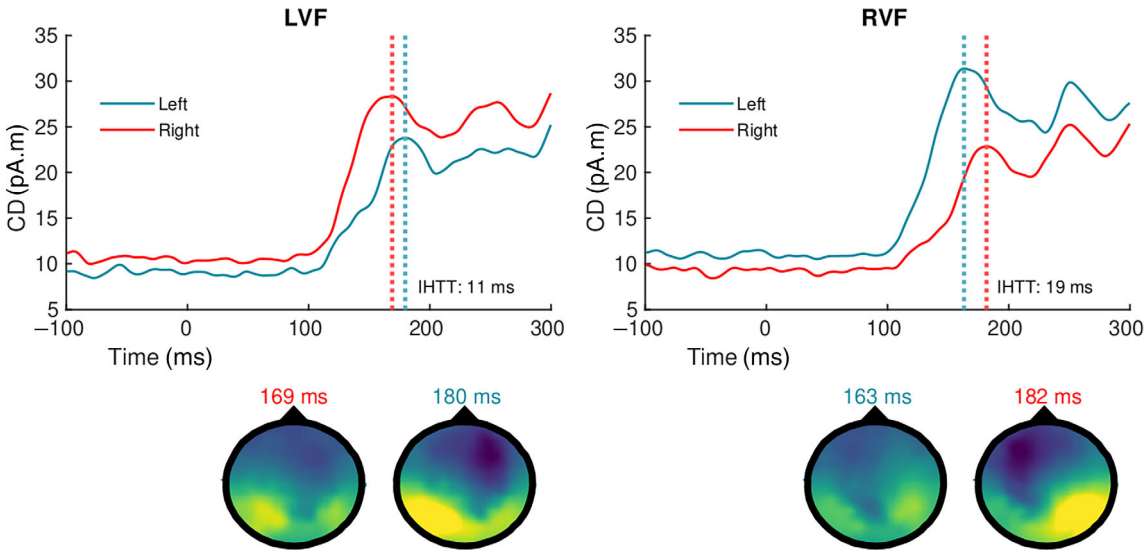

FIGURE 1 Group averaged CD for the LVF (left) and RVF (right) conditions. Stimulus onset took place at $t = 0$ ms. The CDs inside the occipital ROI on the left and right hemispheres are depicted in blue and red lines, respectively. The peaks of activation in each hemisphere are shown by the vertical dashed lines. Voltage topographies maps are shown for the time points corresponding to the identified peaks.

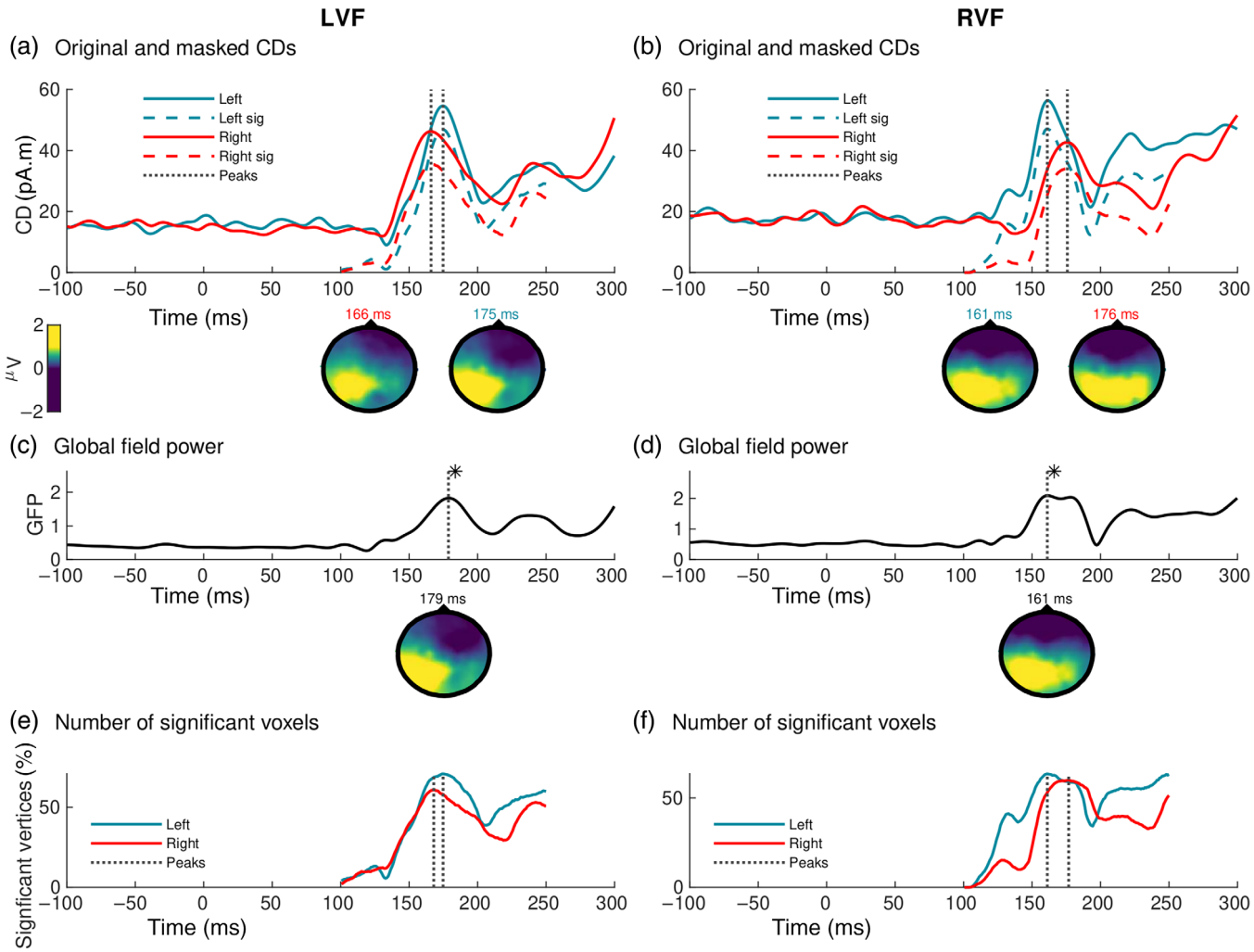

FIGURE 2 Summary of the IHTT estimation in an exemplar participant. (a, b) CD waveforms for one example subject for both visual conditions (LVF and RVF). The original CDs inside the occipital ROI on the left and right hemispheres are depicted with blue and red solid lines, respectively. The masked CDs in the same ROI on the left and right hemispheres are shown in the blue and red dashed lines, respectively. The vertical dashed lines indicate the peaks in each hemisphere, identified from the original CDs. The voltage topographies correspond to those identified peaks. (c,d) Global field power time course and topographies corresponding to the main components. The * identifies the component closest to the first peak identified in (a, b). (e, f) Number of significant voxels (percentage) in the post-stimulus period. Left and right hemispheres' timecourses are shown with blue and red lines, respectively. Vertical lines correspond to peaks. Time 0 ms identifies the onset of the stimulus for all the graphs.

of the number of vertices inside the significant clusters, for each subject and condition. A positive IHTT reflects a transfer in the direction predicted anatomically, where the response of the hemisphere directly stimulated (direct pathway) occurs earlier than the opposite one (indirect pathway). For the LVF, the estimated IHTT was in the direction predicted anatomically in 12 subjects out of 14 from the original CDs and the masked CDs, and in 10 subjects out of 14 from the significant number of vertices. For the RVF, IHTT was in the direction predicted anatomically in nine subjects out of 14 from the original CDs and the significant number of vertices and eight subjects out of 14 from the masked CDs. The mean IHTT across conditions from the original CDs ranged from 8 to 29 ms across participants (with a mean of 19 ms), excluding one participant with a negative IHTT of −25 ms.

The correlation coefficient of the IHTT estimates from the original CDs and masked CDs was .95, from the original CDs and number of voxels was .68, and between the masked CDs and number of voxels was .76. In all three cases, the correlation coefficient was significant ($p < .001$).

3.3 | Peak selection reliability

To identify unreliable IHTT estimates due to the presence of multiple peaks, we searched for a second peak with an amplitude within 5% of the global maximum (* in Table 1). For the LVF, unreliable IHTT estimates were found in two subjects from the original CDs or masked CDs and in five subjects from the significant number of vertices.

TABLE 1 Overview of the IHTT estimation at the single-subject level.

	Left visual field (LVF)				Right visual field (RVF)				Averaged conditions		
	Latency contralateral activation	Original CDs	Masked CDs	Number of vertices	Latency contralateral activation	Original CDs	Masked CDs	Number of vertices	Original CDs	Masked CDs	Number of vertices
S1	155	35	36	46*	155	22	23	29	**29**	30	38
S2	150	12	11	9	144	42	42	43*	**27**	26	26
S3	157	23*	−7*	−18*	172	5	4	6	**14**	−1	−6
S4	179	29*	31	−5*	159	−1	−1	7	**14**	15	1
S5	159	35	37*	−1	175	19	−7*	−13	**27**	15	−7
S6	187	2	4	9	141	56	57	13*	**29**	30	11
S7	159	36	35	32	194	−10	−11	−16*	**13**	12	8
S8	169	47	50	51*	179	−20	−21	−22*	**14**	15	15
S9	154	49	49	51	195	−13	−14	−8	**18**	18	22
S10	179	15	13	13*	143	25*	22*	20*	**20**	17	16
S11	195	13	15	14	193	21	22	16*	**17**	18	15
S12	193	−15	−15	−16	205	−35	−39	−38	**−25**	−27	−27
S13	166	9	7	7	161	15	15	16	**12**	11	11
S14	139	−1	0	44	172	18	18	20	**8**	9	32

Note: Latency contralateral activation refers to the contralateral peak latency as measured from the original CDs. IHTT estimates for the LVF and RVF with the three metrics for the 14 subjects and average across conditions. Highlighted in bold are the values of the IHTT used for the morphological estimates. * identifies the cases where the waveforms contained multiple peaks with amplitude values within 5% of the global maximum and therefore considered less reliable than the values without *. Time is always shown in ms.

Abbreviations: CDs, current densities; IHTT, interhemispheric transfer time.

Similarly for the RVF, unreliable IHTT estimates were found in one subject from the original CDs, in two subjects from the masked CDs, and in six subjects from the significant number of vertices. The IHTT estimated from the first and second highest peaks is detailed in Table S1. The mean absolute difference between the IHTT measured from the first and the second highest maximum of neuronal activity is 32 ms for the LVF and 26 ms for the RVF.

By considering the second-highest amplitude maximum on the CD waveforms, the disagreement between the metrics is often mitigated. This can be observed in the LVF of S3, where the IHTT obtained on original data is positive (23 ms, Figure 3a). The IHTT obtained on the masked data is negative and thus anatomically unplausible when obtained with the absolute maximum (−7 ms, Figure 3b) but when calculated with the second highest maximum is positive and in-line with the one obtained from the original data (24 ms, Figure 3c).

3.4 | IHTT within-session and between-session repeatability

In the assessment of within-session repeatability, the IHTT estimates from the first subset of trials showed moderate repeatability with the ones from the second subset of trials ($r = .68$, $p < .001$, Figure 4a). The mean IHTT absolute difference across the two subsets was ∼11 ms with some differences reaching up to 63 ms. The IHTT estimates obtained from each subset (circles in Figure 4b) differ from the IHTT value obtained from all the trials (horizontal lines in Figure 4b): the absolute differences between the mean IHTT across subsets and the IHTT obtained from all the trials are on average 6 ms for the LVF and 5 ms for the RVF.

In the assessment of between-session repeatability, the CD waveforms showed a high level of visual correspondence between repetitions (Figure 5). For the LVF, the IHTT was 12, 23, and 36 ms in the first session and 12, 17, and 20 ms in the second session. For the RVF, the IHTT was 42, 5, and −10 ms in the first session and 5, −1, and −7 ms in the second session. After averaging the IHTT estimated for the LVF and RVF conditions, the average difference in IHTT between sessions was 10 ms and the resulting difference in conduction velocity estimates was 11 m/s.

3.5 | Estimation of axonal morphology from the MRI and EEG data

The conduction velocities ranged from 4.7 to 18.5 m/s (excluding one negative conduction velocity not considered in subsequent analyses, Table 2). Mean gMRI values within the occipital transcallosal tract ranged from 0.67 to 0.71. The latter conduction velocities and gMRI estimates were used to estimate the parameter θ of the axonal radius distribution and the parameter β of the change in axonal g-ratio with axonal radius (Table 2). The average θ across

subjects was 0.23 μm and ranged from 0.00 to 0.79 μm (Table 2). Subject S1 was the only one with a value of θ near zero (<0.01 μm). The average β across subjects was 0.72 $\mu m^{-\alpha}$ ranging from 0.62 to 0.81 $\mu m^{-\alpha}$ (Table 2).

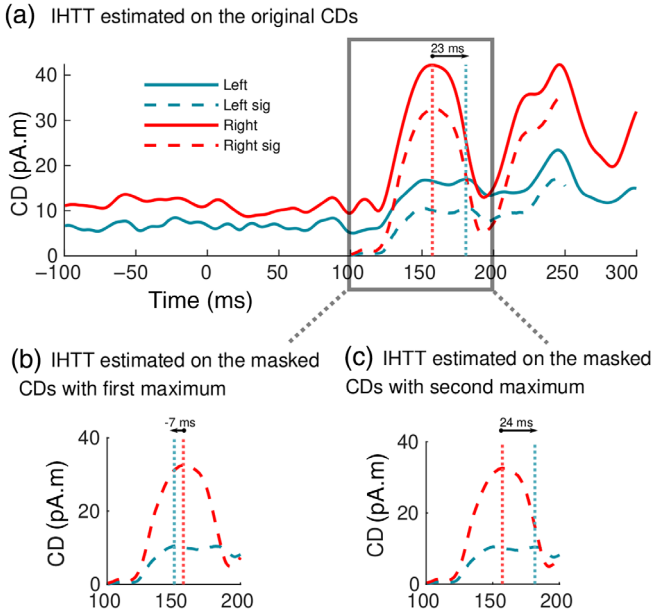

FIGURE 3 Example CD time courses showing multiple peaks with amplitude within 5% of the global maximum. (a) The original CDs in the occipital ROI of the left and right hemispheres are depicted with blue and red solid lines, respectively. The masked CDs from the same ROI are shown with blue and red dashed lines, respectively. Time 0 ms identifies the onset of the stimulus. The vertical dashed lines indicate the selected peaks in the original CDs. The estimated IHTT is 23 ms. (b) Zoom in on the masked CDs of (a). The vertical blue dashed line indicates the global maximum of the left hemisphere. The estimated IHTT is −7 ms. (c) Zoom in on the masked CDs of (a). The vertical blue dashed line indicates the second-highest amplitude peak in the left hemisphere. The estimated IHTT is 24 ms, in-line with the estimated IHTT on the original CDs shown in (a).

The between-subject variability of the model estimates was 0.22 μm and 0.06 $\mu m^{-\alpha}$ for θ and β respectively. A qualitative impression of the variability of θ and β is provided in Figure 6a and Figure 6b, respectively. For comparison, the between-session variability of θ and β was 0.57 μm and 0.11 $\mu m^{-\alpha}$, respectively. This is larger than between-subject variability and indicates low specificity of the axonal morphology estimates to each individual subject.

To further investigate the origin of the low specificity of the axonal morphology estimates, we plotted the values of θ (Figure 7a) and β (Figure 7b) obtained from subjects within the 2-dimensional space of possible combinations of conduction velocities and gMRI. Differences in θ of ∼0.8 are present across the range of conduction velocity estimates obtained experimentally, larger than the differences in θ values across the range of gMRI estimates (∼0.03). Similarly, the differences in the value of β are much larger across the range of conduction velocity estimates (∼0.2) than across the range of gMRI estimates (∼0.03). This finding shows that conduction velocity (rather than gMRI) is the primary determinant of the individual estimates of θ and β obtained from each dataset. Improving the specificity of the axonal morphology estimates, therefore, requires further improvements in the repeatability of the conduction velocity estimates. Moreover, supplementary analyses show that a 10% bias in conduction velocity leads to an average bias in θ of about 22% and an average bias in β of approximately 2% (Figure S3). These results highlight the importance of accurate conduction velocity estimates for the model estimates.

4 | DISCUSSION

In this work, we proposed a novel framework to estimate the IHTT at the single-subject level from EEG data, based on a data-driven evaluation of the maximal peak of neural response to visual stimuli with minimal a priori constraints. The resulting subject-specific estimates of IHTT were used to estimate morphological features of axons within the occipital transcallosal white matter tract, using a recently introduced biophysical model (Oliveira et al., 2022).

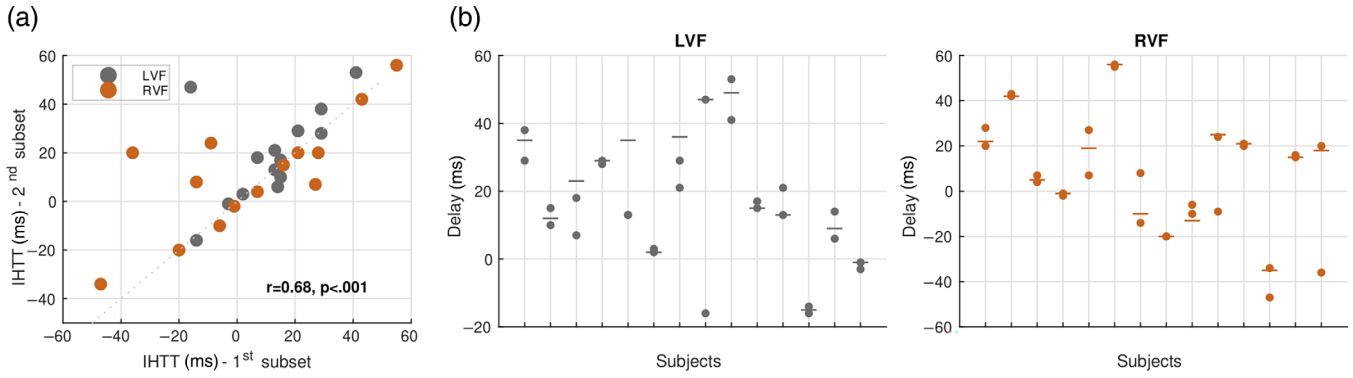

FIGURE 4 Within-session variability of the IHTT estimates. (a) IHTT estimates were obtained from two non-overlapping subsets of the trials for each subject and condition. There is a significant correlation ($r = .68$, $p < .001$) between the two subsets. (b) IHTT estimates obtained from the two non-overlapping subsets of the trials (circles) and IHTT estimates from all the trials (horizontal lines) for each participant and condition. The mean absolute difference between the latter and the mean IHTT across subsets was on average 6 ms for the LVF and 5 ms for the RVF.

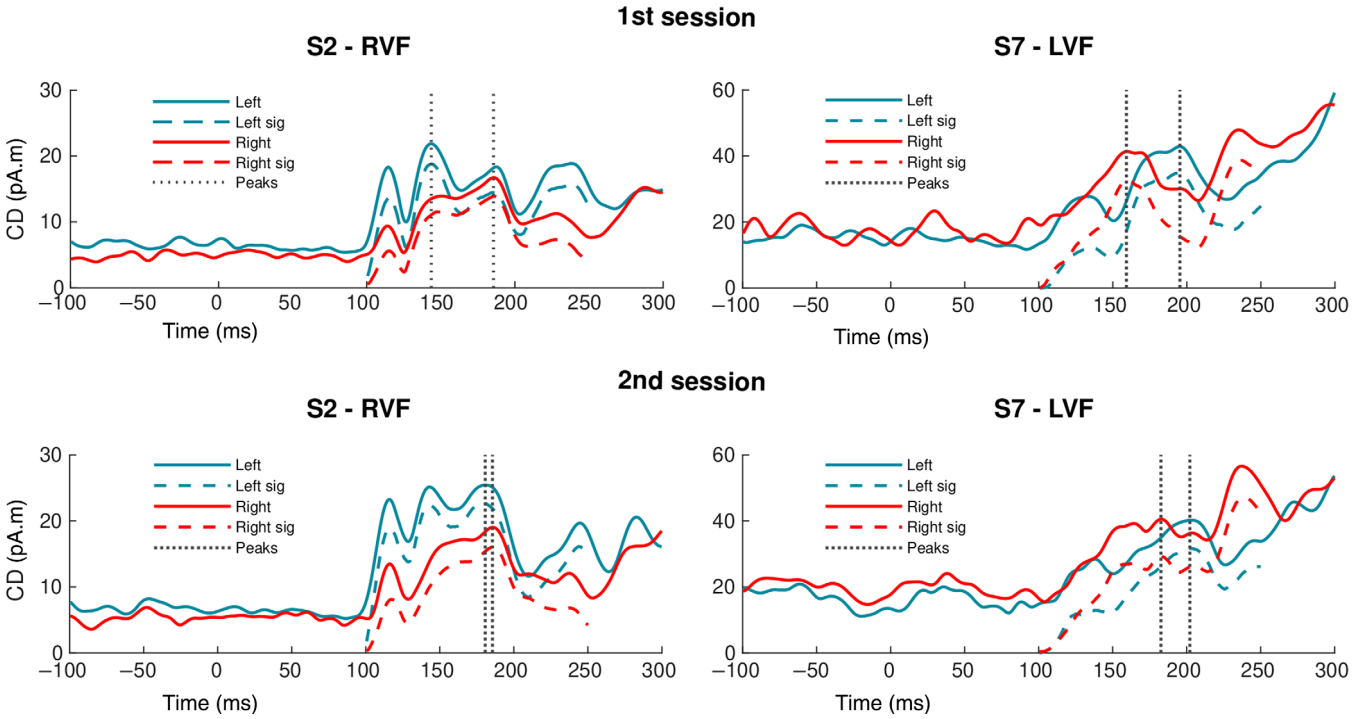

FIGURE 5 CD waveforms obtained in two separate sessions from subjects S2 (RVF) and S7 (LVF). The original CDs from the occipital ROI in the left and right hemispheres are depicted with blue and red solid lines, respectively. The masked CDs from the same ROI are shown with the blue and red dashed lines. The vertical dashed lines indicate the selected peaks for each hemisphere from the original data. Time 0 ms identifies the onset of the stimulus for all the graphs.

TABLE 2 Final IHTT estimates averaged across conditions for the 14 subjects (ms). Length of the white matter tract (mm). Conduction velocity along the white matter tract (m/s). Estimated θ (μm) and β ($\mu m^{-\alpha}$) for each subject.

	IHTT estimated from original CDs (ms)	Length (mm)	Velocity (m/s)	θ (μm)	β ($\mu m^{-\alpha}$)
S1	29	136.5	4.7	0.00	0.81
S2	27	134.6	5.0	0.02	0.81
S3	14	127.7	9.1	0.26	0.71
S4	14	133.6	9.5	0.27	0.69
S5	27	149.0	5.5	0.03	0.77
S6	29	147.3	5.1	0.01	0.79
S7	13	143.9	11.1	0.38	0.69
S8	14	136.3	9.7	0.29	0.70
S9	18	141.6	7.9	0.18	0.72
S10	20	135.4	6.8	0.11	0.74
S11	17	155.8	9.2	0.25	0.70
S12	−25	155.6	−6.2	–	–
S13	12	154.2	12.9	0.46	0.65
S14	8	147.8	18.5	0.79	0.62

Abbreviations: CDs, current densities; IHTT, interhemispheric transfer time.

The proposed framework relies on the estimation of the neural activity in the source space. This avoids the ad hoc selection of electrodes and ERP components at the electrode level and overcomes ambiguities related to the undetermined relation between voltage measurements at the scalp and those of the underlying and neurophysiologically interpretable electric fields (Nunez & Srinivasan, 2009). The subject-specific IHTT estimates are in agreement with the literature (average = 18.6 ms), except for one negative value. From the values of the IHTT, the scale parameter of the axonal radius distribution (θ), was estimated as 0.23 μm on average across

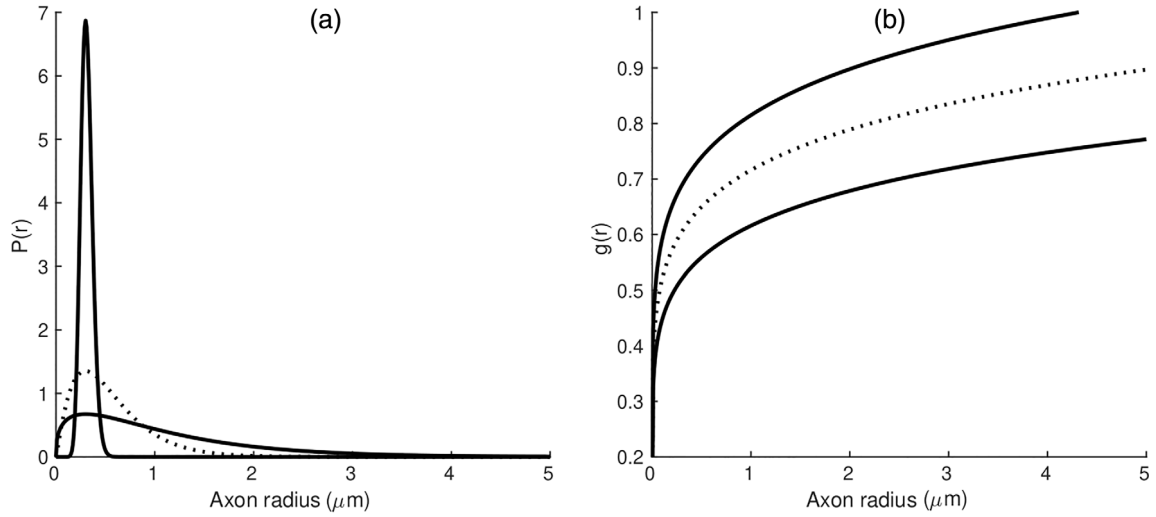

FIGURE 6 (a) Axonal radius distribution $P(r)$ computed from the minimum, maximum (solid lines), and average (dashed line) values of the scale parameter θ. (b) Axonal g-ratio ($g(r)$), computed from the minimum, maximum (solid lines), and average (dashed line) values of the scaling factor β.

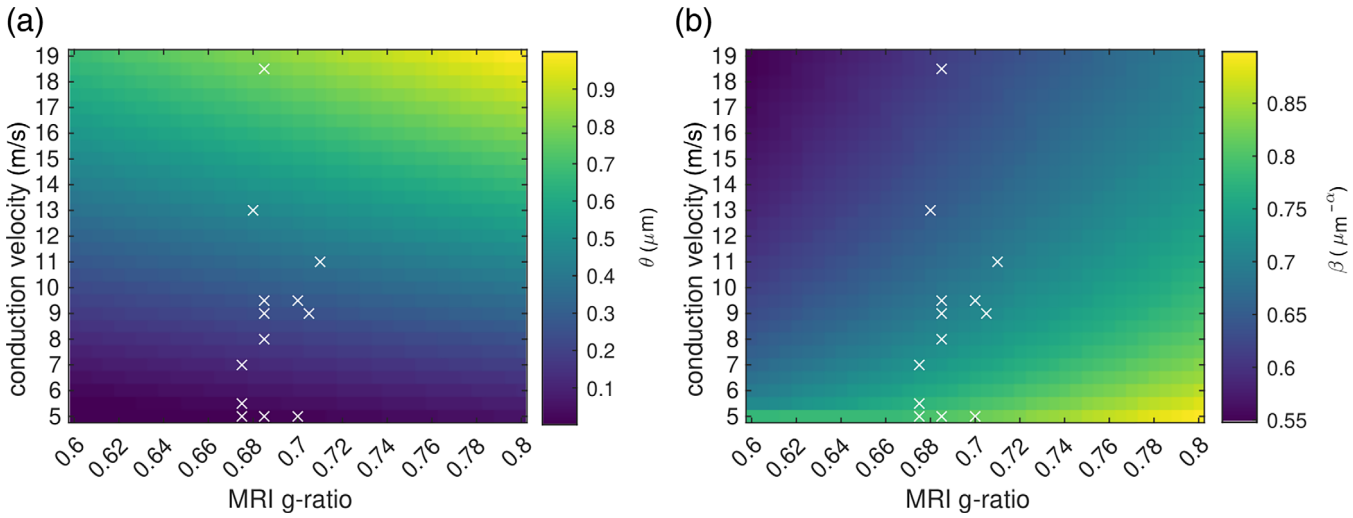

FIGURE 7 Value of the model parameters θ (a) and β (b) computed from combinations of simulated in vivo MRI g-ratio and conduction velocities. The crosses indicate the individual MRI g-ratio and conduction velocities estimates obtained experimentally from each subject. The conduction velocities, rather than gMRI, are the primary determinant of the values of θ and β. As a result, the variability of the conduction velocity estimates drives the specificity of the θ and β estimates obtained from each subject.

subjects, corresponding to a mean axonal radius of 0.53 µm. The amplitude of the change in axonal g-ratio with axonal radius (β) is 0.72 $\mu m^{-\alpha}$ on average across subjects. These estimates are consistent with histology findings obtained from ex-vivo data (Caminiti et al., 2009; Jung et al., 2018).

4.1 | IHTT measures

The IHTT estimates obtained from the original CDs at the group level are consistent with previous literature (Chaumillon et al., 2018; Friedrich et al., 2017; Saron & Davidson, 1989). Moreover, faster right-to-left transfer (i.e. LVF, 11 ms) than left-to-right transfer (i.e. RVF, 19 ms) is consistent with previous findings in right-hand dominated cohorts (Chaumillon et al., 2018; Martin et al., 2007; Marzi et al., 1991; Moes et al., 2007; Whitford et al., 2011).

As for the subject-specific estimates, the mean IHTT across the two visual conditions (LVF and RVF) ranged from 8 to 29 ms across participants – excluding one participant with a negative IHTT of −25 ms (Table 1). These results are in agreement with the few electrode-based studies that report subject-specific IHTT values (Chaumillon et al., 2018; Friedrich et al., 2017; Westerhausen et al., 2006). Our range of estimated IHTT is also in-line with the delays estimated with intracranial recordings from whole-brain cortical–cortical connections (Lemarechal et al., 2022).

The reliability of the subject-specific measures of IHTT was assessed by estimating the consistency of the IHTT estimates across different metrics (the original CDs, masked CDs, and number of significant vertices), two of them computed from a statistical analysis to ensure that neuronal activity was due to the evoked activity in response to the visual stimuli. The correlation coefficients between two pairs of metrics were above 0.68 and significant ($p < .001$) in all cases. The overall agreement between the three metrics confirms the origin of the estimated IHTT on the original CDs as the result of a stimulus-elicited activity.

Analysis of the repeatability of the IHTT estimates within-session (Figure 4a), conducted from non-overlapping subsets of trials for each participant, showed moderate repeatability ($r = .68$, $p < .001$). The average variability in IHTT within-session was 11 ms, approximately half of the mean IHTT across subjects. The between-session repeatability, analyzed on a subgroup of 3 participants, shows a weak linear relationship between the IHTT estimated on two different sessions. After averaging the IHTT estimated for the LVF and RVF conditions, the average variability between sessions was 10 ms. This is comparable to within-session variability despite contributions from environmental or contextual factors such as activation strength and attentional resource allocations (Nishimoto et al., 2020).

The variability of the IHTT estimates between sessions was also comparable to the differences in IHTT estimates between subjects (7 ms), highlighting the low specificity of the IHTT estimates to each participant. Nevertheless, the pattern of neuronal activity is qualitatively reproducible across sessions (Figure 5). This result suggests that peaks of maximal activation might be insufficient to estimate the IHTT. Other approaches, such as transfer entropy (Vicente et al., 2011) or mutual information (Ince et al., 2017) could be considered as future alternatives at the expense of a high number of parameters and assumptions. Confidence intervals on the IHTT values for each subject could also be estimated with a bootstrapping approach, by sampling the delays from the subject's trial data with replacement (Cichy et al., 2014).

4.2 | Subject-specific neuronal activity

At the single-subject level, only one subject (S12) did not fulfill our expected patterns of activity—i.e. increase in activation in the contralateral hemisphere prior to the ipsilateral hemisphere—and thus has negative IHTT in both visual conditions. The reason for this remains unclear. We postulate that the simple process that we assume to describe the visual transfer (peak in one hemisphere and then transfer to the other hemisphere) might be too simplistic. For instance, multiple transfers might occur within a short period (Deslauriers-Gauthier et al., 2019). Also, undeniably, rather than a single IHTT value, there exists a distribution of delays due to the underlying axonal radius distribution (Caminiti et al., 2013).

While the peaks of maximal neuronal response are very evident in the group CD waveforms (Figure 1), the same is not always true for the individual data. Variability in the latencies and topographies of the neuronal response, and in the cortical anatomy across subjects has been extensively reported (Baumgartner et al., 2018; Foxe & Simpson, 2002; Proverbio et al., 2007). Hence, understanding the specific dynamics of each individual data (Figure S2) is fundamental when analyzing the data-driven IHTT estimates. In particular, the presence of multiple peaks with analogous amplitudes on the waveforms hinders the IHTT estimation. If we take such cases into account (Table S1), the overall agreement between IHTT metrics is even more evident. These results support the existence of a subject-specific neuronal response, the difficulty being in the definition of a robust metric to extract IHTT from the CD time courses that is consistent across subjects and requires a minimal set of assumptions.

The presence of multiple peaks in at least two of the metrics was observed in three cases (the LVF of S3 (Figure 3a), RVF of S10, and LVF of S4). For these participants, two possible IHTT estimates exist for all three metrics, with only one of the two options being anatomically plausible (i.e. positive IHTT). For example, the LVF IHTT of S3 may be 23, 24, and 23 ms or − 5, −7, and − 18 ms from the original CDs, masked CDs, and number of significant vertices, and no objective metric exists to guide the choice of a maximum. Because our expected pattern of activity is a contralateral peak occurring before the ipsilateral one (positive IHTT), we could potentially impose an extra constraint on the positivity of the IHTT. However, that would diverge from a data-driven approach with minimal constraints which we are proposing here.

In the absence of a more specific measure, we used the IHTT as a proxy for the conduction time of axon potentials along white matter axons. However, synaptic transfer and signal conduction within the gray matter contribute to the measured IHTT, leading to an overestimation of the conduction time with this approach. The magnitude of this confound is challenging to estimate. In principle, generative models of the effect of gray matter dynamics on the current density curves may provide IHTT estimates with no contribution from gray matter. Another avenue would be to resolve the distribution of current densities across the cortical ribbon and estimate the IHTT from the white-gray matter interface. Unfortunately, both options remain out of reach.

We highlight that, unlike Oliveira et al., 2022, conduction velocities were measured from an average of the two experimental conditions (LVF and RVF). This allows for a more representative characterization of the white matter tract, independent of the direction of propagation of neurons.

In summary, we use a simple assumption for the pattern of interhemispheric transfer, with minimal constraints to obtain single-subject IHTT estimates. We showed that with our approach, estimating the subject-specific IHTT based on the original CDs is associated with some level of uncertainty due to the presence of peaks with similar amplitudes in only 3 out of 28 cases (Section 3.3). In any case, for these 3 cases, the maximum peak, which is the one we chose by default, is the one providing an IHTT in the direction predicted anatomically. The IHTT based on the original CDs is also supported by the other two metrics obtained from statistical analysis, ensuring that neuronal activity was due to the evoked activity in response to the

visual stimuli. Additionally, the agreement of the IHTT estimates with the literature is compelling.

4.3 | Subject-specific axonal morphologic estimates

The scale parameter θ of the axonal radius distribution within a white matter tract ranged from 0.00 to 0.79 µm (Figure 6a). The parameter β, which represents the amplitude of the change in axonal g-ratio with axonal radius, ranged from 0.62 to 0.81 $\mu m^{-\alpha}$ (Figure 6b). The mean value of the scale parameter θ across subjects was 0.23 µm. This corresponds to an average radius of 0.53 µm, in-line with previous estimates from histological studies (0.62 µm; Caminiti et al., 2009). For such value of θ, axons above 2.5 µm represent <0.04% of the total fiber count. This is consistent with previous histological findings showing that these axons represent <0.02% of the total fiber count across the corpus callosum (Aboitiz et al., 1992) and more generally, that the maximum axonal radius in the human brain is ~1.5–3 µm (Aboitiz et al., 1992; Caminiti et al., 2009; Liewald et al., 2014).

The cornerstone of the proposed white matter model is that the structural (MRI g-ratio) and functional (conduction velocity) measures originate from the same white matter tract: the MRI g-ratio values are sampled along this tract and the IHTT estimates are divided by the tract's length used to compute the conduction velocity. The extent of evoked activity from primary to high-order visual areas in response to visual stimulation may imply the involvement of multiple white matter tracts for interhemispheric transfer. As these tracts remain undefined, the tract length was chosen as the mean length of the streamlines that connect the occipital regions across both hemispheres. This tract is 12 mm (8%) smaller than the tract that connects the primary and secondary visual cortices used in our previous study (Oliveira et al., 2022). Differences in gMRI values between these tracts were minimal (<1%).

4.4 | Future directions

This study focuses on the single-subject measurement of the IHTT, which is essential to the assessment of axonal morphology in-vivo in separate individuals. The consistency of the axonal radius and myelination estimates with the histological literature highlights the long-term potential of this technique. However, we found that the variability of the morphological estimates between repetitions was in the order of—or larger than—the difference of these estimates between subjects. Our results suggest that the measurement of the IHTT is the primary source of variability in the estimates of axonal morphology. Increasing the reproducibility of the IHTT estimates may be achieved by considering other source reconstruction methods, alternative metrics for IHTT estimation from the CD time course, or different EEG paradigms with a focus on other tracts. Alternative techniques, such as the newly proposed approach for single-subject and single-tract IHTT estimation, based on resting-state EEG data (Sorrentino et al., 2022) should also be considered. Moreover, our parsimonious approach to IHTT estimation from the current source densities could be improved by the usage of PCA or ICA methods (Barbati et al., 2008; Debener et al., 2005; Porcaro et al., 2010) to enhance source separation of relevant signals, at the expense of a strong hypothesis on the response of the investigated phenomenon. Comparison of EEG-based IHTT estimates with intracranial recordings of local field potentials and histological measures are essential to ensure their validity as in-vivo measures of axonal conduction velocity.

5 | CONCLUSIONS

This work represents the first attempt to estimate morphological properties of white matter axons from combined MRI and EEG data acquired in-vivo in individual subjects. In particular, we propose a new data-driven framework with minimal a priori constraints that allows the single-subject measurement of the IHTT from EEG data, based on the maximal peak of neural response upon visual stimulation. This framework provides evidence that the IHTT estimates are the result of activity elicited by the visual stimulus. The estimated IHTT values are in the reported range of electrode-based and intracranial EEG studies (Chaumillon et al., 2018; Friedrich et al., 2017; Lemarechal et al., 2022; Saron & Davidson, 1989). The MRI data and EEG-based measures of the IHTT were used to estimate morphological properties of white matter axons. The agreement of the estimates of axonal radius and myelination with the histological literature highlights the long-term potential of this technique. However, these morphological estimates showed a high level of variability that arises primarily from the estimation of the IHTT. Increasing the repeatability of the IHTT estimates and comparison with alternative measures of conduction velocity are essential future steps toward the measurement of axonal morphological properties from in-vivo data.

ACKNOWLEDGMENTS

The MRI data were acquired on the MRI platform of the Clinical Neuroscience Department, Lausanne University Hospital. We thank all technicians involved in the data collection and researchers Andria Pelentritou, Giulia Di Domenicantonio, and Quentin Raynaud for their invaluable help with EEG and MRI recordings and insightful discussions.

CONFLICT OF INTEREST STATEMENT

The authors declare no conflict of interest.

DATA AVAILABILITY STATEMENT

The data that support the findings of this study are openly available in Zenodo at: https://doi.org/10.5281/zenodo.7446009, reference number 7446009.

ORCID

Rita Oliveira https://orcid.org/0000-0002-7597-6919
Marzia De Lucia https://orcid.org/0000-0001-8792-7885
Antoine Lutti https://orcid.org/0000-0003-3281-5477

REFERENCES

Aboitiz, F., Scheibel, A. B., Fisher, R. S., & Zaidel, E. (1992). Fiber composition of the human corpus callosum. *Brain Research*, *598*, 143–153. https://doi.org/10.1016/0006-8993(92)90178-C

Alexander, D. C., Hubbard, P. L., Hall, M. G., Moore, E. A., Ptito, M., Parker, G. J. M., & Dyrby, T. B. (2010). Orientationally invariant indices of axon diameter and density from diffusion MRI. *NeuroImage*, *52*, 1374–1389. https://doi.org/10.1016/j.neuroimage.2010.05.043

Andersson, J. L. R., & Sotiropoulos, S. N. (2016). An integrated approach to correction for off-resonance effects and subject movement in diffusion MR imaging. *NeuroImage*, *125*, 1063–1078. https://doi.org/10.1016/j.neuroimage.2015.10.019

Assaf, Y., Blumenfeld-Katzir, T., Yovel, Y., & Basser, P. J. (2008). AxCaliber: A method for measuring axon diameter distribution from diffusion MRI. *Magnetic Resonance in Medicine*, *59*, 1347–1354. https://doi.org/10.1002/mrm.21577

Barakovic, M., Girard, G., Schiavi, S., Romascano, D., Descoteaux, M., Granziera, C., Jones, D. K., Innocenti, G. M., Thiran, J. P., & Daducci, A. (2021). Bundle-specific axon diameter index as a new contrast to differentiate white matter tracts. *Frontiers in Neuroscience*, *15*, 1–13. https://doi.org/10.3389/fnins.2021.646034

Barbati, G., Porcaro, C., Hadjipapas, A., Adjamian, P., Pizzella, V., Romani, G. L., Seri, S., Tecchio, F., & Barnes, G. R. (2008). Functional source separation applied to induced visual gamma activity. *Human Brain Mapping*, *29*, 131–141. https://doi.org/10.1002/hbm.20375

Baumgartner, H. M., Graulty, C. J., Hillyard, S. A., & Pitts, M. A. (2018). Does spatial attention modulate the earliest component of the visual evoked potential? *Cognitive Neuroscience*, *9*, 4–19. https://doi.org/10.1080/17588928.2017.1333490

Bell, A. J., & Sejnowski, T. J. (1995). An information-maximization approach to blind separation and blind deconvolution. *Neural Computation*, *7*, 1129–1159. https://doi.org/10.1162/neco.1995.7.6.1129

Benjamini, D., Komlosh, M. E., Basser, P. J., & Nevo, U. (2014). Nonparametric pore size distribution using d-PFG: Comparison to s-PFG and migration to MRI. *Journal of Magnetic Resonance*, *246*, 36–45. https://doi.org/10.1016/j.jmr.2014.06.017

Berman, S., Filo, S., & Mezer, A. A. (2019). Modeling conduction delays in the corpus callosum using MRI-measured g-ratio. *NeuroImage*, *195*, 128–139. https://doi.org/10.1016/j.neuroimage.2019.03.025

Brown, W. S., & Jeeves, M. A. (1993). Bilateral visual field processing and evoked potential interhemispheric transmission time. *Neuropsychologia*, *31*, 1267–1281. https://doi.org/10.1016/0028-3932(93)90097-J

Brown, W. S., Larson, E. B., & Jeeves, M. A. (1994). Directional asymmetries in interhemispheric transmission time: Evidence from visual evoked potentials. *Neuropsychologia*, *32*, 439–448. https://doi.org/10.1016/0028-3932(94)90089-2

Caminiti, R., Carducci, F., Piervincenzi, C., Battaglia-Mayer, A., Confalone, G., Visco-Comandini, F., Pantano, P., & Innocenti, G. M. (2013). Diameter, length, speed, and conduction delay of callosal axons in macaque monkeys and humans: Comparing data from histology and magnetic resonance imaging diffusion tractography. *The Journal of Neuroscience*, *33*, 14501–14511. https://doi.org/10.1523/JNEUROSCI.0761-13.2013

Caminiti, R., Ghaziri, H., Galuske, R., Hof, P. R., & Innocenti, G. M. (2009). Evolution amplified processing with temporally dispersed slow neuronal connectivity in primates. *PNAS*, *106*, 19551–19556. https://doi.org/10.1073/pnas.0907655106

Campbell, J. S. W., Leppert, I. R., Narayanan, S., Boudreau, M., Duval, T., Cohen-Adad, J., Pike, G. B., & Stikov, N. (2018). Promise and pitfalls of g-ratio estimation with MRI. *NeuroImage*, *182*, 80–96. https://doi.org/10.1016/j.neuroimage.2017.08.038

Chaumillon, R., Blouin, J., & Guillaume, A. (2018). Interhemispheric transfer time asymmetry of visual information depends on eye dominance: An electrophysiological study. *Frontiers in Neuroscience*, *12*, 1–19. https://doi.org/10.3389/fnins.2018.00072

Cichy, R. M., Pantazis, D., & Oliva, A. (2014). Resolving human object recognition in space and time. *Nature Neuroscience*, *17*, 455–462. https://doi.org/10.1038/nn.3635

Cluskey, S., & Ramsden, D. B. (2001). Mechanisms of neurodegeneration in amyotrophic lateral sclerosis. *Molecular Pathology*, *54*, 386–392. https://doi.org/10.1136/mp.54.6.386

Creel, D. (2012). Visually evoked potentials. In *The organization of the retina and visual system*. Salt Lake City, UT: University of Utah Health Sciences Center. https://doi.org/10.1007/978-3-030-30417-1_2

Cuffin, B. N. (1998). EEG dipole source localization: Using inverse solutions for determining source locations. *IEEE Engineering in Medicine and Biology Magazine*, *17*, 118–122. https://doi.org/10.1109/51.715495

Daducci, A., Canales-Rodríguez, E. J., Zhang, H., Dyrby, T. B., Alexander, D. C., & Thiran, J. P. (2015). Accelerated Microstructure Imaging via Convex Optimization (AMICO) from diffusion MRI data. *NeuroImage*, *105*, 32–44. https://doi.org/10.1016/j.neuroimage.2014.10.026

Debener, S., Makeig, S., Delorme, A., & Engel, A. K. (2005). What is novel in the novelty oddball paradigm? Functional significance of the novelty P3 event-related potential as revealed by independent component analysis. *Cognitive Brain Research*, *22*, 309–321. https://doi.org/10.1016/j.cogbrainres.2004.09.006

Delorme, A., & Makeig, S. (2004). EEGLAB: An open source toolbox for analysis of single-trial EEG dynamics including independent component analysis. *Journal of Neuroscience Methods*, *134*, 9–21. https://doi.org/10.1016/j.jneumeth.2003.10.009

Desikan, R. S., Se, F., Fischl, B., Quinn, B. T., Dickerson, B. C., Blacker, D., Buckner, R. L., Dale, A. M., Maguire, R. P., Hyman, B. T., Albert, M. S., & Killiany, R. J. (2006). An automated labeling system for subdividing the human cerebral cortex on MRI scans into gyral based regions of interest. *NeuroImage*, *31*, 968–980. https://doi.org/10.1016/j.neuroimage.2006.01.021

Deslauriers-Gauthier, S., Lina, J. M., Butler, R., Whittingstall, K., Gilbert, G., Bernier, P. M., Deriche, R., & Descoteaux, M. (2019). White matter information flow mapping from diffusion MRI and EEG. *NeuroImage*, *201*, 116017. https://doi.org/10.1016/j.neuroimage.2019.116017

Di Russo, F., Martínez, A., Sereno, M. I., Pitzalis, S., & Hillyard, S. A. (2001). Cortical sources of the early components of the visual evoked potential. *Human Brain Mapping*, *15*, 95–111. https://doi.org/10.1002/hbm.10010

Does, M. D. (2018). Inferring brain tissue composition and microstructure via MR relaxometry. *NeuroImage*, *182*, 136–148. https://doi.org/10.1016/j.neuroimage.2017.12.087

Drobnjak, I., Zhang, H., Ianuș, A., Kaden, E., & Alexander, D. C. (2016). PGSE, OGSE, and sensitivity to axon diameter in diffusion MRI: Insight from a simulation study. *Magnetic Resonance in Medicine*, *75*, 688–700. https://doi.org/10.1002/mrm.25631

Evangelou, N., Konz, D., Esiri, M. M., Smith, S., Palace, J., & Matthews, P. M. (2001). Size-selective neuronal changes in the anterior optic pathways suggest a differential susceptibility to injury in multiple sclerosis. *Brain*, *124*, 1813–1820. https://doi.org/10.1093/brain/124.9.1813

Fan, Q., Nummenmaa, A., Witzel, T., Ohringer, N., Tian, Q., Setsompop, K., Klawiter, E. C., Rosen, B. R., Wald, L. L., & Huang, S. Y. (2020). Axon diameter index estimation independent of fiber orientation distribution using high-gradient diffusion MRI. *NeuroImage*, *222*, 117197. https://doi.org/10.1016/j.neuroimage.2020.117197

Fendrich, R., Hutsler, J. J., & Gazzaniga, M. S. (2004). Visual and tactile interhemispheric transfer compared with the method of Poffenberger. *Experimental Brain Research*, *158*, 67–74. https://doi.org/10.1007/s00221-004-1873-6

Fischl, B. (2012). FreeSurfer. *Neuroimage*, *62*, 774–781. https://doi.org/10.1016/j.neuroimage.2012.01.021

Foxe, J. J., & Simpson, G. V. (2002). Flow of activation from V1 to frontal cortex in humans: A framework for defining "early" visual processing.

Experimental Brain Research, *142*, 139–150. https://doi.org/10.1007/s00221-001-0906-7

Friedrich, P., Ocklenburg, S., Mochalski, L., Schlüter, C., Güntürkün, O., & Genc, E. (2017). Long-term reliability of the visual EEG Poffenberger paradigm. *Behavioural Brain Research*, *330*, 85–91. https://doi.org/10.1016/j.bbr.2017.05.019

Gramfort, A., Papadopoulo, T., Olivi, E., & Clerc, M. (2010). OpenMEEG: Opensource software for quasistatic bioelectromagnetics. *Biomedical Engineering Online*, *9*, 45.

Grech, R., Cassar, T., Muscat, J., Camilleri, K. P., Fabri, S. G., Zervakis, M., Xanthopoulos, P., Sakkalis, V., & Vanrumste, B. (2008). Review on solving the inverse problem in EEG source analysis. *Journal of Neuroengineering and Rehabilitation*, *5*, 1–33. https://doi.org/10.1186/1743-0003-5-25

Hämäläinen, M. S., & Ilmoniemi, R. J. (1994). Interpreting magnetic fields of the brain: Minimum norm estimates. *Medical & Biological Engineering & Computing*, *32*, 35–42. https://doi.org/10.1007/BF02512476

Hamburger, H. L., & Michelle, M. A. G. (1991). Global field power measurement versus classical method in the determination of the latency of evoked potential components. *Brain Topography*, *3*, 391–396. https://doi.org/10.1007/BF01129642

Harkins, K. D., Beaulieu, C., Xu, J., Gore, J. C., & Does, M. D. (2021). A simple estimate of axon size with diffusion MRI. *NeuroImage*, *227*, 117619. https://doi.org/10.1016/j.neuroimage.2020.117619.A

Helms, G., Dathe, H., & Dechent, P. (2008). Quantitative FLASH MRI at 3T using a rational approximation of the Ernst equation. *Magnetic Resonance in Medicine*, *59*, 667–672. https://doi.org/10.1002/mrm.21542

Helms, G., Dathe, H., Kallenberg, K., & Dechent, P. (2008). High-resolution maps of magnetization transfer with inherent correction for RF inhomogeneity and T1 relaxation obtained from 3D FLASH MRI. *Magnetic Resonance in Medicine*, *60*, 1396–1407. https://doi.org/10.1002/mrm.21732

Horowitz, A., Barazany, D., Tavor, I., Bernstein, M., Yovel, G., & Assaf, Y. (2015). In vivo correlation between axon diameter and conduction velocity in the human brain. *Brain Structure & Function*, *220*, 1777–1788. https://doi.org/10.1007/s00429-014-0871-0

Huang, S. Y., Tian, Q., Fan, Q., Witzel, T., Wichtmann, B., McNab, J. A., Daniel Bireley, J., Machado, N., Klawiter, E. C., Mekkaoui, C., Wald, L. L., & Nummenmaa, A. (2020). High-gradient diffusion MRI reveals distinct estimates of axon diameter index within different white matter tracts in the in vivo human brain. *Brain Structure & Function*, *225*, 1277–1291. https://doi.org/10.1007/s00429-019-01961-2

Hutton, C., Bork, A., Josephs, O., Deichmann, R., Ashburner, J., & Turner, R. (2002). Image distortion correction in fMRI: A quantitative evaluation. *NeuroImage*, *16*, 217–240. https://doi.org/10.1006/nimg.2001.1054

Ince, R. A. A., Giordano, B. L., Kayser, C., Rousselet, G. A., Gross, J., & Schyns, P. G. (2017). A statistical framework for neuroimaging data analysis based on mutual information estimated via a gaussian copula. *Human Brain Mapping*, *38*, 1541–1573. https://doi.org/10.1002/hbm.23471

Ipata, A., Girelli, M., Miniussi, C., & Marzi, C. (1997). Interhemispheric transfer of visual information in humans: The role of different callosal channels. *Archives Italiennes de Biologie*, *135*, 169–182.

Jung, W., Lee, J., Shin, H. G., Nam, Y., Zhang, H., Oh, S. H., & Lee, J. (2018). Whole brain g-ratio mapping using myelin water imaging (MWI) and neurite orientation dispersion and density imaging (NODDI). *NeuroImage*, *182*, 379–388. https://doi.org/10.1016/j.neuroimage.2017.09.053

Kybic, J., Clerc, M., Abboud, T., Faugeras, O., Keriven, R., & Papadopoulo, T. (2005). A common formalism for the integral formulations of the forward EEG problem. *IEEE Transactions on Medical Imaging*, *24*, 12–28. https://doi.org/10.1109/TMI.2004.837363

Lemarechal, J. D., Jedynak, M., Trebaul, L., Boyer, A., Tadel, F., Bhattacharjee, M., Deman, P., Tuyisenge, V., Ayoubian, L., Hugues, E., Chanteloup-Forêt, B., Saubat, C., Zouglech, R., Mejia, G. C. R., Tourbier, S., Hagmann, P., Adam, C., Barba, C., Bartolomei, F., … F-TRACT consortium. (2022). A brain atlas of axonal and synaptic delays based on modelling of cortico-cortical evoked potentials. *Brain*, *145*, 1653–1667. https://doi.org/10.1093/brain/awab362

Liewald, D., Miller, R., Logothetis, N., Wagner, H. J., & Schüz, A. (2014). Distribution of axon diameters in cortical white matter: An electron-microscopic study on three human brains and a macaque. *Biological Cybernetics*, *108*, 541–557. https://doi.org/10.1007/s00422-014-0626-2

Lutti, A., Dick, F., Sereno, M. I., & Weiskopf, N. (2014). NeuroImage using high-resolution quantitative mapping of R1 as an index of cortical myelination. *NeuroImage*, *93*, 176–188. https://doi.org/10.1016/j.neuroimage.2013.06.005

Lutti, A., Stadler, J., Josephs, O., Windischberger, C., Speck, O., Bernarding, J., Hutton, C., & Weiskopf, N. (2012). Robust and fast whole brain mapping of the RF transmit field B1 at 7T. *PLoS One*, *7*, 1–7. https://doi.org/10.1371/journal.pone.0032379

MacKay, A. L., & Laule, C. (2016). Magnetic resonance of myelin water: An in vivo marker for myelin. *Brain Plasticity*, *2*, 71–91. https://doi.org/10.3233/bpl-160033

Mancini, M., Tian, Q., Fan, Q., Cercignani, M., & Huang, S. Y. (2021). Dissecting whole-brain conduction delays through MRI microstructural measures. *Brain Structure & Function*, *226*, 2651–2663. https://doi.org/10.1007/s00429-021-02358-w

Maris, E., & Oostenveld, R. (2007). Nonparametric statistical testing of EEG- and MEG-data. *Journal of Neuroscience Methods*, *164*, 177–190. https://doi.org/10.1016/j.jneumeth.2007.03.024

Martin, C. D., Thierry, G., Démonet, J. F., Roberts, M., & Nazir, T. (2007). ERP evidence for the split fovea theory. *Brain Research*, *1185*, 212–220. https://doi.org/10.1016/j.brainres.2007.09.049

Marzi, C. A., Bisiacchi, P., & Nicoletti, R. (1991). Is interhemispheric transfer of visuomotor information asymmetric? Evidence from a meta-analysis. *Neuropsychologia*, *29*, 1163–1177. https://doi.org/10.1016/0028-3932(91)90031-3

Melie-Garcia, L., Slater, D., Ruef, A., Sanabria-Diaz, G., Preisig, M., Kherif, F., Draganski, B., & Lutti, A. (2018). Networks of myelin covariance Lester. *Human Brain Mapping*, *39*, 1532–1554. https://doi.org/10.1002/hbm.23929

Miles, W. R. (1930). Ocular dominance in human adults. *The Journal of General Psychology*, *3*, 412–430. https://doi.org/10.1080/00221309.1930.9918218

Moes, P. E., Brown, W. S., & Minnema, M. T. (2007). Individual differences in interhemispheric transfer time (IHTT) as measured by event related potentials. *Neuropsychologia*, *45*, 2626–2630. https://doi.org/10.1016/j.neuropsychologia.2007.03.017

Mohammadi, S., & Callaghan, M. F. (2021). Towards in vivo g-ratio mapping using MRI: Unifying myelin and diffusion imaging. *Journal of Neuroscience Methods*, *348*, 108990. https://doi.org/10.1016/j.jneumeth.2020.108990

Nilsson, M., Lasič, S., Drobnjak, I., Topgaard, D., & Westin, C. F. (2017). Resolution limit of cylinder diameter estimation by diffusion MRI: The impact of gradient waveform and orientation dispersion. *NMR in Biomedicine*, *30*, 1–13. https://doi.org/10.1002/nbm.3711

Nishimoto, T., Higashi, H., Morioka, H., & Ishii, S. (2020). EEG-based personal identification method using unsupervised feature extraction and its robustness against intra-subject variability. *Journal of Neural Engineering*, *17*, 026007. https://doi.org/10.1088/1741-2552/ab6d89

Nunez, P. L., & Srinivasan, R. (2009). *Electric fields of the brain: The neurophysics of EEG*. Oxford University Press. https://doi.org/10.1093/acprof:oso/9780195050387.001.0001

Oldfield, R. C. (1971). The assessment and analysis of handedness: The Edinburgh inventory. *Neuropsychologia*, *9*, 97–113. https://doi.org/10.1016/0028-3932(71)90067-4

Oliveira, R., Pelentritou, A., Di Domenicantonio, G., De Lucia, M., & Lutti, A. (2022). In vivo estimation of axonal morphology from

magnetic resonance imaging and electroencephalography data. *Frontiers in Neuroscience*, *16*, 1–18. https://doi.org/10.3389/fnins.2022.874023

Oostenveld, R., Fries, P., Maris, E., & Schoffelen, J. M. (2011). FieldTrip: Open source software for advanced analysis of MEG, EEG, and invasive electrophysiological data. *Computational Intelligence and Neuroscience*, *2011*, 156869. https://doi.org/10.1155/2011/156869

Plomp, G., Michel, C. M., & Herzog, M. H. (2010). Electrical source dynamics in three functional localizer paradigms. *NeuroImage*, *53*, 257–267. https://doi.org/10.1016/j.neuroimage.2010.06.037

Porcaro, C., Ostwald, D., & Bagshaw, A. P. (2010). Functional source separation improves the quality of single trial visual evoked potentials recorded during concurrent EEG-fMRI. *NeuroImage*, *50*, 112–123. https://doi.org/10.1016/j.neuroimage.2009.12.002

Proverbio, A. M., Del Zotto, M., & Zani, A. (2007). Inter-individual differences in the polarity of early visual responses and attention effects. *Neuroscience Letters*, *419*, 131–136. https://doi.org/10.1016/j.neulet.2007.04.048

Rushton, W. A. H. (1951). A theory of the effects of fibre size in medullated nerve. *The Journal of Physiology*, *115*, 101–122.

Saron, C. D., & Davidson, R. J. (1989). Visual evoked potential measures of interhemispheric transfer time in humans. *Behavioral Neuroscience*, *103*, 1115–1138. https://doi.org/10.1037/0735-7044.103.5.1115

Slater, D. A., Melie-Garcia, L., Preisig, M., Kherif, F., Lutti, A., & Draganski, B. (2019). Evolution of white matter tract microstructure across the life span. *Human Brain Mapping*, *40*, 2252–2268. https://doi.org/10.1002/hbm.24522

Smith, R. E., Tournier, J. D., Calamante, F., & Connelly, A. (2015). SIFT2: Enabling dense quantitative assessment of brain white matter connectivity using streamlines tractography. *NeuroImage*, *119*, 338–351. https://doi.org/10.1016/j.neuroimage.2015.06.092

Sorrentino, P., Petkoski, S., Sparaco, M., Troisi Lopez, E., Signoriello, E., Baselice, F., Bonavita, S., Pirozzi, M. A., Quarantelli, M., Sorrentino, G., & Jirsa, V. (2022). Whole-brain propagation delays in multiple sclerosis, a combined tractography – Magnetoencephalography study. *The Journal of Neuroscience*, *42*, JN-RM-0938-22–JN-RM-0938-8816. https://doi.org/10.1523/jneurosci.0938-22.2022

Stikov, N., Campbell, J. S. W., Stroh, T., Lavelée, M., Frey, S., Novek, J., Nuara, S., Ho, M. K., Bedell, B. J., Dougherty, R. F., Leppert, I. R., Boudreau, M., Narayanan, S., Duval, T., Cohen-Adad, J., Picard, P. A., Gasecka, A., Côté, D., & Pike, G. B. (2015). In vivo histology of the myelin g-ratio with magnetic resonance imaging. *NeuroImage*, *118*, 397–405. https://doi.org/10.1016/j.neuroimage.2015.05.023

Tabelow, K., Balteau, E., Ashburner, J., Callaghan, M. F., Draganski, B., Helms, G., Kherif, F., Leutritz, T., Lutti, A., Phillips, C., Reimer, E., Ruthotto, L., Seif, M., Weiskopf, N., Ziegler, G., & Mohammadi, S. (2019). hMRI – A toolbox for quantitative MRI in neuroscience and clinical research. *NeuroImage*, *194*, 191–210. https://doi.org/10.1016/j.neuroimage.2019.01.029

Tadel, F., Baillet, S., Mosher, J. C., Pantazis, D., & Leahy, R. M. (2011). Brainstorm: A user-friendly application for MEG/EEG analysis. *Computational Intelligence and Neuroscience*, *2011*, 879716. https://doi.org/10.1155/2011/879716

Tomasi, S., Caminiti, R., & Innocenti, G. M. (2012). Areal differences in diameter and length of corticofugal projections. *Cerebral Cortex*, *22*, 1463–1472. https://doi.org/10.1093/cercor/bhs011

Tournier, J. D., Smith, R., Raffelt, D., Tabbara, R., Dhollander, T., Pietsch, M., Christiaens, D., Jeurissen, B., Yeh, C. H., & Connelly, A. (2019). MRtrix3: A fast, flexible and open software framework for medical image processing and visualisation. *NeuroImage*, *202*, 116137. https://doi.org/10.1016/j.neuroimage.2019.116137

Veraart, J., Nunes, D., Rudrapatna, U., Fieremans, E., Jones, D. K., Novikov, D. S., & Shemesh, N. (2020). Nonivasive quantification of axon radii using diffusion MRI. *eLife*, *9*, e49855. https://doi.org/10.7554/eLife.49855

Vicente, R., Wibral, M., Lindner, M., & Pipa, G. (2011). Transfer entropy-a model-free measure of effective connectivity for the neurosciences. *Journal of Computational Neuroscience*, *30*, 45–67. https://doi.org/10.1007/s10827-010-0262-3

Warner, W., Palombo, M., Cruz, R., Callaghan, R., Shemesh, N., Jones, D. K., Dell'Acqua, F., Ianus, A., & Drobnjak, I. (2023). Temporal diffusion ratio (TDR) for imaging restricted diffusion: Optimisation and pre-clinical demonstration. *NeuroImage*, *269*, 119930. https://doi.org/10.1016/j.neuroimage.2023.119930

Waxman, S., & Bennett, M. (1972). Relative conduction velocities of small myelinated and non-myelinated fibres in the central nervous system. *Nature: New Biology*, *238*, 217–219.

Wegiel, J., Kaczmarski, W., Flory, M., Martinez-Cerdeno, V., Wisniewski, T., Nowicki, K., Kuchna, I., & Wegiel, J. (2018). Deficit of corpus callosum axons, reduced axon diameter and decreased area are markers of abnormal development of interhemispheric connections in autistic subjects. *Acta Neuropathologica Communications*, *6*, 143. https://doi.org/10.1186/s40478-018-0645-7

Westerhausen, R., Kreuder, F., Woerner, W., Huster, R. J., Smit, C. M., Schweiger, E., & Wittling, W. (2006). Interhemispheric transfer time and structural properties of the corpus callosum. *Neuroscience Letters*, *409*, 140–145. https://doi.org/10.1016/j.neulet.2006.09.028

Whitford, T. J., Kubicki, M., Ghorashi, S., Schneiderman, J. S., Hawley, K. J., McCarley, R. W., Shenton, M. E., & Spencer, K. M. (2011). Predicting inter-hemispheric transfer time from the diffusion properties of the corpus callosum in healthy individuals and schizophrenia patients: A combined ERP and DTI study. *NeuroImage*, *54*, 2318–2329. https://doi.org/10.1016/j.neuroimage.2010.10.048

Zhang, H., Hubbard, P. L., Parker, G. J. M., & Alexander, D. C. (2011). Axon diameter mapping in the presence of orientation dispersion with diffusion MRI. *NeuroImage*, *56*, 1301–1315. https://doi.org/10.1016/j.neuroimage.2011.01.084

Zhang, H., Schneider, T., Wheeler-kingshott, C. A., & Alexander, D. C. (2012). NODDI: Practical in vivo neurite orientation dispersion and density imaging of the human brain. *NeuroImage*, *61*, 1000–1016. https://doi.org/10.1016/j.neuroimage.2012.03.072

SUPPORTING INFORMATION

Additional supporting information can be found online in the Supporting Information section at the end of this article.

How to cite this article: Oliveira, R., De Lucia, M., & Lutti, A. (2023). Single-subject electroencephalography measurement of interhemispheric transfer time for the in-vivo estimation of axonal morphology. *Human Brain Mapping*, 1–16. https://doi.org/10.1002/hbm.26420